HYDRAULIC FRACTURE GEOMETRY CHARACTERIZATION USING LOW-FREQUENCY DISTRIBUTED ACOUSTIC SENSING DATA: FORWARD MODELING, INVERSE MODELING, AND FIELD APPLICATIONS

A Dissertation

by

YONGZAN LIU

Submitted to the Office of Graduate and Professional Studies of
Texas A&M University
in partial fulfillment of the requirements for the degree of

DOCTOR OF PHILOSOPHY

Chair of Committee,	Kan Wu
Co-Chair of Committee,	George J. Moridis
Committee Members,	Thomas A. Blasingame
	Hiroko Kitajima
Head of Department,	Jeff Spath

August 2021

Major Subject: Petroleum Engineering

ABSTRACT

Low-Frequency Distributed Acoustic Sensing (LF-DAS) is a promising fracture diagnostic technique for detecting fracture hits and characterizing fracture geometry. However, measured signals exhibiting various characteristics and mechanisms are not well understood, which makes the interpretation and application of LF-DAS data for hydraulic fracture monitoring and characterization much challenging. In this research, a forward geomechanical model was developed based on the three-dimensional displacement discontinuity method (3D DDM) to simulate the LF-DAS strains and strain rates along horizontal wells during multistage/multicluster hydraulic fracturing treatments. The main applications of the forward model include investigating the observed strain/strain-rate responses and their corresponding fracture geometries for better understandings of LF-DAS signals and proposing guidelines for fracture-hit detection during multifracture propagation. More importantly, a Green-function-based inversion algorithm was proposed to estimate fracture geometry by direct inversion of LF-DAS strain data. The stability, accuracy, and efficiency of the proposed algorithm were tested through synthetic cases of both single fracture and multiple fractures. A few field case studies were performed to demonstrate the capability of the proposed workflow. Lastly, a two-dimensional thermoelastic model was presented to quantify the thermal effects on LF-DAS measurements.

A heart-shaped extending region forms before the fracture hit on the waterfall plot of LF-DAS data. After the fracture hits the monitoring well, the extending region shrinks

to a wide band, the size of which depends on the spatial resolution of field DAS measurements, and a two-wing compressing zone is observed. The size and shape of the aforementioned signatures are directly influenced by fracture geometries and fracture interactions. General guidelines for accurate fracture-hit detection were proposed based on detailed characterization of LF-DAS measurements around fracture-hit locations. The inverse modeling indicates that LF-DAS data are only sensitive to the fracture segments near the monitoring well. The developed inversion algorithm can provide the dynamic fracture widths and heights near the monitoring wells during hydraulic fracturing treatments. For the field cases from an unconventional shale oil formation, 4-5 fracture hits out of 8 perforation clusters per stage were detected. Fracturing fluid leakage into the previous fracture stage was observed in all studied stages. Fracture geometries near the monitoring well were characterized.

This research provides a novel workflow for quantitative hydraulic fracture geometry characterization and detection of fracture hits, which has been successfully applied to field cases. The developed workflow can play an important role in optimizing completion and fracturing designs and maximizing well performance in unconventional reservoirs.

DEDICATION

To my parents, Weiming Liu and Lixin Liang

ACKNOWLEDGEMENTS

During my challenging but rewarding Ph.D. study at Texas A&M University, I have gained so much support and help from many individuals, without whom this dissertation would not have been possible. I would like to express my sincere gratitude to all of them.

First and foremost, I would like to thank my advisor, Dr. Kan Wu, who provided me with the opportunity to conduct research in her group. She is always available to give me visionary guidance whenever I encounter a problem throughout my entire research. Her patience and willingness to listen to my ideas make me always feel free to express my thoughts and even to disagree. She is responsible, follows up on students' progress, and cares about students' professional development. Under her supervision, I have improved from different perspectives at a speed that even surprises myself. She is not only a good mentor but also a devoted researcher, who is a role model for me to follow. I am honored to work with her.

Equally important, I am grateful for the continuous guidance, support, and help provided by my co-advisor, Dr. George Moridis. He devotes a tremendous amount of time to stay with his students. He wishes to share all his knowledge and experiences in the subject of reservoir simulation with his students. He is probably the only professor in the PETE department that offers one-to-one instructions with the students for every single coding assignment. By working with him, I have completed the development of a scientifically robust, fully implicit, three-dimensional reservoir simulator, which lays a

solid foundation for my future research. More importantly, it is Dr. Moridis that helps me go through a very tough, stressful, and desperate situation in the early stage of my Ph.D. study. Without him, I could have dropped my Ph.D. study. I can feel that he treats me as his own child. He deserves the sincerest appreciation from the bottom of my heart.

My appreciation is extended to Dr. Ge Jin, an assistant professor at Colorado School of Mines. He is our close research collaborator, but he indeed serves as an academic advisor to me. He shared a lot of his expertise and experience in fiber-optic sensing with me. His guidance, especially in the inverse modeling part, significantly expedites the completion of this dissertation. I always feel fortunate that Dr. Jin and Dr. Wu bring me into this promising area of fiber-optic sensing. In addition, I truly appreciate Dr. Jin for providing me with a lot of genuine and valuable suggestions on my future career plan. I also learned a lot from his generous, optimistic, enthusiastic, and open-minded personality.

I would like to express my special thanks to my advisory committee members, Dr. Thomas Blasingame and Dr. Hiroko Kitajima, for their time, mentorship, comments, and suggestions.

I also would like to thank Dr. Juliana Leung, my MSc supervisor at the University of Alberta. She is the one that I would like to ask for advice when I am in some struggling situations. I much appreciate it she always gives me tremendous support and valuable suggestions. Another person who deserves my sincere acknowledgment is Dr. Lijun Liu from China University of Petroleum (East China). We worked together in 2019, the darkest time of my Ph.D. journey. We discussed research ideas, collaborated on research

papers, and shared many joyful moments, which made me much relaxed during that stressful period. I will always treasure our friendship.

Thanks also go to my friends and colleagues and the department faculty and staff for making my time at Texas A&M University a great experience.

Finally, I must thank my parents, to whom I owe everything in life, for their unconditional love, encouragement, continuous support, and endless faith in me. I also need to express my gratitude to my uncle, Baoheng Song. His encouragement and support help me in every endeavor.

CONTRIBUTORS AND FUNDING SOURCES

Contributors

This work was supervised by a dissertation committee consisting of Professor Kan Wu (advisor), Professor George Moridis (co-advisor), and Professor Thomas Blasingame of the Department of Petroleum Engineering, and Professor Hiroko Kitajima of the Department of Geology & Geophysics.

The fracture geometries used for the synthetic case studies in this dissertation were generated by an in-house fracture propagation model developed by Professor Kan Wu. The raw field DAS data were provided by SM Energy.

All other work conducted for the dissertation was completed by the student independently.

Funding Sources

This work was supported by the start-up funding of Dr. George Moridis and Dr. Kan Wu.

NOMENCLATURE

ε_{ff}	strain in the *f* direction, dimensionless
Γ	boundary surface, m
$\boldsymbol{\chi}$	data-sensitivity vector, dimensionless
ε_{ij}	deviatoric strain, dimensionless
σ_{ij}	deviatoric stress, Pa
δ_{ij}	Dirac delta function, dimensionless
Δu_i	displacement discontinuity of element *i*, m
u_i^-	displacement in *i* direction of negative surface, m
u_i^+	displacement in *i* direction of positive surface, m
u_j	displacement in the *j* direction, m
$T_{ji}(\xi,\eta)$	displacement influence coefficient, dimensionless
Δw_{hit}^t	fracture width changes at fracture-hit location at time *t*, m
q_i^T	heat flow rate, J/s
$\dot{\varepsilon}_{\max}$	maximum strain rate, s^{-1} or min^{-1}
$\overline{f}$	mean of feature *f*
ζ	multiplicative factor, dimensionless
S^-	negative boundary surface, m

$\Delta\dot{\phi}$	phase change rate, radian/s or radian/min
v	Poisson's ratio, dimensionless
S^+	positive boundary surface, m
λ	probe wavelength, 1550 nm
ρ	rock density, kg/m^3
c_p	rock specific heat, J/(kg•K)
k^T	rock thermal conductivity, W/(m•K)
α^T	rock volumetric thermal expansion, 1/K
σ	standard deviation of feature f
ε_j	strain along monitoring well at sensing location j, dimensionless
$\dot{\varepsilon}_{ff}$	strain rate in the f direction, s^{-1} or min^{-1}
$\boldsymbol{\varepsilon}$	strain vector, dimensionless
$\dot{\varepsilon}^t$	strain-rate measurement at time t, s^{-1} or min^{-1}
$\lvert\dot{\varepsilon}\rvert_{\text{sum}}$	summation of strain rate magnitude, s^{-1} or min^{-1}
$\dot{\varepsilon}_{\text{sum}}$	summation of strain rate, s^{-1} or min^{-1}
$f^{'}$	symbol denoting a normalized feature f
c^T	thermal diffusivity, m^2/s
ε_{kk}	volumetric strain, dimensionless
$\sigma_{kk}/3$	volumetric stress, Pa
dt	time step, s or min

e	error vector, dimensionless
f	symbol denoting a specific feature
FOS	fiber-optic sensing
G	Green's function matrix, dimensionless
G	rock shear modulus, Pa
$\mathbf{G}_f$	Green's function matrix corresponding to fracture *f*, dimensionless
K	rock bulk modulus, Pa
L	gauge length, m
M	symmetry-regularization matrix, dimensionless
MW	monitoring well
N	total boundary element number, dimensionless
n_c	refractive index, dimensionless
S	boundary surface, m
S	smoothness-regularization matrix, dimensionless
t	time, s or min
T	time-dependent constraint matrix, dimensionless
w	fracture width vector, m
$\mathbf{w}_f$	width vector of fracture *f*, m
α, β	weighting coefficient, dimensionless

TABLE OF CONTENTS

Page

LIST OF FIGURES

Page

LIST OF TABLES

Page

CHAPTER 1

INTRODUCTION

1.1 Background and Motivation

Unconventional shale reservoirs, typically characterized by low permeability and low porosity, have contributed significantly to the global hydrocarbon production in recent years. Horizontal drilling and multistage hydraulic fracturing are the most commonly used techniques to economically develop such reservoirs. The plug-and-perforate completion scheme has been widely adopted during hydraulic fracturing treatments (Daneshy 2011). Despite their successful applications in unconventional reservoirs, accurate characterization of hydraulic-fracture geometry still remains challenging. Stimulated fracture geometry is highly influenced by many completion parameters, such as well/cluster spacing, number of clusters per stage, injection rate, and volume (Wu et al. 2017), as well as in-situ reservoir conditions including rock mechanical properties, in-situ stress condition, and natural fracture distributions (Dahi-Taleghani and Olson 2011; Fu et al. 2013). However, in addition to the fact that the stimulated well performance is significantly influenced by the hydraulic-fracture geometry, a better understanding of the fracture geometry is critical for optimization of fracture/completion design. For example, a clear idea of fracture length and height helps to optimize the design of well spacing, cluster spacing, and total injection volume for future treatments, and fracture width is an essential parameter for proppant selection (Hu et al. 2018; Wang et al. 2018) and fracture

conductivity (Liu et al. 2019). Therefore, it is of practical importance to accurately characterize hydraulic fracture geometry.

Hydraulic fracture monitoring and characterization have received much research interest in recent years. Many diagnostic techniques have been developed to address the challenges associated with hydraulic fracture characterization. Production/tracer data analysis is a conventional method to characterize fractured reservoir properties, based on analytical/semi-analytical reservoir models (Clarkson and Williams-Kovacs 2013, Karmakar et al. 2016). The results of this method are strongly dependent on the assumptions of the applied models. Microseismic monitoring has been used in the oil and gas industry for a long time (Fisher et al. 2004). Microseismic events are small earthquakes that are often associated with hydraulic fracturing treatments (Van Der Baan et al. 2013). Microseismic mapping of hydraulic fracture has become a common technique, which provides information regarding hydraulic fracture azimuth, height, length, and complexity due to fracture interactions (Maxwell et al. 2009). Time-lapse multicomponent surface seismic data have been used to monitor hydraulic stimulations as well (Atkinson and Davis 2011). The low-permeability nature of unconventional reservoirs would reduce the time-lapse response of compressional wave data, while shear-wave splitting is a possible method to depict hydraulic fractures. Analysis of shear-wave splitting before and after the hydraulic fracturing treatments can roughly provide an estimation of the stimulated fracture networks. Poroelastic responses in offset wells are recently used to diagnose multi-cluster fracture propagation (Dawson and Kampfer 2016, Seth et al. 2019). The poroelastic pressure responses observed at offset monitoring wells during a stimulation

job are used to infer fracture information and evaluate completion efficiency. Sealed wellbore pressure monitoring at offset wells is another diagnostic technique that has been used recently to quantify cluster efficiency (Haustveit et al. 2020). The derivative of sealed wellbore pressure shows an obvious peak value when the fracture hits the sealed monitoring well. This technique can be used to count fracture number in the far field and qualitatively evaluate cluster efficiency and fluid distribution. Geochemical fingerprinting is another technology for reservoir characterization and reservoir monitoring (Liu et al. 2020a). The drainage fracture height and intensity can be obtained from the geochemical signatures. In addition, the variations of geochemical signatures in the oil samples gathered before and after stimulation treatments can be used to identify cross-well communications. Electromagnetic imaging is a surface-based electromagnetic technique that assists in imaging the placement of fracturing fluid/proppant during completion operations (Haustveit et al. 2017, Ng et al. 2019). The introduction of fracturing fluid or proppant into the reservoir can alter the electromagnetic field. The differences allow for the spatial distribution of fracturing fluid/proppant to be delineated, which is an indicator of the areal extension of hydraulic fractures.

Although the aforementioned techniques can provide some information regarding hydraulic fracture geometry, none of these techniques can provide complete information on fracture geometry (i.e., fracture length, height, and width), especially fracture width. Most of the current diagnostic techniques just depict the areal range of stimulated fracture networks. In addition, the interpreted fracture geometry can be influenced by many uncertainties such as bias and dislocations of microseismic events. Poroelastic pressure or

sealed wellbore pressure responses at offset wells can help characterize hydraulic fractures, but the analyses remain at a qualitative level. No studies indicate that these techniques can quantitatively characterize hydraulic fracture geometry. More advanced monitoring or diagnostic technologies are needed for detailed hydraulic fracture geometry characterization.

Fiber optic sensing technology gains increasing interest from the oil and gas industry. Distributed Temperature Sensing (DTS) and Distributed Acoustic Sensing (DAS) are two main fiber optic-based monitoring and diagnostic techniques. DTS has a broad range of applications. For example, DTS can be used to monitor thermal processes in the subsurface such as steam injection in heavy oil reservoirs and cold-water injection in geothermal reservoirs. In unconventional reservoirs, DTS can be used to allocate injected fluid distribution among multiple clusters during hydraulic fracturing (Tabatabaei and Zhu 2012, Li and Zhu 2018) and quantify inflow distribution for well performance evaluation during long-term production (Huckabee 2009, Sun et al. 2017, Zhang and Zhu 2020). DAS is a promising technology that has become available for the oil and gas industry in recent years and has been used in monitoring the stimulation of unconventional reservoirs (Webster et al. 2013, Jin and Roy 2017). DAS requires an optical fiber attached to the wellbore to transmit laser energy into the reservoir. Each section of the fiber scatters a small portion of the laser energy back to the surface sensing unit, which uses interferometry techniques to determine strain changes along the fiber (Bakku 2015, Jin et al. 2019). Because the fiber can be installed either inside or outside a well casing, extensive measurements can be recorded during stimulation or production without interfering with

well operations (Sherman et al. 2017). Moreover, DAS can monitor over a much wider length (up to tens of kilometers) and at a wider range of frequencies (from near direct current to kilohertz) than conventional downhole sensors such as geophones (Sherman et al. 2019). Once the fiber is installed in a well, it provides nonintrusive, continuous, and real-time measurements along the wellbore. Because of these advantages, many DAS applications have been developed for unconventional reservoirs (Grubert et al. 2020), including ball tracking and seating, injection monitoring (Boone et al. 2015), perforation cluster efficiency diagnostics (Ugueto et al. 2016), interstage/interwell communication detection (Holley and Kalia 2015), and production/injection profiling (In't Panhuis et al. 2014, Sun et al. 2020). The previously mentioned applications focus on the high-frequency bands (> 1 Hz) of the DAS data and most of these applications are limited to the treatment wellbore and near-wellbore region. Moreover, these analyses are usually based on the intensity of DAS data.

Recently, Jin and Roy (2017) illustrated that the low-frequency component of DAS (LF-DAS) data (< 0.05 Hz) recorded at offset monitoring wells provides critical information about fracture hits and hydraulic fracture geometry. Figure 1.1 illustrates the well trajectories of a well pair consisting of a treatment well and an offset monitoring well. When the DAS cable is directly attached to the formation with perfect coupling, it can record the dynamic strain perturbations in the formation induced by the fractures propagating from the treatment well. The LF-DAS data can be treated as linear-scaled strains or strain rates, depending on the sensing unit provider. When the data deliverable is a time differential of the measured optical phase, it is equivalent to strain rate; otherwise,

it approximates the strain variation along the fiber (Jin et al. 2017, Sherman et al. 2019). Compared with the industry-standard waterfall visualizations, which only focus on the intensity of the data, the low-frequency processing not only increases the signal-to-noise ratio (i.e., interrogator noise, random background noise, or other unrelated high-frequency signals such as pumping noise) but also preserves the measurement polarity that allows the strain perturbation during stimulation treatments to be clearly identified (Jin and Roy 2017). LF-DAS signals provide high-resolution far-field information about fracture geometry and stimulation efficiency (Karrenbach et al. 2019, Ugueto et al. 2019).

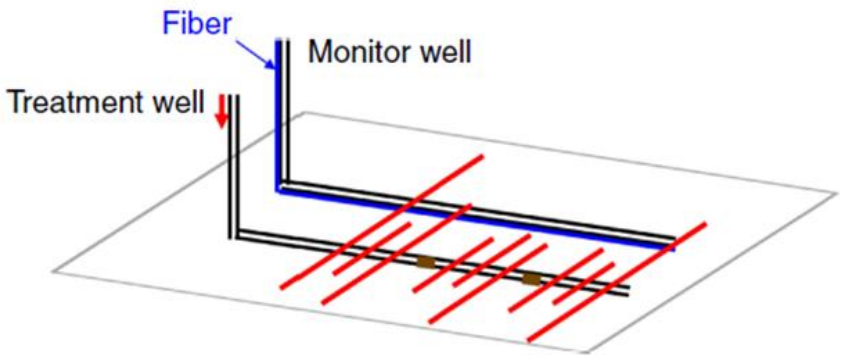

Figure 1.1 Illustration of a well pair consisting of a treatment well and a monitoring well attached with fiber for DAS (reprinted from Liu et al. 2020d).

Large amounts of cross-well DAS data have been acquired across different formations with the advancement in fiber technology. However, the tremendous accomplishment is not matched with an equal advancement in data interpretation. Measured signals from different wells exhibit various characteristics and mechanisms

attributing to the differences are not well understood, which limits maximizing values of this enabling technology in unconventional reservoir stimulation and development.

1.2 Literature Review

1.2.1 Distributed Acoustic Sensing Principle and Low-Frequency Processing

Distributed acoustic sensing (DAS) measures Rayleigh scatter distributed along the fiber optic cable (Hill 2015). A single-mode optical fiber is connected to a laser source from an interrogator that emits laser pulses (Silkina 2014). A coherent laser pulse from an interrogator is sent along the fiber and the fiber acts as a distributed interferometer with a pre-set gauge length (Jin et al. 2019a). The interactions between the light and fiber compositions can cause a small portion of the light to backscatter and return to the input end, where it is detected and analyzed. The intensity and phase of the reflected light are measured as a function of time after transmission of the laser pulse. When the pulse has traveled the full length of the fiber, the next laser pulse is sent along the fiber (Jin et al. 2019a). Changes in the reflected intensity and phase of successive pulses from the same interval of fiber are caused by changes in the optical path length of that section of fiber, which is sensitive to both strain and temperature variations of the fiber.

DAS data in the low-frequency band is a powerful attribute to monitor slow strain and temperature perturbation near the monitoring well (Jin et al. 2017b). The raw DAS data is usually stored in optical phase change and sampled at a very high frequency. To

obtain the low-frequency components, low-frequency data processing is a necessary step. The general procedure is summarized as follows (Jin et al. 2017a, 2017b):

1. The raw data is usually firstly downsampled to a lower sampling rate (e.g., 1 data point per second).

2. Apply a median filter to remove spiky noises.

3. Apply a low-pass filter with a specific corner frequency (e.g., 0.05 Hz is used in this study).

4. Remove the drift noise from the data. The drift noise is channel invariant and does not vary significantly with time, which is most likely associated with interrogator noise (Jin et al. 2017b). This noise can be estimated by the median value of the channels that are out of the zone of interest at each time interval.

1.2.2 Field Observation of Low-Frequency Distributed Acoustic Sensing

DAS data in the low-frequency bands have been used for fracture monitoring and diagnostics in the field. A few field examples have been published recently to demonstrate the potential of LF-DAS data for completion efficiency evaluation and detailed characterization of hydraulic fracture geometry. Jin and Roy (2017b) were among the first to demonstrate how to constrain hydraulic fracture geometry using LF-DAS data through a field example. Karrenbach et al. (2019) correlated the DAS data within a frequency band of less than 1 Hz of a field example with the onset of microseismic events. The two data sets correlate well with each other both in time and space, which helps to improve hydraulic fracturing monitoring. Ugueto et al. (2019) presented field examples of LF-DAS in wells stimulated for a variety of completion systems and demonstrated how to use

extensive LF-DAS measurements to evaluate stimulation efficiency. Ichikawa et al. (2019) attempted to identify fracture hits using the low-frequency components of DAS data acquired during a stimulation treatment in the Montney tight gas formation. Richter et al. (2019) presented an advanced high-resolution distributed acoustic sensor that utilizes engineered optical fibers and developed a retrievable wireline fiber-optic cable for economic hydraulic fracture monitoring and optimization. The presented system could significantly improve the sensitivity and data quality that is beneficial for acquiring LF-DAS strain data. Jin et al. (2019b) proposed a machine-learning-based algorithm to automate fracture-hit identification using LF-DAS signals and successfully applied the workflow in a field case study. Li et al. (2020) conducted cross-well communication analysis based on a set of real-time field LF-DAS strain measurements and concluded that the fracture hit of each fracture can be identified from the signatures of LF-DAS signals. Wu et al. (2020) illustrated through field LF-DAS data that cross-well far-field strain measurements can be used to determine fracture azimuth, the width of the fractured region, and fracture height with a high degree of accuracy and resolution.

In the aforementioned field examples, the well spacing ranges from approximately 300 ft to more than 1300 ft. Strong LF-DAS signals were observed from all wells with different offset distances, which is consistent with the statement in Raterman et al. (2019) that the typical well spacing (approximately 400 to 800 ft) in modern horizontal-well design facilitates cross-well communications. In the aforementioned studies, the focuses were all about field data analysis and qualitative interpretation. Fracture hits in the LF-DAS signals are always interpreted as the fiber locations that experience strong extension

(fracture opening) during the pumping period and strong compression (fracture closure) during the shut-in period. However, the field data may exhibit very complex signatures, especially for multicluster completion scenarios in which fracture interference plays a role. Under such circumstances, the interpretation of LF-DAS signals can be very challenging.

1.2.3 Numerical Modeling of Low-Frequency Distributed Acoustic Sensing Signals

To better understand the mechanisms for LF-DAS signals, a few numerical studies have been done to model the strain/strain-rate variations along monitoring wells.

Sherman et al. (2017, 2019) simulated the LF-DAS signals using a Multiphysics-coupled simulator and identified the signatures of strain and strain rate along monitoring wells concerning different fracture geometries with consideration of a discrete fracture network (DFN). These are the first efforts that tried to understand LF-DAS signals through geomechanical modeling. However, only a single hydraulic fracture was considered in their study, strain/strain-rate variations were calculated along an offset vertical monitoring well, which is not a typical well configuration in the field (i.e., horizontal offset monitoring wells, as shown in Figure 1.1).

Sherman et al. (2018) used the same model to test the ability of LF-DAS to monitor proppant placement in a fracture and found that LF-DAS signals can be used to diagnose proppant tip screen-out. The geomechanical problem is solved using the Finite Element Method (FEM) that requires domain discretization, which could be computationally expensive. Moreover, the strain field calculated by FEM is a tensor and it needs to be projected into the direction of the monitoring well.

Zhang et al. (2020) used the Displacement Discontinuity Method (DDM), which is a more efficient approach to model the fracture-induced linear-elastic rock deformation, to simulate the strain/strain-rate responses along both horizontal and vertical monitoring wells during hydraulic fracturing treatments. The simulation results were compared against field data gathered from Hydraulic Fracturing Test Site 2 (HFTS2). The dynamic fracture geometries were generated by manually changing the fracture size at each time step, instead of using a physical fracturing simulator.

1.2.4 Gaps in Existing Studies

In summary, field data have shown that LF-DAS measurements provide critical information on hydraulic fracture geometry. However, the current research efforts are mostly focused on the qualitative interpretation of field data. Only a few forward numerical studies have been conducted to better understand the observed LF-DAS signatures. More work needs to be done to investigate the fundamental mechanisms controlling the signatures of strain and strain-rate responses measured by LF-DAS and to better utilize LF-DAS data for hydraulic fracture geometry characterization.

Moreover, the forward geomechanical modeling of LF-DAS signals lays the foundation for quantitative hydraulic fracture geometry characterization. However, to the best of our knowledge, no study has been done to quantify detailed fracture geometry by directly inverting the LF-DAS strain data. It is meaningful and necessary to develop inversion algorithms to estimate hydraulic fracture geometry using LF-DAS data.

1.3 Objectives

The general objective of this research is to better understand and utilize LF-DAS signals for quantitative hydraulic fracture geometry characterization. This research is focused on (1) understanding the fundamental mechanisms and their influencing factors for LF-DAS signals through a forward numerical model, and (2) characterizing hydraulic fracture geometry at a quantitative level by developing an inversion algorithm to interpret LF-DAS strain data. The specific objectives are as follows.

1. Develop a three-dimensional geomechanical model to simulate LF-DAS signals measured along offset wells during hydraulic fracturing treatments to investigate the mechanisms for various patterns of LF-DAS signals from the perspective of rock deformation and provide insights for the interpretation of LF-DAS measurements.
2. Propose a general guideline of fracture-hit detection for multi-stage fracture treatments based on quantitative analyses of LF-DAS strain/strain-rate responses.
3. Develop an inversion algorithm to quantify fracture geometry by the inversion of LF-DAS strain data.
4. Build a practical workflow for field applications, which contains raw DAS data processing, fracture-hit identification and completion efficiency evaluation based on LF-DAS signals, and data interpretation for hydraulic-fracture geometry characterization.

5. Develop a thermoelastic model to quantify the thermal effects on cross-well LF-DAS measurements and assess whether temperature perturbation during cold fluid injection into subsurface reservoirs has significant impacts on LF-DAS measurements.

1.4 Dissertation Outline

This dissertation consists of eight chapters. In this chapter (Chapter 1), the background and motivation of this research are discussed, followed by the literature review. Then the research objectives are illustrated.

Chapter 2 presents the development and validation processes of a three-dimensional geomechanical model based on the Displacement Discontinuity Method (DDM). This model can be used to simulate LF-DAS measurements along any offset horizontal wells with arbitrary trajectories during hydraulic fracturing treatments.

In Chapter 3, the forward model developed in Chapter 2 is applied to simulate LF-DAS signals along offset horizontal wells. The basic characteristics of LF-DAS strain and strain rate measured during single-fracture propagation are analyzed. The impacts of fracture width, fracture height, and fracture-height growth on LF-DAS signals are discussed through sensitivity analysis. Finally, a field case is interpreted based on the forward modeling results.

The objective of Chapter 4 is to accurately identify fracture hits using complex LF-DAS signals. We simulate simultaneous multiple-fracture propagation as well as fracture-induced strain and strain-rate responses along an offset monitoring well. A general guideline for fracture-hit detection is proposed based on quantitative analysis of LF-DAS

measurements. Then a set of field examples are presented to demonstrate the potential of LF-DAS data on hydraulic fracture monitoring and characterization.

Chapter 5 presents a Green-function-based inversion algorithm for quantitative hydraulic fracture geometry characterization. Firstly, the procedure to construct the Green-function matrix corresponding to a single fracture is presented. The robustness and accuracy of the inversion algorithm, and LF-DAS data sensitivity are tested through a single-fracture synthetic case. Then, the algorithm is extended to handle multifracture cases. Mitigation of non-unique inversion solutions is discussed using a multiple-fracture synthetic case. Finally, a method to approximate fracture height is presented.

Chapter 6 is primarily the field applications of the developed inversion algorithm in Chapter 5. Three consecutive stages of the same well are included. The results include time-dependent fracture width profiles and fracture heights at the end of fluid injection. The methods to estimate fracture length are also briefly discussed in this chapter.

In Chapter 7, we present a two-dimensional thermoelastic model to quantify the impacts of temperature variation on cross-well LF-DAS measurements. The implementation is validated against analytical solutions of thermal-induced rock deformation by a point heat source, followed by a set of sensitivity studies.

Chapter 8 summarizes the conclusions obtained from this dissertation and provides some pertinent suggestions for future work on this topic.

CHAPTER 2

FORWARD MODEL DEVELOPMENT AND VALIDATION*

2.1 Overview

In this chapter, the development and validation processes of a forward numerical model to simulate LF-DAS signals are presented. The model is derived based on the three-dimensional displacement discontinuity method. Linear-elastic rock deformation at any arbitrary point induced by hydraulic fractures can be calculated efficiently by the developed model. The numerical implementation is validated against the analytical solution of rock deformation induced by a simple fracture (Pollard and Segall 1987).

2.2 Three-Dimensional Linear-Elastic Displacement Discontinuity Method

Displacement Discontinuity Method (DDM) is an efficient method to calculate fracture-induced elastic rock deformation at any arbitrary location in an infinite elastic domain (Crouch et al. 1983). For crack-like geometries, the boundary *S* can be treated as two surfaces $S^{\pm}$, as shown in Figure 2.1. The displacement components at an arbitrary point ξ, induced by displacement discontinuities located at point η over the fracture surface *S*, can be expressed as (Shou 1993, Wu 2014)

*Part of this chapter is reprinted with permission from "Rock Deformation and Strain-Rate Characterization during Hydraulic Fracturing Treatments: Insights for Interpretation of Low-Frequency Distributed Acoustic-Sensing Signals" by Liu, Y., Wu, K., Jin, G., and Moridis, G., 2020. *SPE Journal*, 25 (05), 2251-2264, Copyright [2020] by Society of Petroleum Engineers.

$$u_j(\xi) = \int_S T_{ji}(\xi,\eta)\Delta u_i dS(\eta) \quad \Delta u_i = u_i^- - u_i^+, \tag{2.1}$$

where u_i^- and u_i^+ are the displacement components of surfaces S^- and S^+, respectively. The quantities $T_{ji}(\xi,\eta)$ represent the influences of a displacement discontinuity in the *i* direction at η on the displacement in the *j* direction at ξ. To numerically solve the above equation, the boundary surface is divided into *N* elements. With the assumption of constant displacement discontinuities over each element (S_m), Eq. (2.1) can be written as

$$u_j(\xi) = \sum_{m=1}^{N} T_{ji}^*(\xi,\eta_m)\Delta u_i(\eta_m), \tag{2.2}$$

$$T_{ji}^*(\xi,\eta_m) = \int_{S_m} T_{ji}(\xi,\eta)dS(\eta). \tag{2.3}$$

Analytical solutions of influence coefficients T^* are reported by Shou (1993) and Wu (2014), which are briefly reviewed for completeness, followed by the numerical implementation procedure.

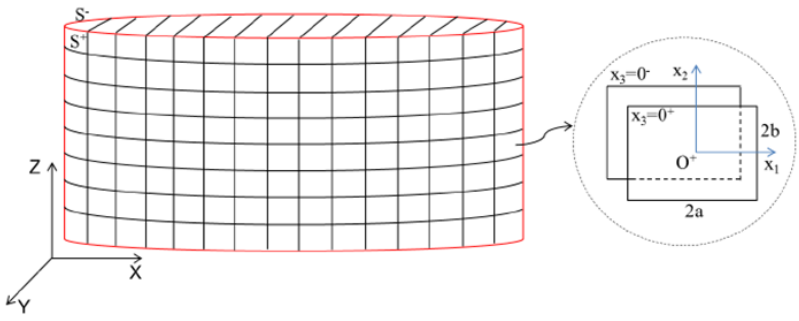

Figure 2.1 Schematic of a three-dimensional vertical fracture in an elastic body (adapted from Wu 2014).

As shown in Figure 2.1, the global coordinate is labeled as X, Y, Z. For each fracture element, the local coordinate system is denoted as x_1, x_2, x_3. x_3 is pointing from the negative side ($x_3 = 0^-$) to the positive side ($x_3 = 0^+$). In the local coordinate, the displacement discontinuities in the three directions are written as

$$\begin{aligned} D_1(x_1, x_2, 0) &= u_1(x_1, x_2, 0^-) - u_1(x_1, x_2, 0^+) \\ D_2(x_1, x_2, 0) &= u_2(x_1, x_2, 0^-) - u_2(x_1, x_2, 0^+), \\ D_3(x_1, x_2, 0) &= u_3(x_1, x_2, 0^-) - u_3(x_1, x_2, 0^+) \end{aligned} \tag{2.4}$$

where u_1, u_2, u_3 are displacements in the x_1, x_2, x_3 directions, respectively.

The analytical solution to the problem of a constant displacement D_i over a rectangular area in the local coordinate $|x_1| \le a$, $|x_2| \le b$, $x_3 = 0$ (Figure 2.1) in an infinite elastic solid can be expressed in terms of three harmonic functions Φ_i and their derivatives, $i = 1, 2, 3$, as (Salamon 1964)

$$\begin{aligned} u_1 &= 2(1-\nu)\Phi_{1,3} - (1-2\nu)\Phi_{3,1} - x_3\Phi_{k,k1} \\ u_2 &= 2(1-\nu)\Phi_{2,3} - (1-2\nu)\Phi_{3,2} - x_3\Phi_{k,k2} \\ u_3 &= 2(1-\nu)\Phi_{3,3} - (1-2\nu)(\Phi_{1,1} + \Phi_{2,2}) - x_3\Phi_{k,k3} \end{aligned}, \tag{2.5}$$

where ν is the Poisson's ratio, and the notation ',i' represents the partial derivative with respect to x_i. Einstein notation is used in terms $\Phi_{k,ki}$.

The functions Φ_i are associated with displacement discontinuities, which can be written as (Crouch et al. 1983)

$$\Phi_i = \frac{1}{8\pi(1-\nu)} D_i I(x_1, x_2, x_3), \tag{2.6}$$

in which

$$I\left(x_1, x_2, x_3\right) = \int_{-b}^{b}\int_{-a}^{a} r^{-1} d\xi_1 d\xi_2 , \tag{2.7}$$

and

$$r = \sqrt{\left(x_1 - \xi_1\right)^2 + \left(x_2 - \xi_2\right)^2 + x_3^2} . \tag{2.8}$$

After integration, $I\left(x_1, x_2, x_3\right)$ in Eq. (2.7) becomes

$$I\left(x_1, x_2, x_3\right) = \left[\bar{x}_1 \ln\left(r + \bar{x}_2\right) + \bar{x}_2 \ln\left(r + \bar{x}_1\right) - x_3\theta\right]\Big|_{\xi_1=-a}^{\xi_1=a}\Big|_{\xi_2=-b}^{\xi_2=b}, \tag{2.9}$$

where $\bar{x}_1 = x_1 - \xi_1$, $\bar{x}_2 = x_2 - \xi_2$, and $\theta = \tan^{-1}\left[\dfrac{\bar{x}_1 \bar{x}_2}{r x_3}\right]$. The related derivatives of function *I* are derived as

$$J_1 = I_{,1} = \ln\left(r + x_2 - \xi_2\right)\Big\|, \tag{2.10}$$

$$J_2 = I_{,2} = \ln\left(r + x_1 - \xi_1\right)\Big\|, \tag{2.11}$$

$$J_3 = I_{,3} = -\tan^{-1}\left(\frac{\left(x_1 - \xi_1\right)\left(x_2 - \xi_2\right)}{x_3 r}\right)\Big\|, \tag{2.12}$$

$$J_4 = I_{,11} = \frac{\left(x_1 - \xi_1\right)}{r\left(r + x_2 - \xi_2\right)}\Big\|, \tag{2.13}$$

$$J_5 = I_{,22} = \frac{\left(x_2 - \xi_2\right)}{r\left(r + x_1 - \xi_1\right)}\Big\|, \tag{2.14}$$

$$J_6 = I_{,33} = \frac{\left(x_1 - \xi_1\right)\left(x_2 - \xi_2\right)\left(x_3^2 + r^2\right)}{r\left[x_3^2 + \left(x_1 - \xi_1\right)^2\right]\left[x_3^2 + \left(x_2 - \xi_2\right)^2\right]}\Big\|, \tag{2.15}$$

$$J_7 = I_{,12} = \frac{1}{r}\Big\|, \tag{2.16}$$

$$J_8 = I_{,13} = \frac{x_3}{r\left(r + x_2 - \xi_2\right)}\Big\|, \tag{2.17}$$

$$J_9 = I_{,23} = \frac{x_3}{r\left(r + x_1 - \xi_1\right)}\Big\|. \tag{2.18}$$

The symbol || denotes Chinnery's notation, which is expressed as

$$J\left(\xi_1, \xi_2\right) = J\left(a, b\right) - J\left(a, -b\right) - J\left(-a, b\right) + J\left(-a, -b\right). \tag{2.19}$$

Substitute the *J* functions into Eq. (2.5) gives

$$u_1 = \frac{1}{8\pi\left(1-\nu\right)}\left\{\left[2\left(1-\nu\right)J_3 - x_3 J_4\right]D_1 - x_3 J_7 D_2 - \left[\left(1-2\nu\right)J_1 + x_3 J_8\right]D_3\right\}, \tag{2.20}$$

$$u_2 = \frac{1}{8\pi\left(1-\nu\right)}\left\{-x_3 J_7 D_1 + \left[2\left(1-\nu\right)J_3 - x_3 J_5\right]D_2 - \left[\left(1-2\nu\right)J_2 + x_3 J_9\right]D_3\right\}, \tag{2.21}$$

$$u_3 = \frac{1}{8\pi\left(1-\nu\right)}\begin{Bmatrix}\left[\left(1-2\nu\right)J_1 - x_3 J_8\right]D_1 + \left[\left(1-2\nu\right)J_2 - x_3 J_9\right]D_2 \\ + \left[2\left(1-\nu\right)J_3 - x_3 J_6\right]D_3\end{Bmatrix}. \tag{2.22}$$

Based on Eqs. (2.20), (2.21), and (2.22), the displacements at any arbitrary point can be obtained by coordinate transformation and superposition. The implementation procedure for vertical fractures (i.e., angle between x_2 and Z is zero) is summarized as follows,

Step 1: For each element, transform its global coordinates $\left(X, Y, Z\right)$ into local coordinates $\left(x_1, x_2, x_3\right)$. For vertical fractures, the transformation matrix from global coordinate to local coordinate for the system shown in Figure 2.1 is

$$\mathbf{A}=\begin{bmatrix}1 & 0 & 0\\ 0 & 0 & 1\\ 0 & 1 & 0\end{bmatrix}\begin{bmatrix}\cos\beta & \sin\beta & 0\\ -\sin\beta & \cos\beta & 0\\ 0 & 0 & 1\end{bmatrix}=\begin{bmatrix}\cos\beta & \sin\beta & 0\\ 0 & 0 & 1\\ -\sin\beta & \cos\beta & 0\end{bmatrix}, \tag{2.23}$$

where β is the angle between X and x_2. Then a point in the local coordinate system can be calculated by

$$\begin{bmatrix}x_1\\ x_2\\ x_3\end{bmatrix}=\begin{bmatrix}\cos\beta & \sin\beta & 0\\ 0 & 0 & 1\\ -\sin\beta & \cos\beta & 0\end{bmatrix}\begin{bmatrix}X\\ Y\\ Z\end{bmatrix}. \tag{2.24}$$

Step 2: Calculate displacement components in the local coordinate system using Eqs. (2.20)-(2.22).

Step 3: To superimpose the contributions of all the boundary elements, the displacements in the local coordinate system of each element should be transformed back to the global coordinate system, following

$$\begin{bmatrix}U_x\\ U_y\\ U_z\end{bmatrix}=\begin{bmatrix}\cos\beta & -\sin\beta & 0\\ 0 & 0 & 1\\ \sin\beta & \cos\beta & 0\end{bmatrix}\begin{bmatrix}u_1\\ u_2\\ u_3\end{bmatrix}. \tag{2.25}$$

Step 4: Superimpose the contributions from all the boundary elements to calculate the displacement field at survey points.

2.3 Low-Frequency Distributed Acoustic Sensing Strain and Strain Rate

The LF-DAS measurements are equivalent to linearly scaled directional strain or strain rate along the fiber over a predefined gauge length (Jin and Roy 2017b; Ugueto et al. 2019). As shown in Figure 2.2, the discrete sampling locations on the fiber (i.e., channel

locations) locate at the center of each measurement gauge length. The gauge lengths can overlap if they are larger than the channel spacing, which is always the case in DAS.

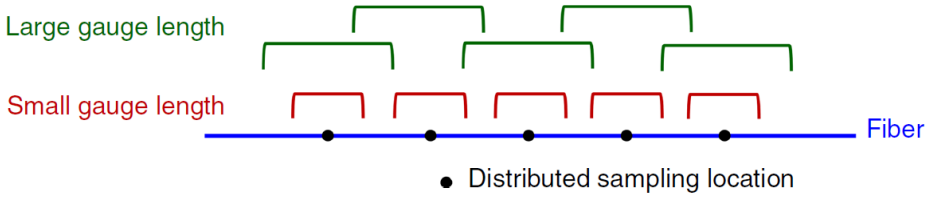

Figure 2.2 Illustration of distributed sensing locations and different gauge lengths (reprinted from Liu et al. 2020b).

To be consistent with the distributed acoustic sensing principle, the strain (ε_{ff}) and strain rate ($\dot{\varepsilon}_{ff}$) along the fiber are calculated following

$$\varepsilon_{ff} = \frac{u_f^{j+\frac{L}{2}} - u_f^{j-\frac{L}{2}}}{L}, \tag{2.26}$$

$$\dot{\varepsilon}_{ff} = \frac{d\varepsilon_{ff}}{dt} = \frac{\varepsilon_{ff}^{n+1} - \varepsilon_{ff}^{n}}{t^{n+1} - t^{n}}, \tag{2.27}$$

where the subscript *f* indicates the direction along the monitoring well, and superscripts *j* and *n* represent the location index and time (*t*) index, respectively. u_f is the displacement component along the fiber direction. *L* represents the gauge length. The strain at each sensing location (*j*) is calculated by dividing the directional displacement difference between the two points on both sides of *j* with a distance of *L*/2 by the gauge length (*L*). The strain rate is calculated by dividing the strain difference at two adjacent time steps by the time interval (Eq. (2.27)).

2.4 Model Assumptions

In the developed model for modeling and analysis of LF-DAS signals, there are several limitations/assumptions that need further improvements:

1. It is assumed that the rock deformation is linear elastic and the formation is homogeneous and isothermal. Second, hydraulic fractures are vertical.
2. We assume that the fiber is perfectly coupled to the surrounding rock, and the differences in mechanical properties between them are not considered, such that the LF-DAS measurements are accurate representations of the simulated rock deformations.
3. Thermal effects on the LF-DAS measurements are not included in the calculation of rock deformation. The temperature difference between the injected fracturing fluid and subsurface formation may induce stress/strain in the surrounding matrix that can be measured by DAS. The temperature effects may be calibrated if the cable includes distributed temperature sensors.
4. Fluid pressure in the matrix around the fracture may build up because of fluid leakoff and rock deformation during the hydraulic fracturing treatments, which needs to be considered in future studies so that the poroelastic effects can be included.

2.5 Model Validation

Pollard and Segall (1987) derived analytical models for calculating the induced stress and displacement fields around a fracture with constant internal pressure under the

plane strain condition. To validate the implementation of the presented model, a numerical case is constructed with the fracture height being 100 m and fracture length being 20 m, so that the plane strain condition is satisfied. A schematic of the fracture is presented in Figure 2.3. Fracture height is along the x_3 direction. The Young's modulus is 10 GPa, the Poisson's ratio is 0.2, and the uniform internal pressure is 10 MPa. The induced displacements along the centerline of the fracture (i.e., along the x_1 direction) calculated by the numerical model are compared against the analytical solutions in Figure 2.4. The good agreements validate the implementation of the geomechanical model of fracture-induced rock deformation.

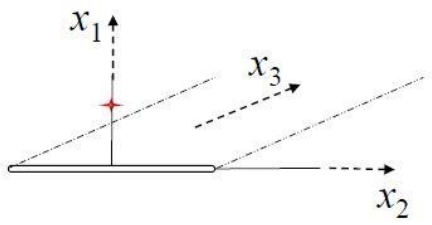

Figure 2.3 Schematic of a fracture in an infinite elastic body with a constant internal pressure.

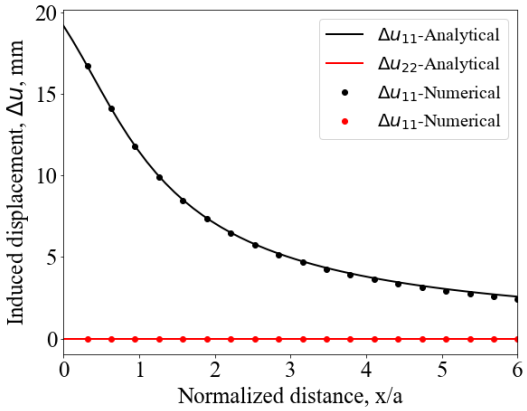

Figure 2.4 Fracture-induced displacements as a function of normalized distance away from the fracture surface (a represents the fracture half-length).

2.6 Summary

In this chapter, we presented a forward geomechanical model to simulate cross-well DAS signals. The procedure to obtain the cross-well LF-DAS data consists of mainly three steps. Firstly, calculate the fracture-induced displacements along the monitoring well at the sensing points. Then, calculate the LF-DAS strains under the predefined gauge length. Finally, calculate the LF-DAS strain rates by differentiating the strain variation by the time step. The developed model can efficiently simulate the LF-DAS signals during fracture propagation processes.

CHAPTER 3

ROCK DEFORMATION AND STRAIN-RATE CHARACTERIZATION DURING HYDRAULIC FRACTURING TREATMENT*

3.1 Overview

In this chapter, the geomechanical model developed in Chapter 2 is applied to simulate the induced rock deformation and characterize the strain/strain-rate responses measured along monitoring wells during fracture propagation. First, a base case with a single fracture is constructed to illustrate the signatures of displacement, strain, and strain rate measured along three monitoring wells with different well spacings. Then, the impacts of fracture width, fracture height, and height growth on LF-DAS measured strain-rate characteristics are examined. Lastly, the signatures of dynamic displacement/strain/strain rate along a monitoring well for a simultaneous four-cluster propagation case are discussed and compared against field LF-DAS data recorded during the treatment of a single stage.

3.2 Basic Characteristics of LF-DAS Strain and Strain Rate

In the base case, a single-cluster fracture propagation is simulated using a fracture propagation model developed by Wu (2014). The associated dynamic deformations (i.e.,

*Part of this chapter is reprinted with permission from "Rock Deformation and Strain-Rate Characterization during Hydraulic Fracturing Treatments: Insights for Interpretation of Low-Frequency Distributed Acoustic-Sensing Signals" by Liu, Y., Wu, K., Jin, G., and Moridis, G., 2020. *SPE Journal*, 25 (05), 2251-2264, Copyright [2020] by Society of Petroleum Engineers.

displacement, strain, and strain rate) along three monitoring wells with different offset distances to the treatment well are calculated. The well configuration is schematically illustrated in Figure 3.1. The relevant completion parameters and in-situ geomechanical conditions are presented in Table 3.1.

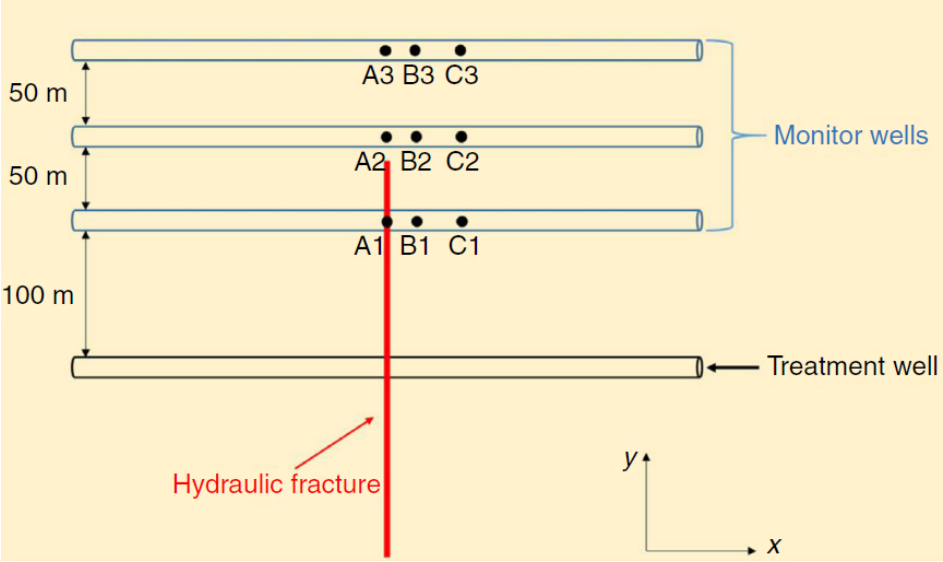

Figure 3.1 Schematic of well configuration with offset distances for the base case (reprinted from Liu et al. 2020d).

Figure 3.2 illustrates the fracture half-length evolution and fracture-width profiles at different injection times. It takes approximately 12, 24.5, and 42 minutes, respectively, for the fracture to reach 100, 150, and 200 m (i.e., offset distances of the three monitoring wells). The fracture-induced displacement and strain fields in the direction of monitoring wells at the end of fluid injection are shown in Figure 3.3. As shown in Figure 3.3(a), the fracture-induced displacement on each side of the fracture has the same magnitude but

different signs, because fracture opening deforms the rock on each side of the fracture in opposite directions. Figure 3.3(b) illustrates the strain field around the fracture with compression zones on both sides of the fracture and extension zones in front of the fracture tips. These features of fracture-induced deformation could produce characteristic signatures during fracture propagation that are measurable by distributed acoustic sensing.

Table 3.1 Summary of geomechanical and completion parameters for the base case (adapted from Liu et al. 2020d).

Parameter	Unit	Value
Young's Modulus	GPa	21.4
Poisson's Ratio	-	0.26
Minimum Horizontal Stress	MPa	41.34
Maximum Horizontal Stress	MPa	45.74
Injection Rate	m^3/min	3.18
Injection Time	min	60
Fluid Viscosity	cp	5
Leak-off Coefficient	$m/s^{0.5}$	0.00009
Interval Thickness	m	21.336

Figure 3.4 schematically illustrates the hypothetical responses of a DAS cable attached to an offset monitoring well during a single-cluster hydraulic fracturing treatment. Based on the fracture-induced deformation, when the fracture tip is far away

from the monitoring well (i.e., Time 1), the cable is slightly extended over a wide range because of rock deformation induced by the approaching fracture. As the fracture approaches the monitoring well, the extension region detected by the cable gradually decreases but the magnitude becomes larger, as illustrated by the cable responses from Time 1 to Time 2 in Figure 3.4. Right at the time when the fracture encounters the monitoring well, the cable on the fracture is still extended because of fracture opening, whereas the cable sections on both sides of the fracture are suddenly changed to be compressed, as illustrated by the cable response at Time 3. Similar behaviors are observed during Time 4 as the fracture continues propagating. Once injection stops, the fracture starts closing because of fluid leakoff. Correspondingly, rock deformation starts releasing and the magnitude of fracture-induced deformation decreases, such that the extended cable section on the fracture would show a compressing trend while the compressed sections on the sides of the fracture produce an extending signature. In this dissertation, the analysis is focused on the fluid-injection phase of hydraulic fracturing treatments. The post-fracturing stage (i.e., fracture closure during Time 5 in Figure 3.4) is recommended to be investigated in future studies.

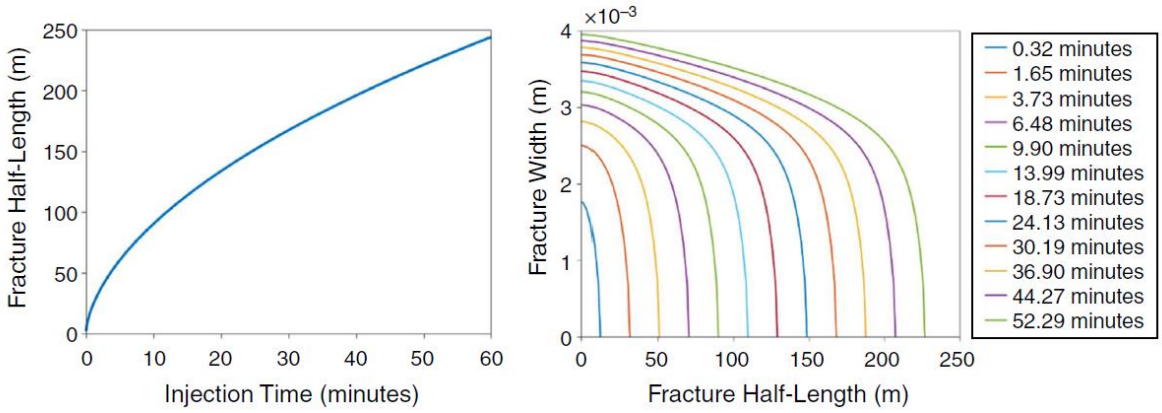

(a) (b)

Figure 3.2 (a) Fracture half-length as a function of injection time and (b) fracture-width profiles at different injection times (reprinted from Liu et al. 2020d).

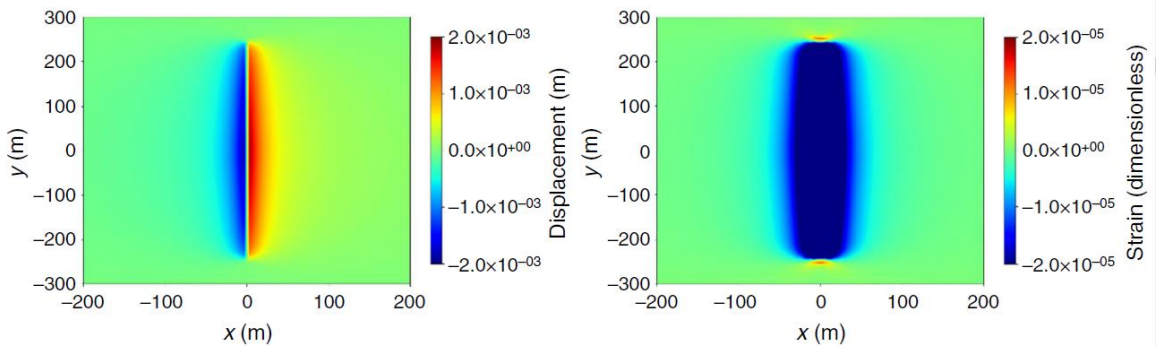

(a) (b)

Figure 3.3 (a) Fracture-induced displacement field and (b) strain field along the *x*-direction (reprinted from Liu et al. 2020d).

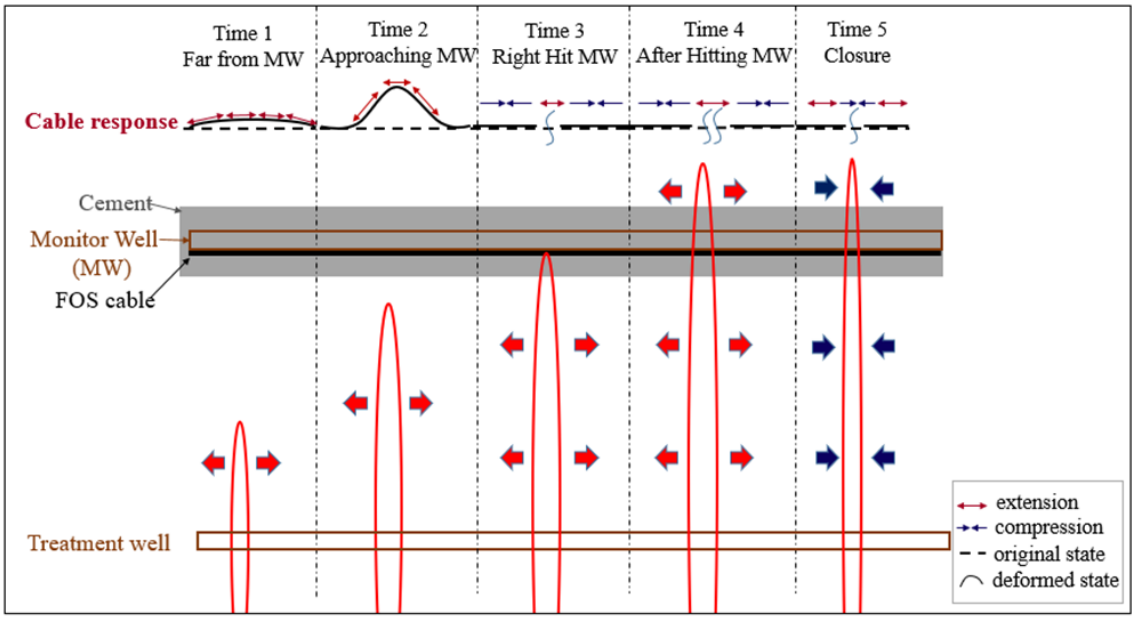

Figure 3.4 Schematic of different DAS cable responses during a single-cluster hydraulic fracturing treatment. FOS = fiber-optic sensing (reprinted from Liu et al. 2020d).

Figure 3.5 shows the directional displacement, strain, and strain rate as a function of time (i.e., waterfall plots) along the monitoring wells with offset distance of 100 (MW1), 150 (MW2), and 200 m (MW3). In general, the waterfall plots present distinct characteristics before and after fracture hit (labeled by white dashed lines), consistent with the hypothetical responses illustrated in Figure 3.4. The displacement plots (plots in the first row of Figure 3.5) show a pronounced response after the fracture encounters the monitoring well because the rock on two sides of the fracture is compressed apart from each other. In all strain waterfall plots (plots in the second row of Figure 3.5), red colors indicate extension with positive magnitudes and blue colors mean compression with

negative magnitudes. The heart-shaped extension zone in the strain waterfall plot corresponds to the progressively narrowing extension detected by the DAS cable before fracture hit. After the fracture encounters the monitoring well, the section of the fiber on the fracture keeps being extended as indicated by the red line, whereas blue regions represent the compressed sections of the fiber on both sides of the fracture. The relative strain variations between two adjacent time steps (i.e., strain rate) are demonstrated in figures in the last row of Figure 3.5. Red colors indicate increasing extension or decreasing compression, whereas blue colors mean increasing compression or decreasing extension. The heart-shaped extending zone before the fracture hit indicates that the magnitude of extension keeps increasing as the fracture tip gets closer to the monitoring well. After the fracture hit, a two-wing compressing zone is observed, illustrating that large compressional strain change occurs on both sides of the growing fracture. As the fracture propagates away from the fiber, the magnitude of compressional strain still increases, but the increasing rate decays with time and the compressional strain is finally stable and keeps constant. The corresponding signature is the decreasing dimension of the compressing zone in the location axis as injection time increases, which is caused by less significant fracture-induced strain variations detected by the monitoring wells between adjacent time steps. This is also evidenced by Figure 3.2, which shows that the growth of fracture width keeps decreasing as injection time increases, resulting in less strain perturbations.

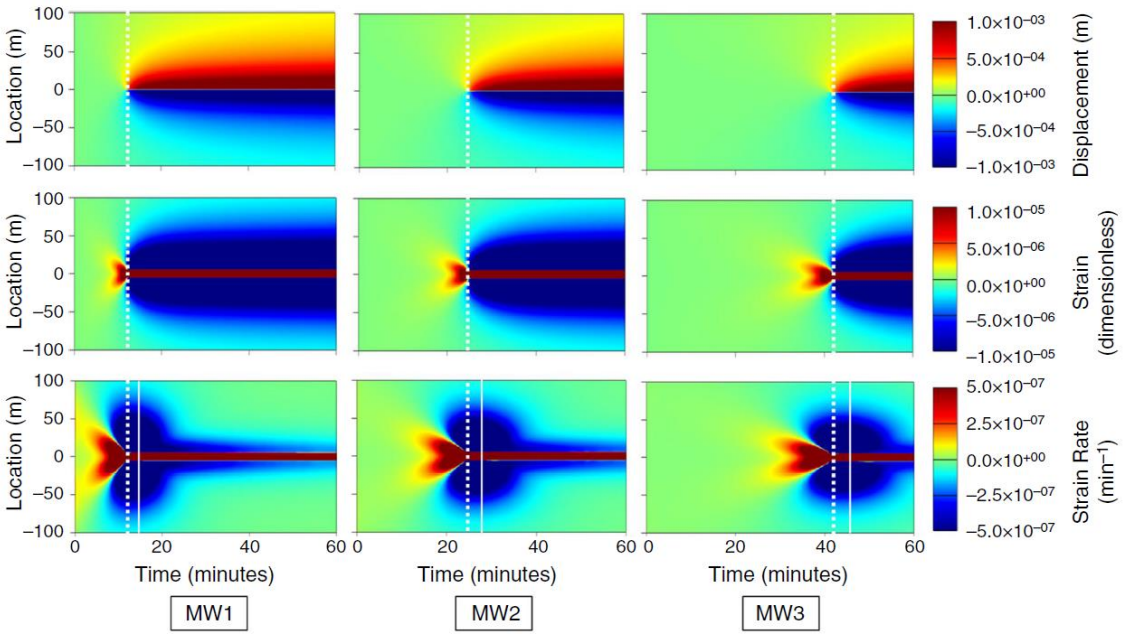

Figure 3.5 Waterfall plots of displacement, strain, strain rate along the three monitoring wells for the base case. The first column corresponds to Monitoring Well 1 (MW1), the second column corresponds to Monitoring Well 2 (MW2), and the third column corresponds to Monitoring Well 3 (MW3). The plots in the first row are displacement plots, whereas the plots in the second and third rows are strain and strain-rate plots, respectively. The gauge length is 10 m (reprinted from Liu et al. 2020d).

Another interesting observation by comparing the strain-rate waterfall plots of the three monitoring wells (i.e., figures in the last row of Figure 3.5) is that different sizes of the two-wing compressing zone are created. The size of the compressing zone in the location axis becomes smaller, whereas the size in the time axis becomes larger as the offset distance increases. To facilitate a quantitative comparison of the difference among the three wells, the strain rates as a function of time at three different locations (labeled in

Figure 3.1) in each well are given in Figure 3.6(a) to Figure 3.6(c). In Figure 3.1, A1, A2, and A3 are on the fracture at the three monitoring wells; B1, B2, and B3 are 10 m away from the fracture; and C1, C2, and C3 are 20 m away from the fracture. In addition, the strain-rate variations with respect to location at the time when the maximum dimension in the location axis is achieved (T_e, labeled by the white solid lines in Figure 3.5) are presented in Figure 3.6(d).

At the fracture hit point (i.e., A1, A2, A3) (Figure 3.6(a)), the strain rate is always a positive value, which means that the extensional strain keeps increasing during fracture propagation. Moreover, Figure 3.6(a) indicates that there is a big strain jump when the fracture hits the monitoring well, and then the strain rate shows a decreasing trend. Because of the small color bar range used in the waterfall plots, this sharp jump and decrease of strain rate at the fracture hit point generally are not visible.

At Points B and C, the strain rate is positive and increasing before fracture hit, whereas it becomes negative and gradually increasing back to zero after fracture hit, as shown in Figure 3.6(b) and Figure 3.6(c). In addition, it takes longer for the strain rate to increase back to zero as the offset distance increases, indicating that the fracture propagation speed tends to decrease, which is consistent with the decreasing slope of fracture half-length growth plot in Figure 3.2(a). Figure 3.6(d) shows that at time T_e for three monitoring wells, the strain rate observed at the monitoring well with the smallest offset distance (i.e., MW1) is the largest. The dimension of the nonzero strain rate along the fiber becomes shorter as the offset distance increases. The difference is attributed to

the change of fracture opening between adjacent time steps. As illustrated in Figure 3.2(b), there is relatively larger width growth over each time interval during the early injection period, and a larger fracture width growth would result in a larger strain rate, which further induces a longer affected dimension along the fiber with nonzero strain rates.

The previous analyses indicate that the characteristic signatures of the induced deformation, especially the strain-rate variations over time, are highly dependent on the features of the propagating fracture. Thus, it is necessary to have comprehensive studies of the impacts of fracture geometry on strain-rate characteristics for better interpretation of the LF-DAS signals.

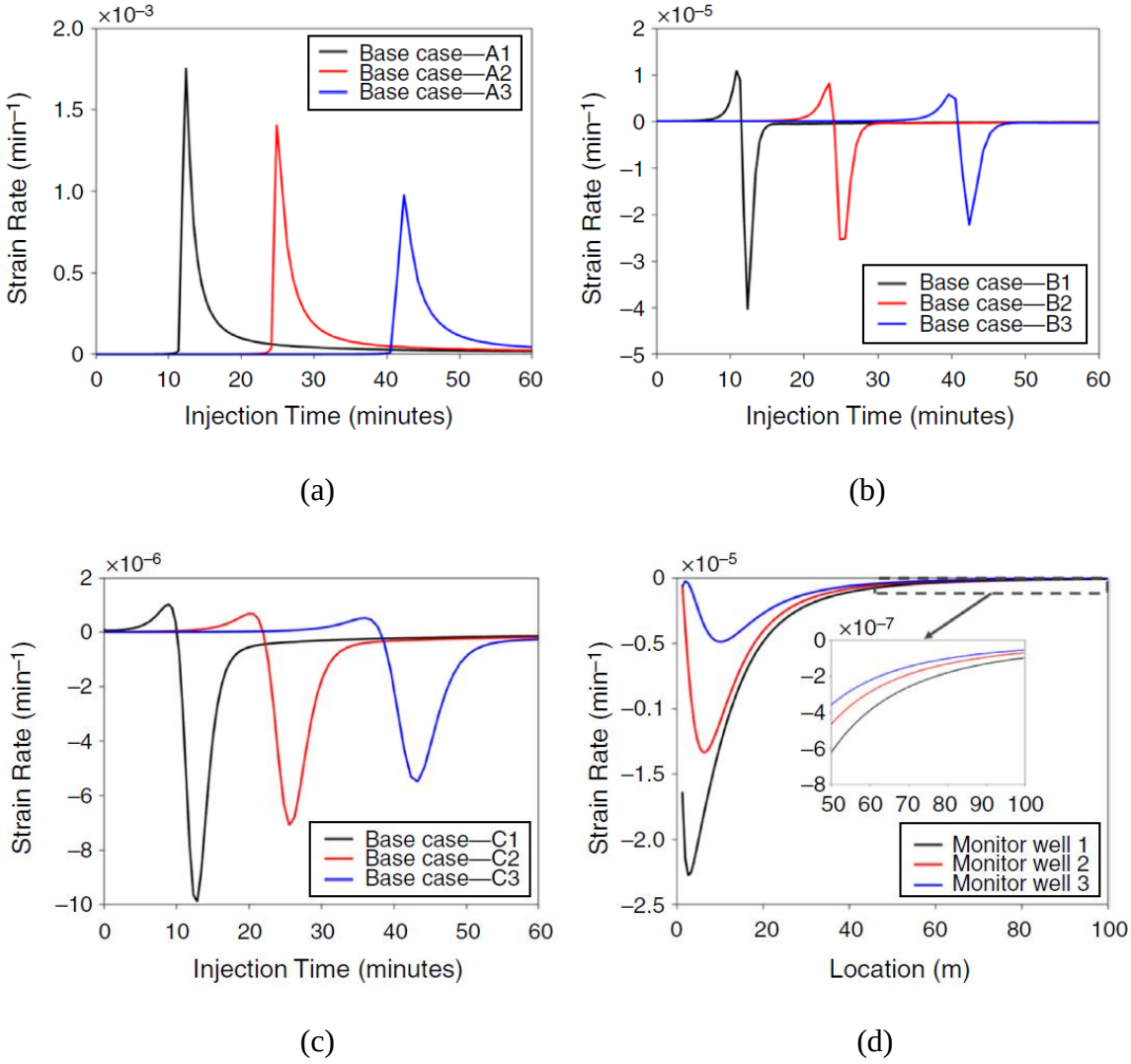

Figure 3.6 Comparison of strain rates as a function of injection time at (a) Locations A1, A2, and A3; (b) Locations B1, B2, and B3; and (c) Locations C1, C2, and C3; and (d) comparison of strain rate as a function of location at time T_e of the three different monitoring wells. Black curves correspond to Monitoring Well 1; red curves correspond to Monitoring Well 2; blue curves correspond to Monitoring Well 3 (reprinted from Liu et al. 2020d).

3.3 Impacts of Fracture Width

To investigate the impacts of fracture width on LF-DAS measurements, another two cases (Cases 1 and 2) are constructed. Comparing with the base case, Case 1 has larger fracture width and Case 2 has smaller fracture width. The leakoff coefficient is adjusted to make the fracture length the same as the base case (i.e., 0.000076 $m/s^{0.5}$ for Case 1 and 0.000095 $m/s^{0.5}$ for Case 2). The fluid viscosity used in Case 1 and Case 2 is 50 and 1 cp, respectively, and the other parameters are the same as the base case, as presented in Table 3.1. The final fracture-width profiles of the base case, Case 1, and Case 2 are compared in Figure 3.7.

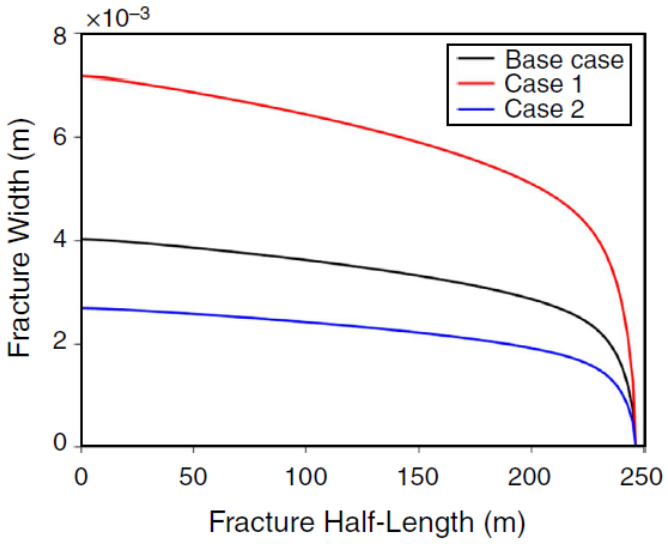

Figure 3.7 Comparison of fracture-width profiles at the end of injection of the base case, Case 1 and Case 2 (reprinted from Liu et al. 2020d).

Figure 3.8 shows the strain-rate waterfall plots along the monitoring well with 150-m offset distance (MW2) of Case 1 and Case 2. Compared together with the strain-rate waterfall plot of MW2 in Figure 3.5 under the same color bar range, the shapes of the signatures are similar among the three cases, but the sizes are dependent on the fracture-width profile. The largest nonzero strain-rate region in the waterfall plot is observed in Case 1 with the widest fracture opening, whereas the smallest region is shown in Case 2 with the smallest fracture width. Figure 3.9(a) to Figure 3.9(c) compare the time serial strain-rate data at the same three locations as the base case along MW2. Clearly, Point A2 experiences more severe strain perturbation as the fracture width increases. Figure 3.9(b) and Figure 3.9(c) confirm that, for locations off the fracture path, both the extending strain rate before fracture hit and the compressing strain rate after fracture hit are enlarged when the fracture width becomes larger. Moreover, Figure 3.9(d) compares the strain rate at T_e among the three cases, indicating that larger fracture width induces more pronounced strain variation at the same location.

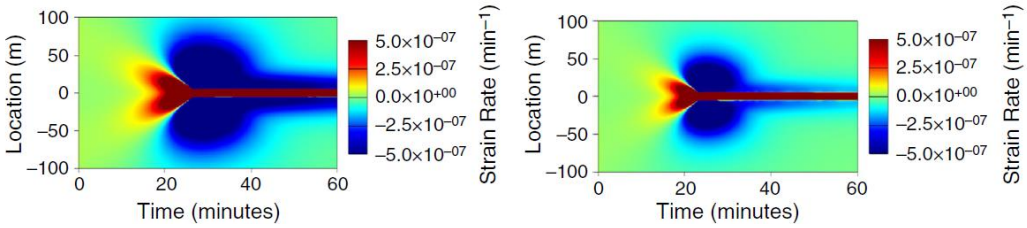

(a) (b)

Figure 3.8 Strain-rate waterfall plots along the monitoring well with an offset distance of 150 m for (a) Case 1 and (b) Case 2. The gauge length is 10 m (reprinted from Liu et al. 2020d).

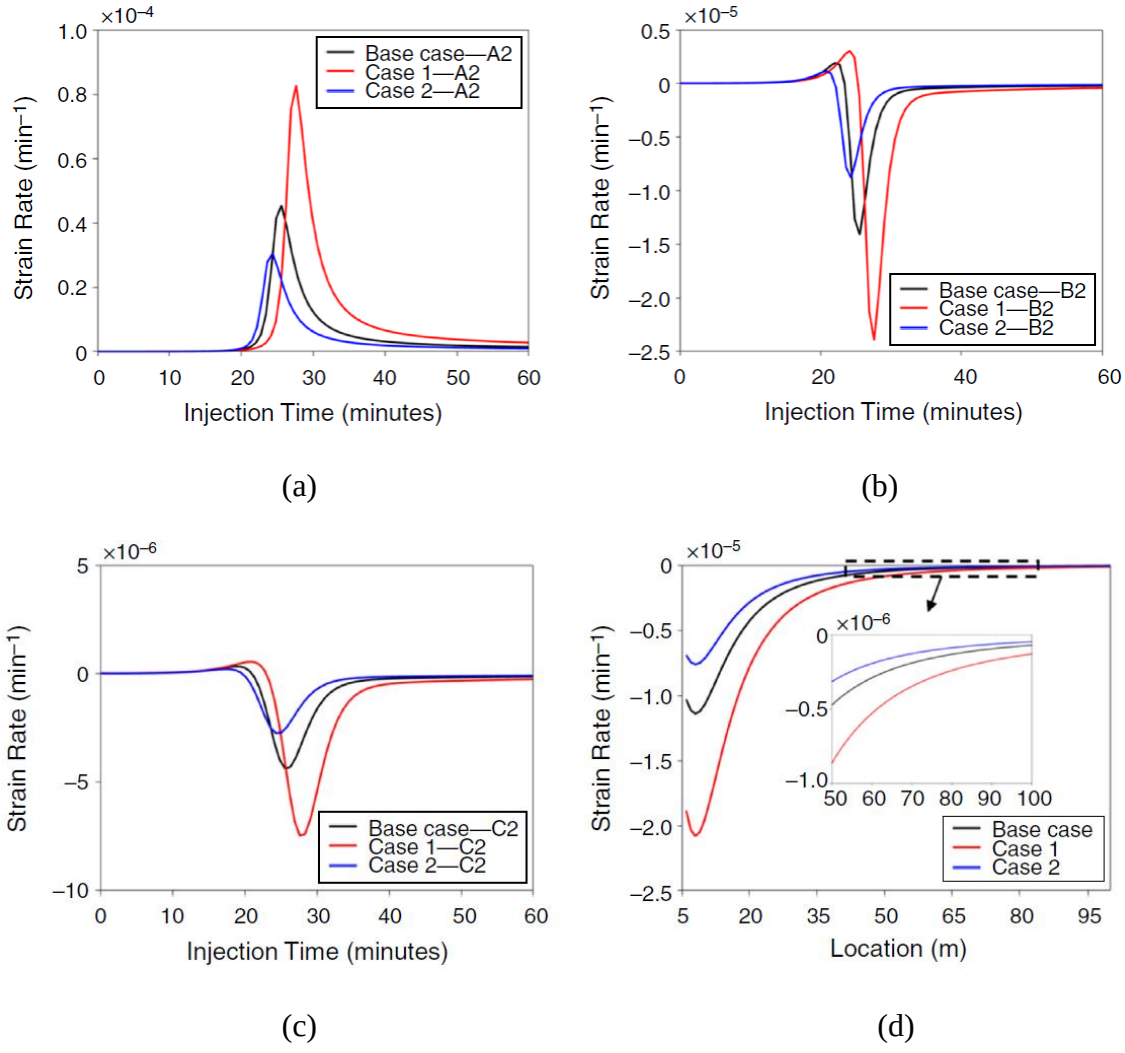

Figure 3.9 Comparison of strain rates as a function of injection time at (a) Location A2, (b) Location B2, and (c) Location C2; and (d) comparison of strain rate as a function of location at time T_e among base case (intermediate fracture width, black curve), Case 1 (large fracture width, red curve), and Case 2 (small fracture width, blue curve) (reprinted from Liu et al. 2020d).

3.4 Impacts of Fracture Height

In this section, the effects of fracture height on the characteristic signatures in the strain-rate waterfall plot are investigated. Different from the base case with a constant fracture height of 21.336 m, the fracture height is changed to 10 m in Case 3 and 40 m in Case 4. Again, the leakoff coefficient is tuned to make the fracture and width almost identical, so their impacts could be minimized. Specifically, the leak-off coefficient is 0.00021 $m/s^{0.5}$ in Case 3 and 0.000039 $m/s^{0.5}$ in Case 4.

The strain-rate waterfall plots of Case 3 and Case 4 are presented in Figure 3.10. Similar to the effects of fracture width, larger fracture height results in larger nonzero strain-rate region in the waterfall plot. In addition, the propagating fractures with different heights generate various signatures on the strain-rate plot. After the fracture hit, the region in the vicinity of the fracture becomes less compressed for the higher fracture indicated by the strain rates with less absolute values in Figure 3.10(b). This is because fracture segments away from the monitoring well with larger fracture height could induce larger extension along the direction of the horizontal monitoring well and result in less overall compression in the fiber near the fracture.

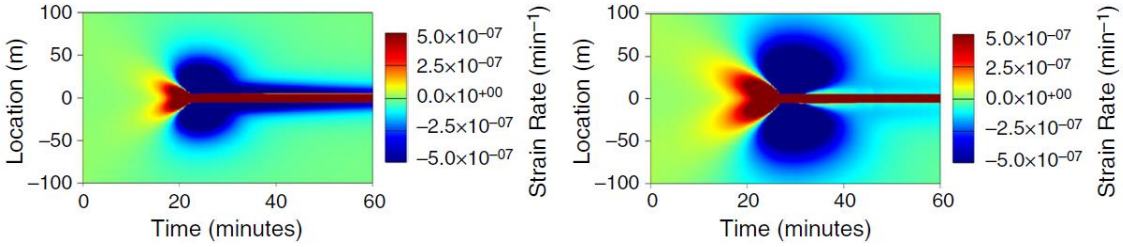

(a) (b)

Figure 3.10 Strain-rate waterfall plots along the monitoring well with an offset distance of 150 m for (a) Case 3 and (b) Case 4. The gauge length is 10 m (reprinted from Liu et al. 2020d).

Figure 3.11(a) shows the strain-rate values as a function of injection time at A2, illustrating that fracture height has trivial impacts on strain-rate magnitude at the location of fracture hit on the fiber. Only slight differences are observed that could be caused by the small variations of the fracture width among the three cases. Figure 3.11(b) and Figure 3.11(c) indicate that fracture height has more complicated impacts along the fiber sections off the fracture path. Before the fracture hit, the maximum strain rates observed at B2 and C2 both show an increasing trend as the fracture height increases. After fracture hit, strain rate detected at different locations responds differently to the fracture height, as indicated by the different trends of strain rate observed at B2 and C2. As illustrated by the strain rate vs. location at time T_e in Figure 3.11(d), when the fracture height is smaller, the magnitude of strain rate increases in the vicinity of the fracture, but it decreases back to zero within a relatively shorter distance away from the fracture. On the contrary, when the

fracture height is increased, the maximum absolute value of strain rate decreases, but it takes a longer distance to return to zero.

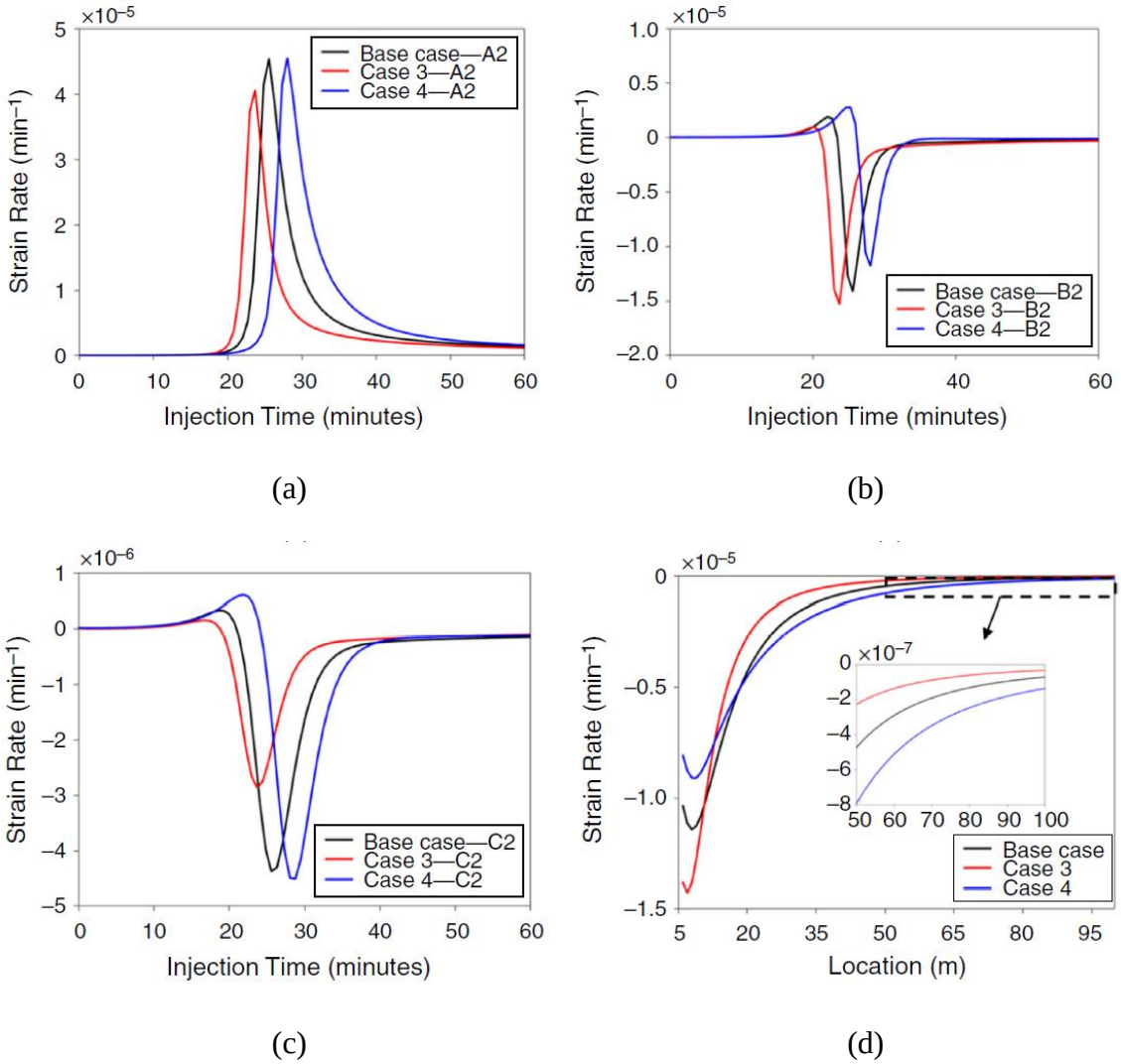

Figure 3.11 Comparison of strain rates as a function of injection time at (a) Location A2, (b) Location B2, (c) Location C2; and (d) comparison of strain rate as a function of location at time T_e among base case (intermediate fracture height, black curve), Case 3 (small fracture height, blue curve), and Case 4 (large fracture height, red curve) (reprinted from Liu et al. 2020d).

In summary, before the fracture hit, variation of strain rate at the two sides of the fracture is mainly affected by rock deformation in the direction along the monitoring well as the fracture approaches, whereas after the fracture hit, the variation is also influenced by the compression on the fiber induced by fracture opening at the fracture-hit location in addition to the fracture-induced rock deformation along the fiber as the fracture tip grows away from the fiber.

3.5 Impacts of Fracture Height Growth

Instead of propagating with constant height, a hydraulic fracture may grow gradually as well in the vertical direction. In Case 5, the impacts of fracture height growth on the strain-rate signatures are examined. The initial fracture height is set to be 6 m at the fracture tip and gradually grows to the maximum height that is equivalent to the height of the base case. The fracture height evolution is presented in Figure 3.12.

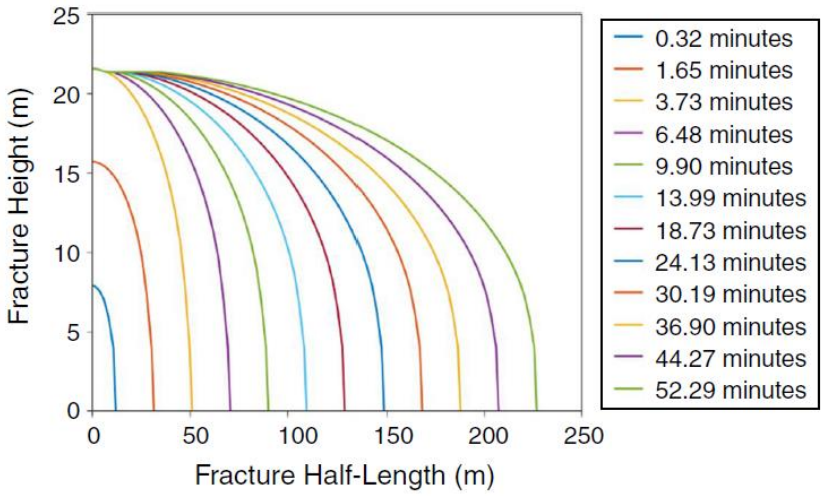

Figure 3.12 Fracture height as a function of fracture half-length at different injection times of Case 5 (reprinted from Liu et al. 2020d).

Figure 3.13 illustrates the strain-rate waterfall plot of Case 5 observed at MW2. Compared with the base case (Figure 3.5), because of the small initial fracture height at the propagating fracture tip, the heart-shaped extending zone is relatively smaller in Case 5. Moreover, as shown in Figure 3.13 the shape of the compressing zone is changed when the fracture height growth is considered, and the decreasing trend of the nonzero strain-rate dimension is smoother because of the gradual height change during fracture propagation. Another obvious difference in the strain-rate signatures is that the region in the vicinity of the fracture becomes less compressed and shows near-zero strain rates after the fracture hit. As explained in the Impacts of Fracture Height section, larger fracture height could induce more extension in the vicinity of the fracture, so the growing fracture height generates a more pronounced extending signature in the later injection time because the fracture height keeps changing in each timestep.

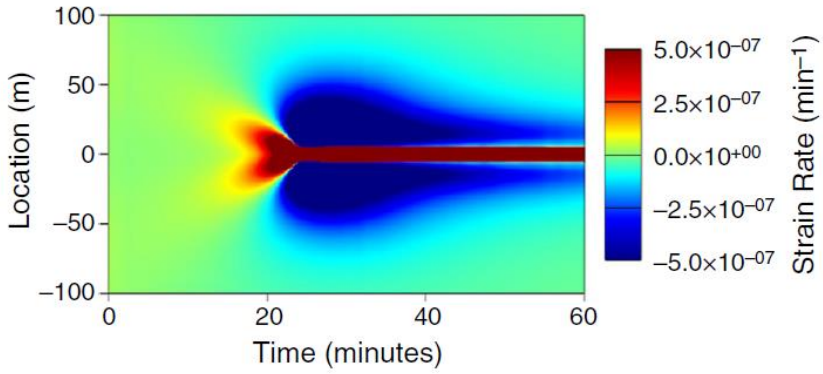

Figure 3.13 Strain-rate waterfall plot along the monitoring well with an offset distance of 150 m for Case 5. The gauge length is 10 m (reprinted from Liu et al. 2020d).

3.6 Interpretation of a Field Case

The goal of Cases 1 to 5 is to understand the mechanisms of strain and strain-rate responses from LF-DAS and their corresponding features of fracture hits and fracture geometry. The results of Cases 1 to 5 provide critical guidelines for field data interpretation. In this section, a field case in the BC Montney, Groundbirch (Case 6) presented in Ugueto et al. (2019) is simulated, and the strain-rate waterfall plot for a case of simultaneous four-fracture propagation is interpreted.

Based on the given information from Ugueto et al. (2019) and assumed values for the variables missing in the paper, a case with four fractures propagating simultaneously is simulated, and the resultant fracture geometry and waterfall plots of displacement, strain, and strain rate along a parallel horizontal monitoring well with 200-m offset distance are presented. The cluster spacing, injection rate, and injection time are referred from Ugueto et al. (2019), which are listed in Table 3.2 together with some assumed fluid and reservoir properties. The field-measured strain-rate waterfall plot (Figure 3.14(a)) provided by Ugueto et al. (2019) is interpreted based on our simulation results. It is worth mentioning that in this study only the strain-rate waterfall plot during injection for the fracturing treatment is interpreted.

Table 3.2 Summary of completion and reservoir parameters for Case 6 (adapted from Liu et al. 2020d).

Parameter	Unit	Value
Cluster Number	-	4
Cluster Spacing	m	50
Injection Rate 1	m^3/min	1.5
Injection Time 1	minutes	15
Injection Rate 2	m^3/min	6.5
Injection Time	min	90
Fluid Viscosity	cp	50
Initial Fracture Height	m	40
Interval Thickness	m	100

Although the intention is not to history match the real LF-DAS data because of the lack of detailed completion/reservoir data, our simulation result does capture the main characteristics observed in the real data by comparing Figure 3.14(a) and Figure 3.14(b). Based on our simulated strain-rate waterfall plot, two primary features of fracture hits can be observed: shrinkage of the extending zone from a heart shape to a line; and appearance of compressing zone at two sides of the fracture on the fiber. It is important to know that a line of the extending zone after fracture hits becomes a wide band in the field-measured plot because of the low measurement resolution. Although these features cannot be obviously detected in the measured strain-rate waterfall plot because of the measurement

resolution and unavoidable noise, the size change of the red extending zone in the location axis still can be identified when the fracture hits the fiber. As shown in Figure 3.14, the transition in size of each fracture is labeled by the white solid lines and the fracture-hit time is labeled by the white dashed lines. According to our simulation result, fracture-hit time is at the moment of size shrinkage of the extending zone instead of the moment when the extending zone appears as discussed in Ugueto et al. (2019).

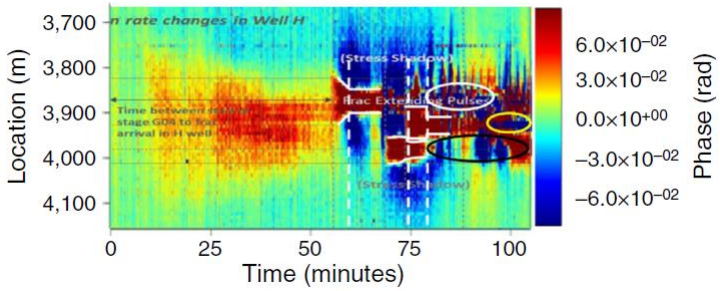

(a)

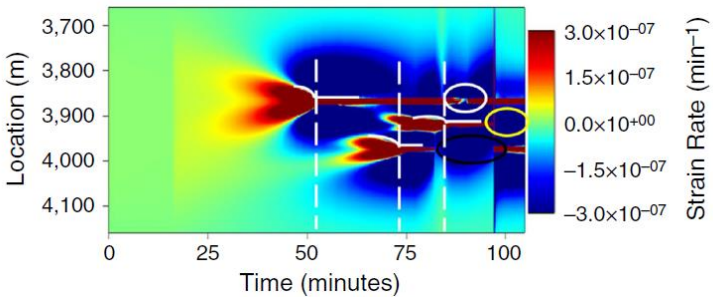

(b)

Figure 3.14 (a) Waterfall plot of real LF-DAS data modified from Ugueto et al. (2019) and (b) strain-rate waterfall plot along the monitoring well with an offset distance of 200 m for Case 6. The gauge length in (b) is 10 m (reprinted from Liu et al. 2020d).

As shown in Figure 3.14(a), the measured strain-rate waterfall plot also shows some other features after fracture hits, which are labeled in the black, yellow, and white circles. As labeled in the black circle, the red extending zone of Fracture 4 is not continuous, which is not consistent with the results of Cases 1 to 5. One possible interpretation for this observation is that the fracture stops propagating at a certain time and restarts to propagate later. Based on this hypothesis, during the simulation of fracture propagation, Fracture 4 is stopped after injecting 80 minutes and resumed to propagate after 20 minutes because of the uneven fluid allocation, as shown in Figure 3.15(a) of fracture half-length evolution. Figure 3.14(b) of the simulated strain rate clearly indicates that, after Fracture 4 stops propagating, the red zone of increasing extension changes to the blue zone of decreasing extension, which later changes back to the red zone of increasing extension again after Fracture 4 restarts to grow. The result proves our hypothesis and provides an interpretation for the discontinuous feature of the red extending zone along Fracture 4 in Figure 3.14(a).

A similar observation is shown in the yellow circle: the strain rate at the fracture-hit location of Fracture 3 shows a trend of decreasing extension, which is an indicator of fracture stop. As highlighted in the white circles, the strain rate at the fracture-hit location of Fracture 2 also shows a trend of decreasing extension after the fracture hit of Fracture 3. Based on our simulation results, this could be because the growth of Fracture 3 suppresses the second fracture, resulting in fracture aperture reduction within this period. Moreover, the dimension of the compressing zone in the location axis around the second

fracture is larger than that around the fourth fracture, which implies that Fracture 2 is wider than Fracture 4. Correspondingly, Figure 3.15(b) illustrates Fracture 2 has a larger width than Fracture 4, which corroborates the findings in the Impacts of Fracture Width section.

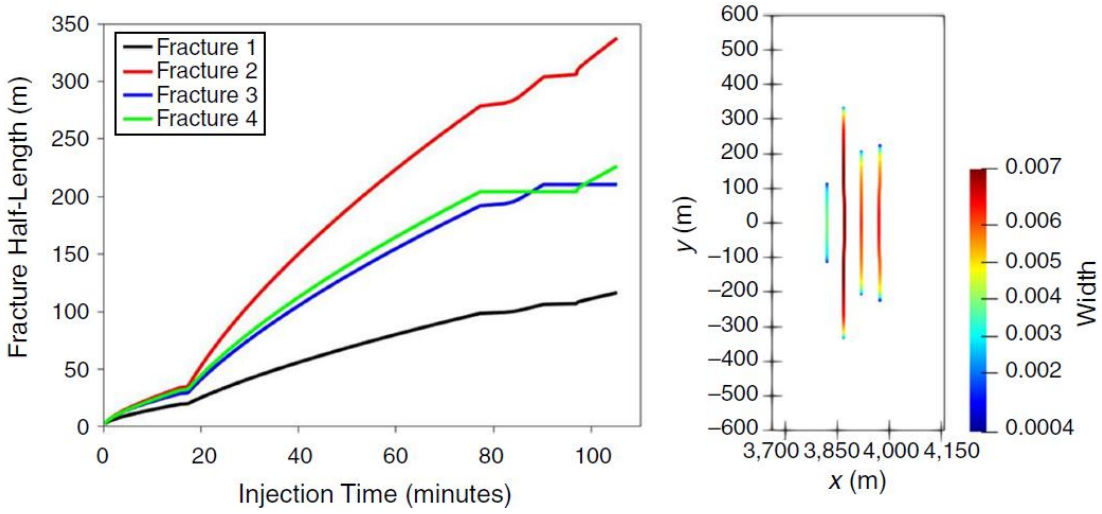

(a) (b)

Figure 3.15 Illustration of (a) fracture half-length evolution and (b) final fracture width and trajectory at the end of injection for Case 6 (reprinted from Liu et al. 2020d).

In addition, Figure 3.15(a) also indicates that the half fracture length of Fracture 1 at the end of injection is less than 200 m. Hence, only three of four fractures are detected by the monitoring well. Accordingly, no signatures associated with Fracture 1 are observed in the waterfall plots, including the displacement and strain waterfall plots presented in Figure 3.16. This observation implies that LF-DAS data may provide minimal information about fractures that do not hit the monitoring well. The relative fracture

propagation speed can also be clearly identified: Fracture 2 encounters the monitoring well first, followed by Fracture 4 and then Fracture 3. The heart-shaped extension zone induced by the third fracture is suppressed by the compression induced by the nearby two fractures, as shown in the strain waterfall plot (Figure 3.16(b)). It should be noted that the presented interpretation is just one possible realization, while the objective of the field case analysis is to testify the findings obtained from the previous synthetic case studies.

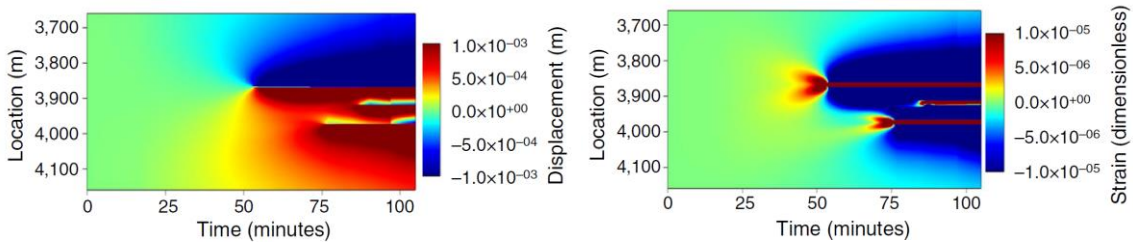

(a) (b)

Figure 3.16 (a) Displacement and (b) strain waterfall plot along the monitoring well with an offset distance of 200 m for Case 6. The gauge length is 10 m (reprinted from Liu et al. 2020d).

3.7 Summary

In this chapter, through five synthetic cases, the mechanisms and corresponding influencing factors for the LF-DAS signals were analyzed from the perspective of rock mechanics. The induced displacement, strain, and strain rate along offset monitoring wells were presented in the form of waterfall plots. Then, a field case was studies and the field-measured strain-rate waterfall plot was interpreted based on our simulated result. In the

meantime, the corresponding fracture geometry and propagating characteristics for the field case were provided. The results of this chapter help to better interpret the real-time LF-DAS data and provide critical insights into hydraulic fracture characterization using LF-DAS data.

CHAPTER 4

FRACTURE-HIT DETECTION USING COMPLEX LOW-FREQUENCY DISTRIBUTED ACOUSTIC SENSING MEASUREMENTS*

4.1 Overview

Chapter 3 demonstrated that LF-DAS data is a powerful attribute to detect fracture hits and characterize fracture geometry during multistage hydraulic fracturing treatments in unconventional reservoirs. Due to the complexity of multiple-fracture propagation in unconventional reservoirs, the measured signals from different wells exhibit various characteristics, especially when the gauge length is similar to the cluster spacing. It is necessary to relate the observed complex strain/strain-rate signatures to specific fracture patterns based on the physical model of rock deformation during fracture propagation and to quantitatively characterize signatures surrounding fracture hits.

In this chapter, we simulate simultaneous multiple-fracture propagation as well as fracture-induced strain and strain-rate responses along an offset monitoring well. Then a general guideline for fracture-hit detection is proposed based on quantitative analysis of LF-DAS measurements during multiple-fracture propagation. Finally, a set of field examples are presented to demonstrate the potential of LF-DAS data on hydraulic fracturing monitoring.

*Part of this chapter is reprinted with permission from "Fracture-Hit Detection Using LF-DAS Signals Measured during Multifracture Propagation in Unconventional Reservoirs" by Liu, Y., Wu, K., Jin, G. et al., 2020. *SPE Reservoir Evaluation & Engineering,* Preprint, Copyright [2020] by Society of Petroleum Engineers.

4.2 Detailed Characterization of Fracture-Hit Signatures

The LF-DAS data in the 2D time-channel format are transformed into three 1D features along the channel axis, which are designed to detect the fracture hits from different perspectives. The first feature is the maximum strain rate ($\dot{\varepsilon}_{\max}$) of each channel during the injection period. When the fracture hits the monitoring well, there is a significant strain perturbation and the channels within the fracture path would show an obvious strain-rate jump. The second feature is the summation of strain rate ($\dot{\varepsilon}_{\text{sum}}$) in each channel during the pumping stage, which represents the fracture-induced strain at the end of the injection phase. For this feature, channels with fracture hits should show large positive values, assuming the extension is positive. The third feature is the summation of the strain-rate magnitude (i.e. absolute value $\left|\dot{\varepsilon}\right|_{\text{sum}}$), which captures the dynamic amplitude variation during the fracture propagation process.

To aid in comparative analysis, the features are normalized by standardization, expressed as

$$f' = \frac{f - \overline{f}}{\sigma}, \tag{4.1}$$

where *f* represents a feature, $\overline{f}$ is the mean of *f*, and σ is the standard deviation of the feature *f*. After standardization, the mean of each feature is zero, while the standard deviation is one.

Two cases are constructed with different cluster spacings: 25 m in Case 1 and 12 m in Case 2. Within each case, two gauge lengths are used to calculate the strain along the monitoring well to examine its effects on the geomechanical responses and associated features for fracture-hit detection because the strain rate equivalent LF-DAS signals are dependent on the gauge length (i.e., spatial resolution) (Jin and Roy 2017b; Liu et al. 2020a). Other relevant parameters are summarized in Table 4.1.

Table 4.1 Relevant geomechanical and completion parameters for simulation cases (adapted from Liu et al. 2020b).

Parameter	Unit	Value
Young's Modulus	GPa	21.4
Poisson's Ratio	-	0.26
Minimum Horizontal Stress	MPa	41.34
Maximum Horizontal Stress	MPa	45.74
Injection Rate	m^3/min	3.18
Injection Time	min	60
Fluid Viscosity	cp	5
Leak-off Coefficient	$m/s^{0.5}$	0.00009
Interval Thickness	m	21.336

Figure 4.1 schematically illustrates the well configuration, and the well spacing is 250 m. The monitoring well installed with FOS cables could detect the induced strain perturbations generated by the fractures initiated at the treatment well.

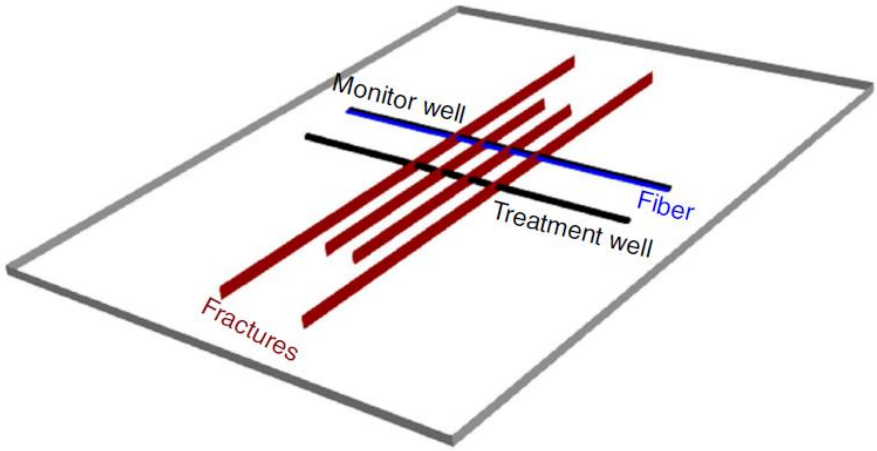

Figure 4.1 Schematic of the well configuration consisting of a treatment well and a monitoring well installed with DAS cable (reprinted from Liu et al. 2020b).

4.2.1 Case 1—Large Cluster Spacing

The final fracture geometry and fracture half-length evolution are shown in Figure 4.2, which indicates that the outer two fractures propagate faster and longer than the inner two fractures. The average widths of the outer fractures are also relatively larger than those of the inner ones, especially in the near treatment well region. Figure 4.3 shows the spatial distributions of displacement and strain components in the direction of the monitoring well. A fracture opening separates the rock on each side of the fracture in opposite directions as indicated by the displacement field in Figure 4.3(a), which results in

compression zones on both sides of the fractures and extension zones in front of the fracture tips, as shown in Figure 4.3(b). These fracture-induced rock deformation characteristics would generate distinct signatures measured by the distributed acoustic sensing fiber along the monitoring well as the fracture propagates from the treatment well. Chapter 3 presented the details regarding the mechanisms and the influencing factors for LF-DAS signals.

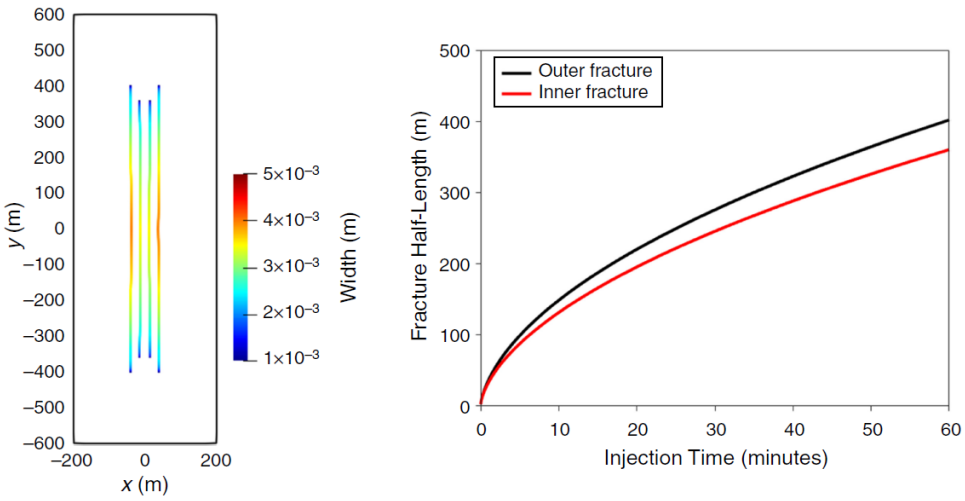

(a) (b)

Figure 4.2 (a) Final fracture geometry and (b) fracture half-length evolution as a function of injection time for Case 1 (reprinted from Liu et al. 2020b).

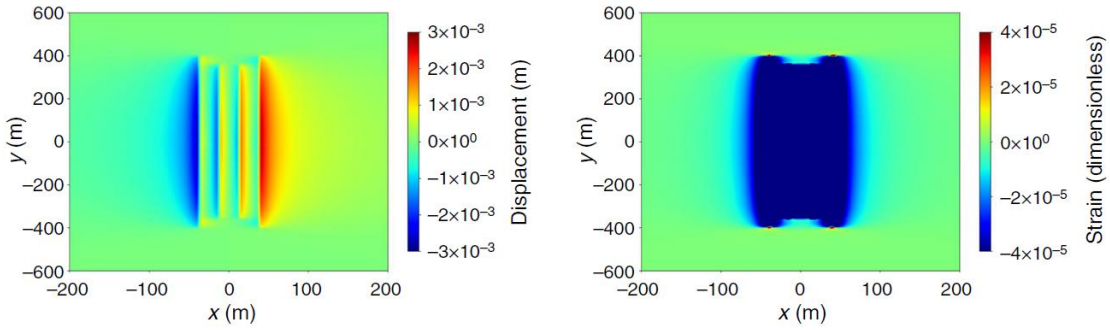

(a) (b)

Figure 4.3 Spatial distribution of (a) displacement and (b) strain in the direction of the monitoring well (i.e., *x* direction) at the end of injection (reprinted from Liu et al. 2020b).

Figure 4.4 shows the waterfall plots of strain and strain rate measured along the monitoring well with an offset distance of 250 m. The gauge length used in Figure 4.4 is 5 m. In Figure 4.4(a), there are two obvious "heart-shaped" regions corresponding to the outer two fractures, which are generated by the narrowing extension in front of the propagating fracture tips before fractures hit the monitoring well. However, the heart-shaped regions are not observed for the two inner fractures because the extension in front of the inner fracture tips is suppressed by the compression induced by the opening of the outer fractures, leading to overall compression. After the fractures encounter the monitoring well, the fiber sections within the fracture paths experience extension due to the separation of fracture surfaces, while those on the sides of the fracture paths are compressed, as indicated by the blue compression zones divided by the red extension bands in Figure 4.4(a). The strain-rate plot reflects the dynamic changes of the strain amplitude. As shown in Figure 4.4(b), the red heart-shaped signatures indicate that the

extension keeps increasing as the fracture tips approach the monitoring well. In the meantime, before the fracture hits, the fiber sections far off the fracture paths already start experiencing less extension, indicated by the blue zones on both sides of the heart-shaped regions. After the fracture hits, the red bands indicate that the extensions detected by the fiber sections within the fracture paths keep increasing as fractures continue propagating. For the fibers on the sides of the fractures, the compression magnitude keeps increasing, but the increasing trend tends to be stable as the fractures propagate, indicated by the decay signature of the blue regions after fracture hits in Figure 4.4(b).

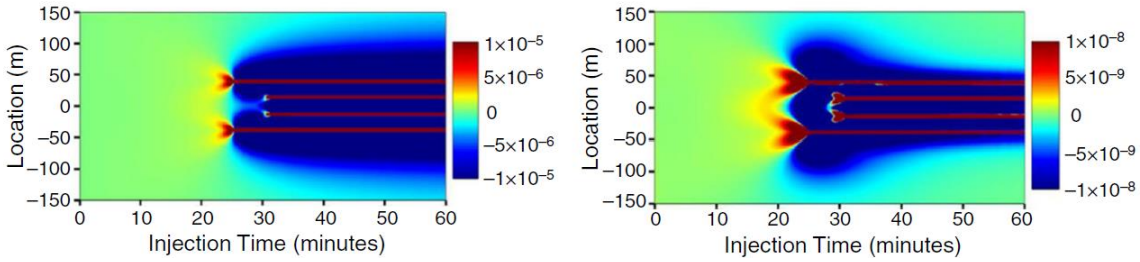

(a) (b)

Figure 4.4 Waterfall plot of (a) strain, dimensionless and (b) strain rate, s^{-1} measured by the monitoring well with an offset distance of 250 m for Case 1. The gauge length is 5 m and the sensing (sampling) distance is 1m (reprinted from Liu et al. 2020b).

Figure 4.5 shows the strain-rate waterfall plot for Case 1 with 5-m gauge length along with three features ($\dot{\varepsilon}_{\max}$, $\dot{\varepsilon}_{\text{sum}}$, and $|\dot{\varepsilon}|_{\text{sum}}$) for fracture-hit identification. In general, the three features show significant peak values at the channels where fractures hit the

monitoring well. The peak values corresponding to the inner two fractures are smaller than those of the two outer fractures because the fracture widths of the inner two fractures are relatively smaller as shown in Figure 4.2(a). Moreover, $\dot{\varepsilon}_{sum}$ plot shows a decreasing trend among the locations close to the fracture-hit locations, representing the stress-shadow regions. The smallest values are observed among locations between fracture hits because the compression in these regions is the superposition of contributions from the adjacent fractures. On the contrary, $|\dot{\varepsilon}|_{sum}$ gradually increases as the location approaches the fracture-hit location, indicating that more strain perturbation occurs in the vicinity of fractures. The signatures in Figure 4.5 analyzed above are helpful for the detection of fracture hits and the interpretation of field LF-DAS data.

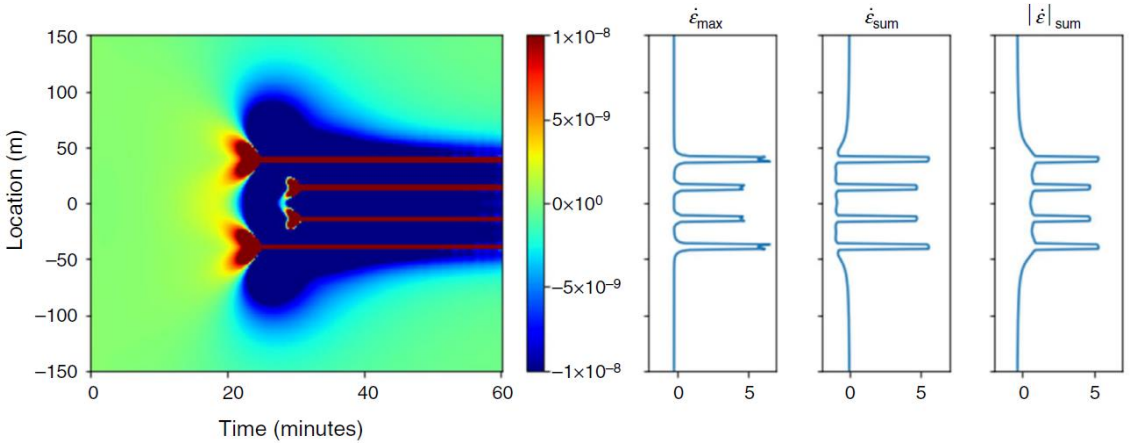

Figure 4.5 LF-DAS measured strain rate (s^{-1}) and corresponding normalized features (dimensionless) with 5-m gauge length for Case 1 (reprinted from Liu et al. 2020b).

Because the gauge length is adjustable in the field, it is necessary to investigate its impact on strain-rate signatures and related features. Figure 4.6 shows the same quantities as Figure 4.5, but the gauge length used in Figure 4.6 is 10 m. A comparison between the strain-rate waterfall plots with different gauge lengths indicates that the main differences are the widths of the red regions after fracture hits. Based on the definition of strain (Eq. (2.26)), the width of each band should equal the gauge length. It is interesting to note that the strain rates of the outer two fractures are negative over a short period of time after the inner two fractures hit the monitoring well in Figure 4.6. This is because of the interference between fractures under larger gauge length since LF-DAS data is equivalent to the linear-scaled strain rate over the gauge length. Due to the same reason, the peak values in the plots of Figure 4.6 compared with those in Figure 4.5.

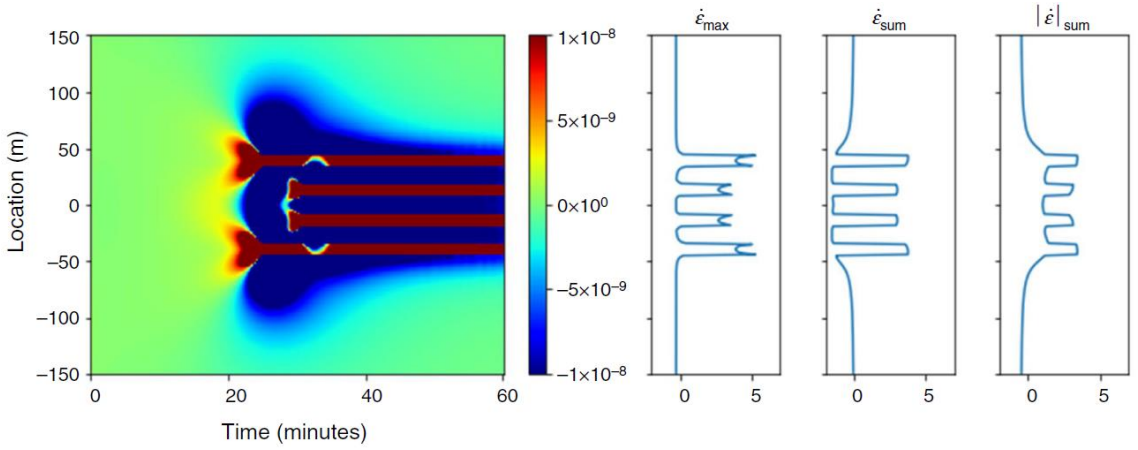

Figure 4.6 LF-DAS measured strain rate (s^{-1}) and corresponding normalized features (dimensionless) with 10-m gauge length for Case 1 (reprinted from Liu et al. 2020b).

4.2.2 Case 2—Small Cluster Spacing

The objective of constructing Case 2 is to investigate the fracture geometries and strain responses as well as the corresponding features for fracture-hit detection with relatively smaller cluster spacing because small cluster spacing is usually used in recent completion designs. Figure 4.7 shows the final fracture geometries and fracture half-length evolution for Case 2. More inter-fracture interference occurs due to the reduced cluster spacing compared with Case 1. The inner two fractures propagate slightly toward the outer fractures, which is also illustrated by the off-azimuth fracture-hit location and reduced distance between inner and outer fractures, shown in Figure 4.8.

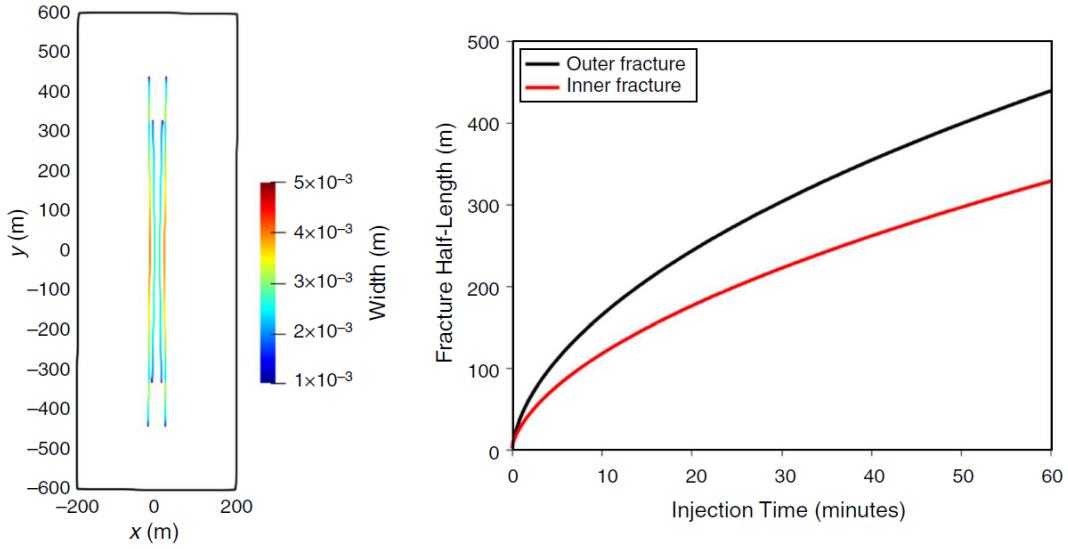

(a) (b)

Figure 4.7 (a) Final fracture geometries and (b) fracture half-length evolution as a function of injection time for Case 2 (reprinted from Liu et al. 2020b).

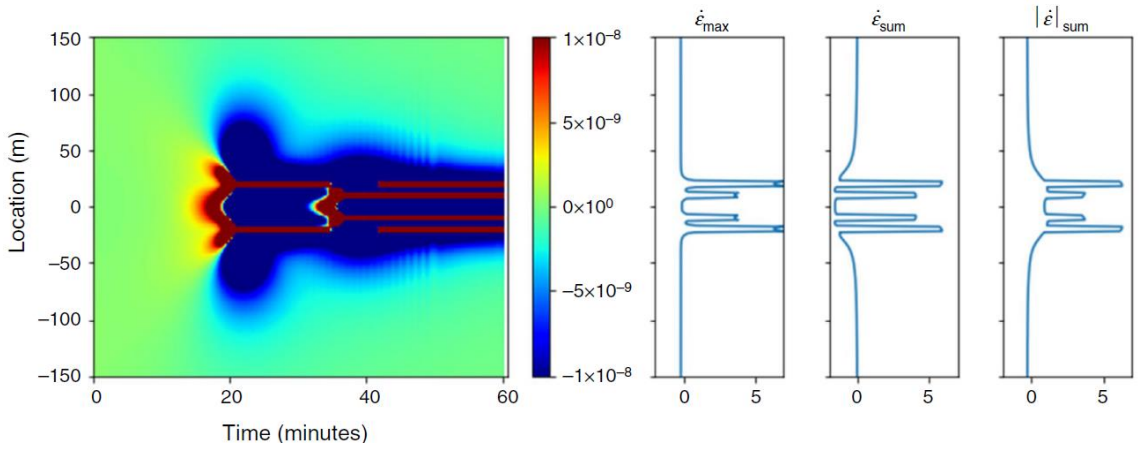

Figure 4.8 LF-DAS measured strain rate (s^{-1}) and corresponding normalized features (dimensionless) with 5-m gauge length for Case 2 (reprinted from Liu et al. 2020b).

With a 5-m gauge length, peak values are still distinguishable for each fracture in all three feature plots. However, when the gauge length is close to the cluster spacing, the red extending zones start overlapping with each other, leading to less obvious signatures for fracture-hit identification in the feature plots, as shown in Figure 4.9. Despite the small difference between the gauge length (10 m) and cluster spacing (12 m) making the peaks corresponding to the inner fractures less detectable, the channels with fracture hit still exhibit signatures that help to identify fracture hits. As labeled in red circles in Figure 4.9, there are local deflections suggesting potential fracture hits.

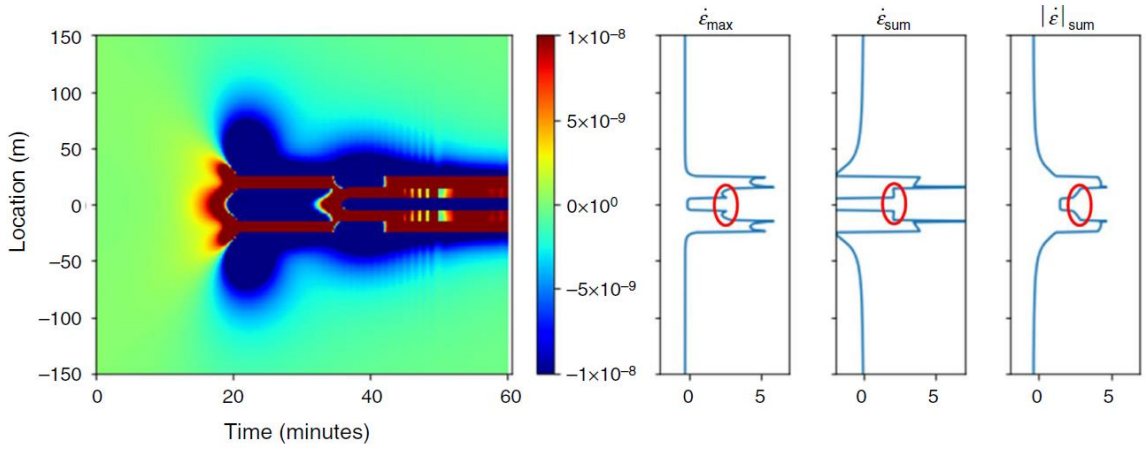

Figure 4.9 LF-DAS measured strain rate (s^{-1}) and corresponding normalized features (dimensionless) with 5-m gauge length for Case 2 (reprinted from Liu et al. 2020b).

It could be more challenging when analyzing the field LF-DAS data because of the complex reservoir/completion conditions and unavoidable noise related to DAS. The above synthetic numerical studies help to understand the dominant processes or mechanisms for the observed LF-DAS signals and provide general guidelines for fracture-hit detection, which is important for evaluating the fracture design and completion efficiency. In the following section, several field examples are analyzed based on the findings obtained from the numerical simulations.

4.3 Field Case Study

The horizontal wells investigated in this field case study were drilled in an unconventional shale formation. As shown in Figure 4.10, the two wells are in the same depth and parallel to each other and the well spacing is approximately 396.24 m (1300 ft).

The azimuth angle is approximately 140^{o} from the north. The fiber in the monitoring well (red) was installed outside of the casing and cemented in place. The DAS data recorded by the fiber during the fracturing operations of four consecutive stages in the treatment well (blue) are analyzed in this section. At each stage, eight perforation clusters were stimulated simultaneously, with cluster spacing of approximately 6.7-7.0 m (~22-23 ft). The raw DAS data are sampled with 1-m (3.281-ft) spatial sampling length and 5-m (16.40ft) gauge length. The gauge length is very close to the cluster spacing, so the feature plots might be similar to those of Case 2 with a 10-m gauge length.

The LF-DAS data, stored in the form of optical-phase change rate, are converted to strain rate following (Hartog 2017; Lindsey et al. 2020)

$$\dot{\varepsilon} = \frac{\lambda}{4\pi n_c \zeta L} \Delta\dot{\phi}, \tag{4.2}$$

where $n_c = 1.5$ is the refractive index, dimensionless; $\zeta = 0.8$ is a scalar multiplicative factor, dimensionless; λ is the probe wavelength, which is about 1550 nm; and L is the gauge length, which is 5 m in this case.

In the following discussion, the focus will be on the analysis of the low-frequency components of the DAS data and fracture-hit identification. We name the monitored four stages T1, T2, T2, and T4 in the following analysis. T1 was stimulated first, which is closest to the toe side among the four stages, while T4 was stimulated last, which is closest to the heel side.

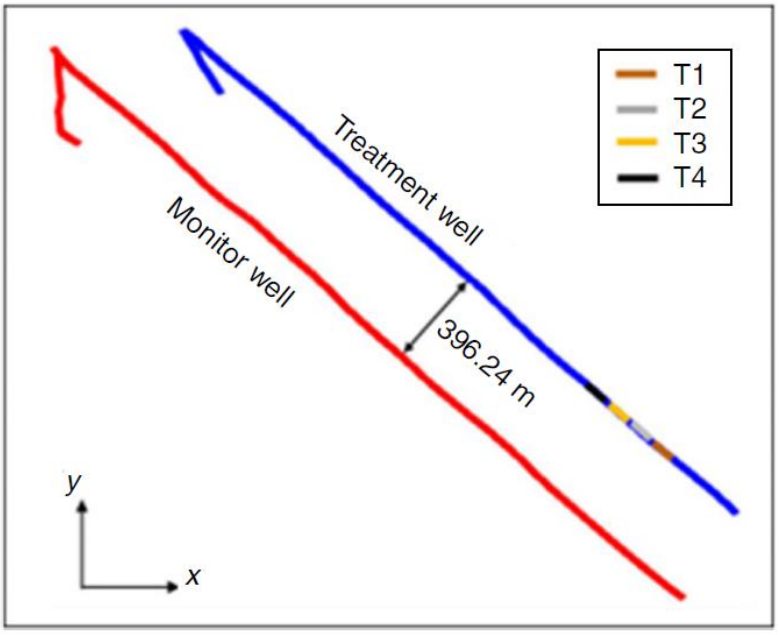

Figure 4.10 Map view of the well configuration of a well pair with a treatment well and a monitoring well (reprinted from Liu et al. 2020b).

4.3.1 Field Example One—Stage T1

The injection history of slurry rate and cumulative slurry volume of the first field example is illustrated in Figure 4.11. The average injection rate during the main stimulation period is 12.61 m^3/min and the injection stops at 107 mins.

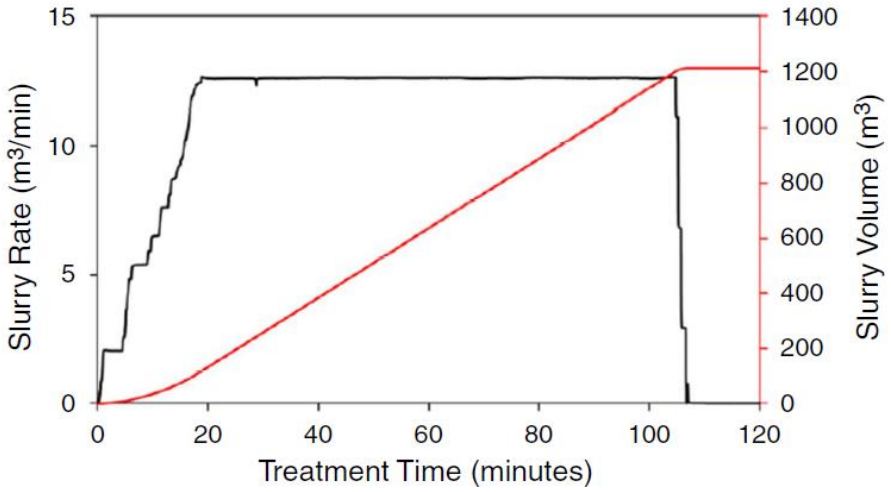

Figure 4.11 Slurry rate and cumulative slurry volume as a function of treatment time for Stage T1 (reprinted from Liu et al. 2020b).

Figure 4.12 shows the LF-DAS signals recorded at the offset monitoring well during the stimulation of stage T1 and the corresponding three feature plots. The values of the three features are calculated using the data before injection stops, as labeled by the white dash line in the waterfall plot of Figure 4.12. The location axis is the measured depth along the monitoring well. Since the gauge length (5 m) is very close to the cluster spacing (6.7-7.0 m), the feature signals overlap introducing complexity and uncertainties in detecting fracture hits. As shown in Figure 4.12, the peak value signatures in the three feature plots are not as obvious as those presented in Figure 4.5, Figure 4.6, and Figure 4.8. According to the guidelines concluded from the theoretical study, the fracture-hit locations are identified where the feature plots show local peak values or deflections. The black dash lines mark the fracture-hit locations. Most of the maximum values occur immediately after fractures encounter the monitoring well.

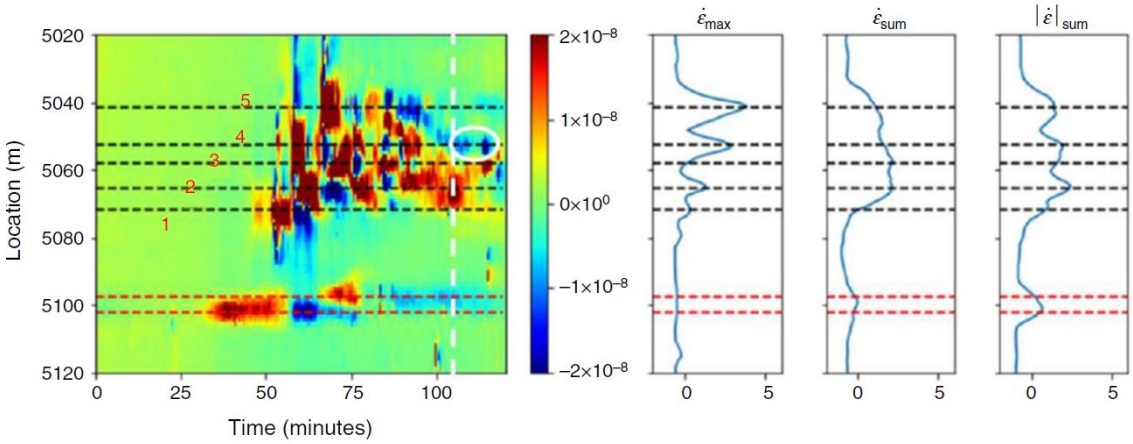

Figure 4.12 LF-DAS strain-rate data (s^{-1}) and corresponding normalized features (dimensionless) for Stage T1. Black dash lines mark the fracture-hit channels; red dash lines mark the fractures from the previous stage; the white dash line marks the time when the injection stops (reprinted from Liu et al. 2020b).

It is worthwhile to mention that the LF-DAS signals during the shut-in period also provide valuable information on fracture-hit detection. Once the injection stops, fractures may close immediately or after a period of time, depending on the pressure transient process. Fracture closure generates a clear blue band signature with negative LF-DAS values, as labeled by the white circle in Figure 4.12. This signature could serve as another constraint on fracture-hit identification. However, in the data set presented in this study, only a very short period of shut in was monitored, which limits further discussion on its potential in hydraulic fracture characterization. Another information that can be used to validate the identified fracture hits is the signals caused by the fluid leak-off into fractures of the previous stage, as labeled by the red dash lines in Figure 4.12. Fracturing fluid leak-off into fractures of the previous stage can be caused by the plug leakage, cement

debonding, or fluid pumping before the ball seat. This process could open the existing fractures, which generates obvious red extending signatures at the fracture-hit channels, usually followed by blue compressing signatures indicating fracture closure. The fractures that take the fracturing fluid should be among those identified using the LF-DAS data of the previous stage. Since the information about T1's previous stage is lacking, more details will be discussed in the following stages.

In summary, five fractures hit the monitoring well out of eight perforation clusters for stage T1, which are numbered in ascent order from the toe side to the heel side as shown in Figure 4.12. The connections between the fracture-hit position and the perforation cluster position can determine the direction of fracture propagation. If the fracture-hit number is equal to the cluster number, it is reasonable to connect on a one-to-one basis. However, in this case, the fracture hits are less than the designed clusters, which requires additional information to reduce the uncertainty in linking the fracture hits to specific clusters. The cluster corresponding to fracture hit #1 might be estimated based on the distance to the closest re-opened fracture in the previous stage. Then, other clusters can be determined based on the distance between adjacent fracture hits. For example, fracture hit #1 locates at 5071.87 m and the location of its closest re-opened fracture from the previous stage is 5097.78 m, and the distance between them is 25.91 m. Since the cluster spacing is 6.7-7.0 m, there are maybe three or four fractures in this range. Moreover, since there are still four fractures behind this first hit, it is most possible that fracture hit #1 corresponds to the third perforation cluster in the treatment well. Then other

connections can be determined by comparing the fracture-hit distance and cluster spacing. The details regarding fracture-hit location, fracture-hit time, the distance between fracture hits, and connection to perforations are summarized in Table 4.2.

Table 4.2 Fracture-hit information and the relation with perforation clusters of Stage T1 (adapted from Liu et al. 2020b).

Cluster #	Cluster spacing, m	Hit monitoring well?	Fracture-hit time, min	Fracture-hit location, m	Frac-hit Distance, m
1	-	No	-	-	-
2	6.71	No	-	-	-
3	7.01	**Yes**	52	5071.87	-
4	6.71	**Yes**	62	5065.47	6.4
5	7.01	**Yes**	70	5058.16	7.31
6	6.71	**Yes**	58	5052.67	5.49
7	7.01	No	-	-	-
8	6.71	**Yes**	66	5041.39	11.28

4.3.2 Field Example Two—Stage T2

Figure 4.13 illustrates the injection rate and slurry volume as a function of the treatment time of stage T2. The average slurry rate is 12.64 m^3/min and the total slurry volume is about 1174.76 m^3 at the end of treatment. Pumping stops after 100 minutes. Figure 4.14 shows the LF-DAS signals together with the three feature plots. The fracture hits are identified at the locations where there are local peaks or deflections, and the signatures across the three feature plots are pretty consistent. In addition, more clear band signatures along the fracture-hit locations than example 1 are observed during the shut-in period in Figure 4.14. Strong signals are also observed in the previous stage (i.e. Stage

T1), as labeled by the red dash lines. The locations marked by these lines are 5041.39 m, 5052.67 m, and 5058.16 m, respectively, which are the locations of fracture hits #5, #4, and #3 of stage T1. This consistency further confirms the adequacy and accuracy of the presented fracture-hit detection criteria.

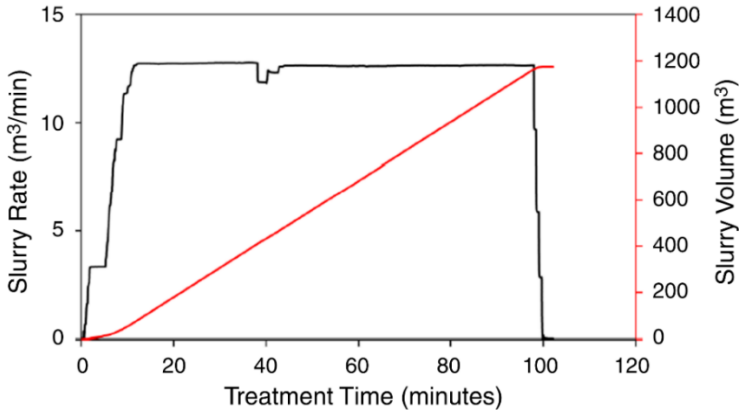

Figure 4.13 Slurry rate and cumulative slurry volume as a function of treatment time for Stage T2 (reprinted from Liu et al. 2020b).

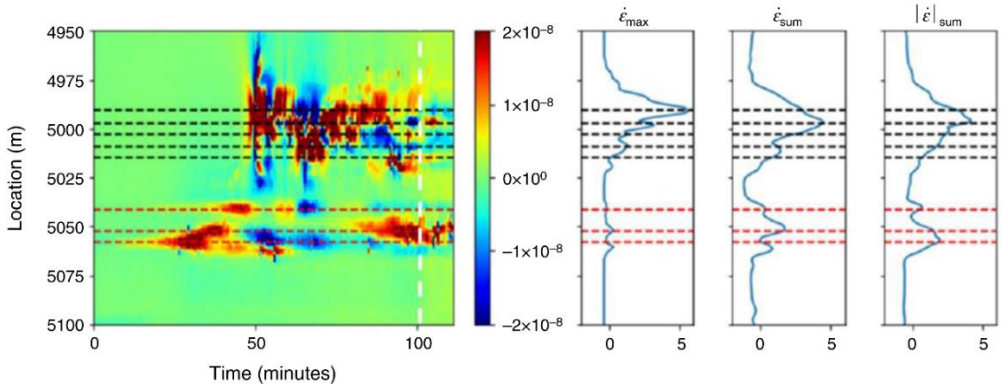

Figure 4.14 LF-DAS strain-rate data (s^{-1}) and corresponding normalized features (dimensionless) for Stage T2. Black dash lines mark the fracture-hit channels; red dash lines mark the fractures from the previous stage; the white dash line marks the time when the injection stops (reprinted from Liu et al. 2020b).

As labeled by the black dash lines in Figure 4.14, there are five fracture hits and the average distance between adjacent fracture hits is about 6.1 m that is very close to the designed cluster spacing, which indicates that the corresponding perforation clusters are in succession. The location of fracture hit #1 in stage T2 is 5014.87 m, which is about 29.56 m away from fracture hit #5 in the previous stage. Thus, fracture hit #1 is most likely related to the fourth cluster perforation of stage T2 in the treatment well. The details are summarized in Table 4.3.

Table 4.3 Fracture-hit information and the relation with perforation clusters of Stage T2 (adpated from Liu et al. 2020b).

Cluster #	Cluster spacing, m	Hit monitoring well?	Fracture -hit time, min	Fracture-hit location, m	Frac-hit Distance, m
1	-	No	-	-	-
2	7.01	No	-	-	-
3	6.71	No	-	-	-
4	7.01	**Yes**	90	5014.87	-
5	6.71	**Yes**	63	5009.39	5.48
6	7.01	**Yes**	68	5002.99	6.40
7	6.71	**Yes**	53	4997.20	5.79
8	7.01	**Yes**	48	4990.80	6.40

4.3.3 Field Example Three—Stage T3

The pumping history of stage T2 is shown in Figure 4.15. Injection with an average rate of 12.78 m^3/min stops at about 95 mins. The total injected volume is about 1168.08 m^3. The LF-DAS data and associated feature plots are illustrated in Figure 4.16. The

distance between the detected fracture hit #1 and fracture hit # 5 from the previous stage is 24.38 m, and the identified fracture hit #3 is 22.86 m away from fracture hit #4. It is likely that there are two clusters in each of these gaps, considering that the designed cluster spacing is 6.7-7.0 m. Therefore, fracture hit #1 in this stage corresponds to the third perforation cluster on the treatment well. Correspondingly, the remaining fracture hits are related to the fourth, fifth, and eighth clusters, respectively. The details about the fracture hits are summarized in Table 4.4.

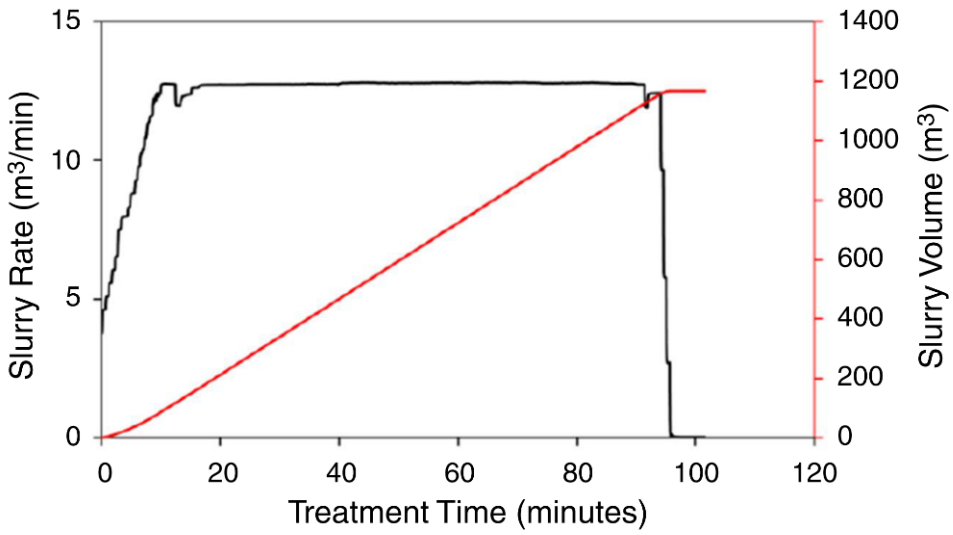

Figure 4.15 Slurry rate and cumulative slurry volume as a function of treatment time for Stage T3 (reprinted from Liu et al. 2020b).

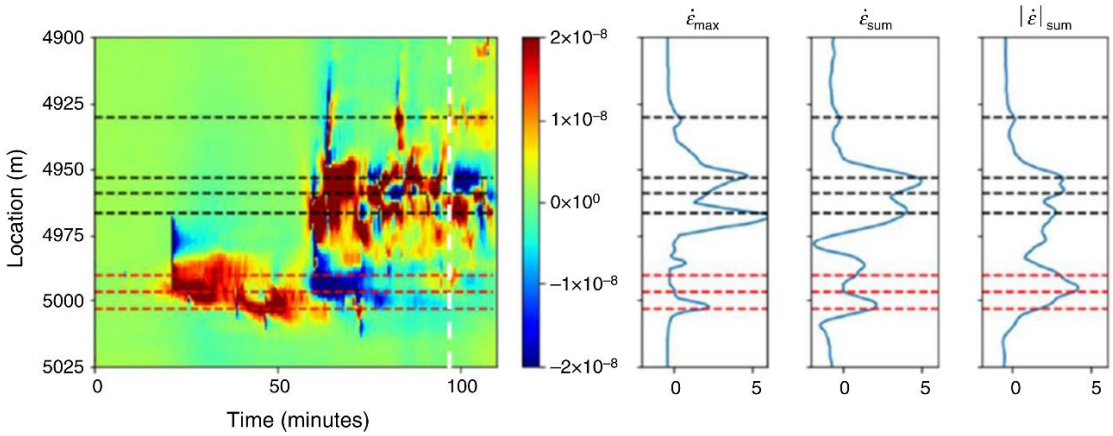

Figure 4.16 LF-DAS strain-rate data (s^{-1}) and corresponding normalized features (dimensionless) for Stage T3. Black dash lines mark the fracture-hit channels; red dash lines mark the fractures from the previous stage; the white dash line marks the time when the injection stops (reprinted from Liu et al. 2020b).

Table 4.4 Fracture-hit information and the relation with perforation clusters of Stage T3 (adapted from Liu et al. 2020b).

Cluster #	Cluster spacing, m	Hit monitoring well?	Fracture-hit time, min	Fracture-hit location, m	Frac-hit Distance, m
1	-	No	-	-	-
2	7.01	No	-	-	-
3	6.71	**Yes**	59	4966.41	-
4	7.01	**Yes**	63	4958.79	7.62
5	6.71	**Yes**	63	4953.00	5.79
6	7.01	No	-	-	-
7	7.01	No	-	-	-
8	6.71	**Yes**	82	4930.14	22.86

4.3.4 Field Example Four—Stage T4

Figure 4.17 shows the pumping profiles of stage T4. The average rate is 12.61 m^3/min and the total injection volume is 1268.24 m^3. Injection stops at about 105 mins. As shown in Figure 4.18, there are five detected fracture hits, labeled by the black dash lines. The average distance between adjacent fracture hits among the hits #1 to #4 is 9.14 m, while the distance between fracture hits #4 and #5 is 31.09 m. In addition, fracture hit #1 is 18.29 m away from the re-opened fracture closest to the heel side in the previous stage (i.e. hit #5 in T3). Considering these relative positions, fracture hit #1 of stage T4 is most likely connected with the second perforation cluster in the treatment well, and the following fracture hits from the toe to the heel correspond to clusters #3, #4, #5, and #8, respectively. The fracture-hit locations, times, and connections to the perforations are summarized in Table 4.5.

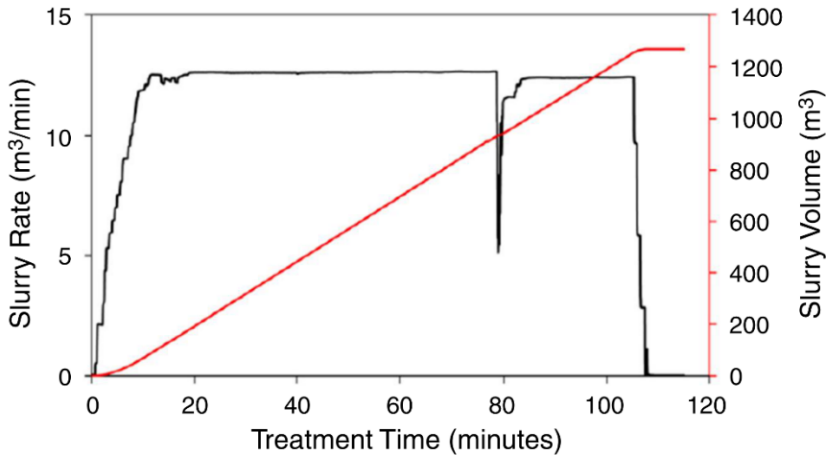

Figure 4.17 Slurry rate and cumulative slurry volume as a function of treatment time for Stage T4 (reprinted from Liu et al. 2020b).

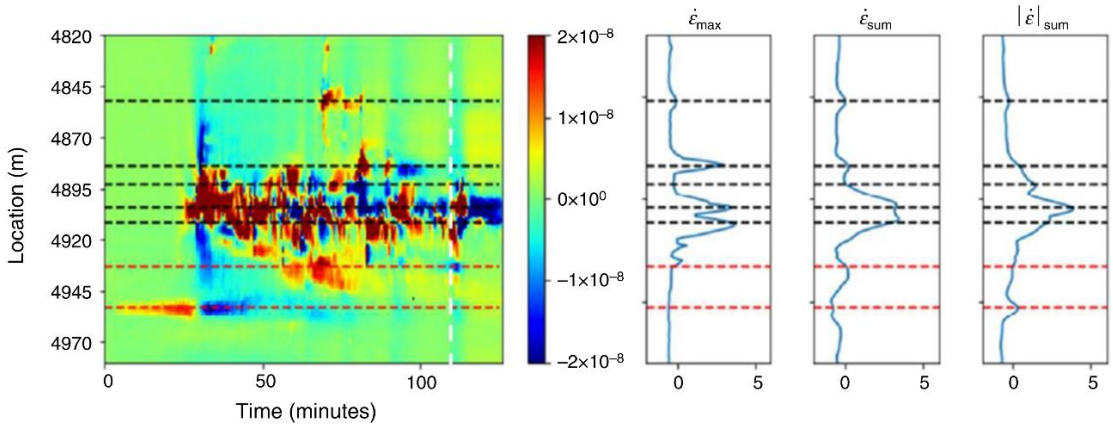

Figure 4.18 LF-DAS strain-rate data (s^{-1}) and corresponding normalized features (dimensionless) for Stage T4. Black dash lines mark the fracture-hit channels; red dash lines mark the fractures from the previous stage; the white dash line marks the time when the injection stops (reprinted from Liu et al. 2020b).

Besides, it is interesting to notice that the first fracture-hit time is much earlier than those of the other three stages. One possible reason is that there is less fracturing fluid leaking off into the previous stage. As indicated by the feather plots in Figure 4.18, both the maximum signal and accumulate signal are significantly lower than those in Figure 4.12, Figure 4.14, and Figure 4.16. Another possible reason can be attributed to the non-uniform fracturing fluid allocation. The fractures that hit the monitoring well first may propagate dominantly in the early injection period.

Table 4.5 Fracture-hit information and the relation with perforation clusters of Stage T4 (adapted from Liu et al. 2020b).

Cluster #	Cluster spacing, m	Hit monitoring well?	Fracture-hit time, min	Fracture-hit location, m	Frac-hit Distance, m
1	-	No	-	-	-
2	7.01	No	-	-	-
3	6.71	**Yes**	59	4966.41	-
4	7.01	**Yes**	63	4958.79	7.62
5	6.71	**Yes**	63	4953.00	5.79
6	7.01	No	-	-	-
7	7.01	No	-	-	-
8	6.71	**Yes**	82	4930.14	22.86

4.3.5 Fracture Azimuth Estimation

Based on the above analyses, the connections between fracture-hit locations and corresponding perforation clusters are shown in Figure 4.19. The azimuth of the well trajectory is 140^{o} from North, and the range of the fracture propagation direction is between 229^{o} and 233^{o} from North. The fractures are mainly planar and propagate nearly perpendicular to the wellbore. From the fracture-hit mapping in Figure 4.19, it can be clearly seen that the fractures from the first two toe clusters in each stage usually cannot approach the monitoring well (i.e., ‘heel-biased’ fracture pattern), which can be due to the stress-shadow effect from the previous stage.

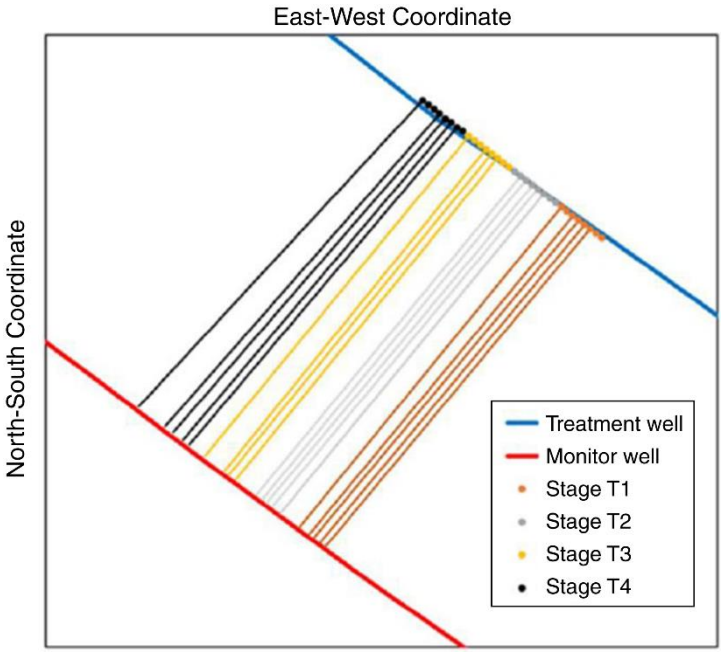

Figure 4.19 Map of hydraulic fracture azimuths. The lines connect the fracture-hit locations on the monitoring well and their corresponding perforation clusters on the treatment well (reprinted from Liu et al. 2020b).

4.4 Summary

In this chapter, the strain and strain-rate responses monitored at an offset horizontal well during multiple-fracture propagation were simulated, and a general guideline for fracture-hit detection was proposed based on the theoretical study. Then, four field examples from an unconventional shale formation were demonstrated using the proposed guideline. The theoretical study indicates that channels with fracture hits show significant peak values of the three defined features, i.e., the maximum strain rate, the summation of strain rates, and the summation of the amplitude of strain rates. Moreover, the strain-rate

signals during the shut-in period also provide valuable information on fracture-hit detection. Combining these three features and strain-rate responses of the shut-in period, we proposed a guideline for fracture-hit detection and successfully applied it to field cases.

Field LF-DAS data is much more complicated due to unavoidable complex subsurface conditions. The field examples demonstrated the applicability and accuracy of the proposed guideline for fracture-hit detection in multiple-fracture cluster completion with small cluster spacing. In the investigated formation, fractures propagate nearly perpendicular to the horizontal wellbore. The fractures of the first two clusters close to the toe side usually do not hit the monitoring well, which could be due to the stress-shadow effects induced by the previous stage. LF-DAS can also diagnose fracturing fluid leak-off into the previous stage, which is possibly due to plug leakage, cement debonding, or fluid pumping before the ball seat.

CHAPTER 5

GREEN-FUNCTION-BASED INVERSION ALGORITHM FOR QUANTITATIVE HYDRAULIC FRACTURE GEOMETRY CHARACTERIZATION*

5.1 Overview

In this chapter, an inversion algorithm is proposed, in which the strains monitored by LF-DAS along an offset horizontal well are related to the fracture widths through a Green function. The Green function is constructed based on the 3D forward geomechanical model developed in Chapter 2. The stability, accuracy, and robustness of the inversion algorithm are tested through a synthetic case with a single fracture. LF-DAS data sensitivity is investigated through Markov-chain Monte Carlo (MCMC) simulations.

In modern completion designs, multi-cluster completions with tight cluster spacings are more commonly adopted. One main challenge in the inversion of LF-DAS strain data under such circumstances is the non-unique solutions. We then extend the inversion algorithm to handle multiple fractures, investigate the uncertainties of the inversion results, and propose possible mitigations to the challenges raised by completion designs and field data acquisition through a multifracture synthetic case. Lastly, we also

*Part of this chapter is reprinted with permission from "Hydraulic-Fracture-Width Inversion Using Low-Frequency Distributed-Acoustic-Sensing Strain Data—Part I: Algorithm and Sensitivity Analysis" by Liu, Y., Jin, G., Wu, K., and Moridis, G., 2021. *SPE Journal*, 26 (01), 359-371, Copyright [2021] by Society of Petroleum Engineers, and "Hydraulic-Fracture-Width Inversion Using Low-Frequency Distributed-Acoustic-Sensing Strain Data—Part II: Extension for Multifracture and Field Application" by Liu, Y., Jin, G., Wu, K., and Moridis, G., 2021. *SPE Journal*, Preprint, Copyright [2021] by Society of Petroleum Engineers.

test the height sensitivity of the algorithm and discuss how to estimate fracture height and fracture length.

5.2 Inversion Algorithm Development for Single Fracture

5.2.1 Green-Function Matrix Construction

In the Cartesian coordinate system, the strain (ε) at a point (x, y, z) in the direction of the monitoring well, induced by a single fracture element located at $(0,0,0)$ with constant width *w*, can be expressed using a Green function as

$$G(x, y, z)w = \varepsilon(x, y, z), \tag{5.1}$$

where *G* is the Green function.

In a discretized system for numerical analysis, we assume there are N fracture elements and M sensing points along the fiber, as shown in Figure 5.1. At the j^{th} sensing point (x_{sj}, y_{sj}, z_{sj}), the strain component along the fiber induced by the i^{th} fracture element (x_{fi}, y_{fi}, z_{fi}) can be written as

$$\varepsilon_j^i(x_{sj}, y_{sj}, z_{sj}) = G(x_{sj} - x_{fi}, y_{sj} - y_{fi}, z_{sj} - z_{fi})w_i, \tag{5.2}$$

where ε_j^i denotes the strain component at the j^{th} sensing point induced by the i^{th} fracture element. Subscripts *i* and *j* are the fracture index and sensing-point index, respectively. Subscript *s* denotes sensing point, while subscript *f* denotes fracture. w_i is the width of fracture element *i*.

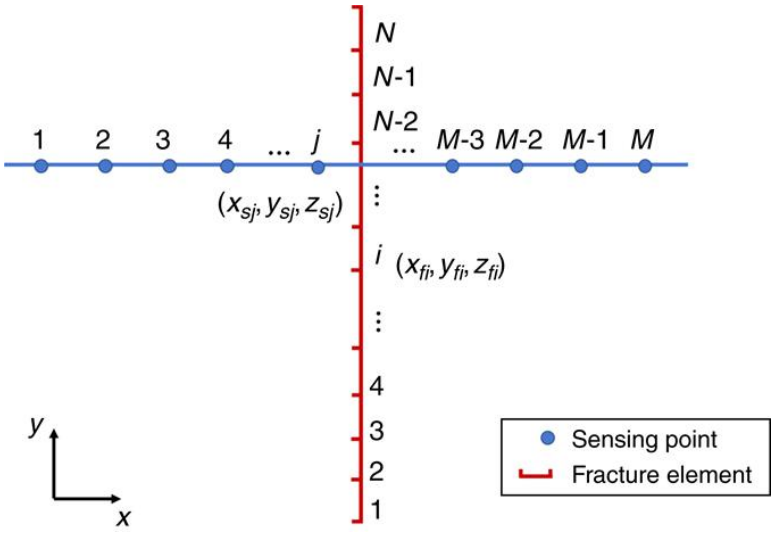

Figure 5.1 Conceptual illustration of relative positions of fracture elements and sensing points along the fiber (reprinted from Liu et al. 2021c).

Under the assumption of linear-elastic-rock deformation, the induced strain at a point $\left(x_{sj}, y_{sj}, z_{sj}\right)$ is the superposition of the individual contributions of the N fracture elements, which can be expressed as

$$\varepsilon_j\left(x_{sj}, y_{sj}, z_{sj}\right) = \sum_{i=1}^{N} G\left(x_{sj} - x_{fi}, y_{sj} - y_{fi}, z_{sj} - z_{fi}\right) w_i \,. \tag{5.3}$$

For all the M sensing points, we obtain a system of linear equations, written as

$$\begin{bmatrix} G_{11} & \cdots & G_{1i} & \cdots & G_{1N} \\ \vdots & \ddots & \vdots & \ddots & \vdots \\ G_{j1} & \cdots & G_{ji} & \cdots & G_{jN} \\ \vdots & \ddots & \vdots & \ddots & \vdots \\ G_{M1} & \cdots & G_{Mi} & \cdots & G_{MN} \end{bmatrix}_{M\times N} \begin{bmatrix} w_1 \\ \vdots \\ w_i \\ \vdots \\ w_N \end{bmatrix}_{N\times 1} = \begin{bmatrix} \varepsilon_1 \\ \vdots \\ \varepsilon_j \\ \vdots \\ \varepsilon_M \end{bmatrix}_{M\times 1} , \tag{5.4}$$

where $G_{ji} = G\left(x_{sj} - x_{fi}, y_{sj} - y_{fi}, z_{sj} - z_{fi}\right)$ represents the Green function associated with the i^{th} fracture element and j^{th} sensing point. For convenience, Eq. (5.4) can be written in a matrix-vector form as

$$\mathbf{Gw} = \boldsymbol{\varepsilon}, \tag{5.5}$$

where **G** denotes the Green-function matrix; **w** is the fracture-width vector, which consists of the unknown parameters; and $\boldsymbol{\varepsilon}$ is the strain vector that can be measured by LF-DAS.

Then, the key is to construct the **G** matrix. The physical forward model presented in Chapter 2 is used to build the Green-function matrix. Eq. (2.20) to Eq. (2.22) are the fracture-induced displacements as a function of displacement discontinuities. Here, the fracture width is equivalent to the normal displacement discontinuity (D_1) in a local coordinate system. As suggested by Eq. (2.26), LF-DAS measures the linearly scaled strain perturbation over a predefined gauge length along the fiber. Therefore, the strain at the j^{th} sensing point (ε_j) can be calculated using

$$\varepsilon_j = \frac{u_{j+\frac{L}{2}} - u_{j-\frac{L}{2}}}{L}, \tag{5.6}$$

where L is the gauge length and $j \pm \frac{L}{2}$ denotes locations that are $\frac{L}{2}$ from the sensing point j on both sides. It should be noted that the direction indices (i.e., x, y, z) are omitted for conciseness since the focus is always the strain in the direction of the fiber. Substituting displacements into Eq. (5.6) and replacing normal displacement discontinuity (Δu) by fracture width (w_i) leads to

$$\varepsilon_j = \frac{\sum_{i=1}^{N}\left[T^*\left(j+\frac{L}{2},i\right)-T^*\left(j-\frac{L}{2},i\right)\right]w_i}{L}, \tag{5.7}$$

where i denotes the fracture-element index and j denotes the sensing-point index. Comparing Eqs. (5.3), (5.4), and (5.7), we obtain that the component in the **G** matrix can be calculated using

$$G_{ji} = \frac{T^*\left(j+\frac{L}{2},i\right)-T^*\left(j-\frac{L}{2},i\right)}{L}, \tag{5.8}$$

where the analytical solutions for T^* can be found in Chapter 2.

We can tell that the components in the **G** matrix are dependent on the relative positions and direction of the sensing points and fracture elements. Therefore, it is convenient to calculate the values of the Green function over the spatial computational induced by a seed fracture element located at a reference point (e.g., the origin in Cartesian coordinates), then the desired **G** matrix can be obtained by shifting the seed Green function, based on the coordinates of sensing points and fractures. In particular, the spatial distribution of displacement in fiber-direction induced by a seed fracture element with unit width located at the origin can be calculated, denoted by $\tilde{\mathbf{T}}$. Then, the two influence-coefficient matrices that are needed to calculate the **G** matrix, as illustrated in Eq. (5.8), can be obtained by the following procedure:

Summary of **G** matrix calculation procedure.

Recall N is the number of fracture elements;
u denotes the coordinates of points along the monitoring well; each row represents one point.
v denotes the coordinates of fracture elements. each row represents one element.

---

1. **DO** i = 1, *N*:
2. $\mathbf{c} = \mathbf{u} - \mathbf{v}[i,:]$;
3. $\mathbf{T}^*[:,i] = f\left(\tilde{\mathbf{T}}, \mathbf{c}\right)$; f denotes the interpolation function.
4. **END DO**
5. Calculate **G** following Eq. (5.8)

5.2.2 Linear Least-Squares Method

The linear least-squares algorithm is commonly used to solve overdetermined or underdetermined problems by minimizing the *L-2* norm of the error vector **e**, which can be expressed as

$$err = \sum_i e_i^2 = \mathbf{e}^{\mathbf{T}}\mathbf{e}, \tag{5.9}$$

where $\mathbf{e} = \mathbf{Gw} - \boldsymbol{\varepsilon}$ is the data misfit in this study. Minimizing the "*err*" gives the solution, expressed as

$$\mathbf{w} = \left(\mathbf{G}^{\mathbf{T}}\mathbf{G}\right)^{-1}\mathbf{G}^{\mathbf{T}}\boldsymbol{\varepsilon}. \tag{5.10}$$

In real cases, the $\mathbf{G}^{\mathbf{T}}\mathbf{G}$ matrix in Eq. (5.10) is usually not full rank, which makes the linear system underdetermined. Under such circumstances, it is possible that there is no existing solution that fully satisfied all the equations in the system. When the matrix $\mathbf{G}^{\mathbf{T}}\mathbf{G}$ is ill-conditioned, regularization may be required to stabilize the inversion process. The regularization terms can be set up based on our general knowledge of the problem. This knowledge may not have to be accurate but could impose important constraints to stabilize the inversion. For the fracture-width inversion problem in this study, it can be assumed that the width variations along the fracture are smooth, which can be described

mathematically as the width difference between adjacent fracture elements is very small, written in a matrix-vector form as

$$\mathbf{Sw} = \mathbf{0}, \tag{5.11}$$

where **S** denotes the smoothness-regularization matrix and **w** is the width vector, which is expressed explicitly as

$$\mathbf{S} = \begin{bmatrix} 1 & -1 & 0 & 0 & \cdots & 0 & 0 \\ 0 & 1 & -1 & 0 & \cdots & 0 & 0 \\ 0 & 0 & 1 & -1 & \cdots & 0 & 0 \\ \vdots & \vdots & \vdots & \vdots & \ddots & \vdots & \vdots \\ 0 & 0 & 0 & 0 & \cdots & 1 & -1 \end{bmatrix}_{(N-1)\times N}, \ \mathbf{w} = \begin{bmatrix} w_1 \\ w_2 \\ w_3 \\ \vdots \\ w_n \end{bmatrix}_{N\times 1}. \tag{5.12}$$

Combining Eq. (5.5) and Eq. (5.11), the regularized linear system of equations can be written as

$$\begin{bmatrix} \mathbf{G} \\ \alpha\mathbf{S} \end{bmatrix} \mathbf{w} = \begin{bmatrix} \boldsymbol{\varepsilon} \\ \mathbf{0} \end{bmatrix}, \tag{5.13}$$

where α is a weighting coefficient that controls the smoothness of the fracture width.

In addition, it is common to assume that the fracture is symmetric about the perforation point. Mathematically, this constraint can be written as

$$\mathbf{Mw} = \mathbf{0}, \tag{5.14}$$

where **M** denotes the symmetry-regularization matrix, which is constructed as

$$\mathbf{M} = \begin{bmatrix} 1 & 0 & 0 & \cdots & \cdots & 0 & 0 & -1 \\ 0 & 1 & 0 & \cdots & \cdots & 0 & -1 & 0 \\ 0 & 0 & 1 & \cdots & \cdots & -1 & 0 & 0 \\ \vdots & \vdots & \vdots & \ddots & \ddots & \vdots & \vdots & \vdots \\ \cdots & 0 & 0 & 1 & -1 & 0 & 0 & \cdots \end{bmatrix}_{\frac{N}{2}\times N}. \tag{5.15}$$

Adding a symmetric constraint to Eq. (5.13), the regularized linear system can be expanded to

$$\begin{bmatrix} \mathbf{G} \\ \alpha\mathbf{S} \\ \beta\mathbf{M} \end{bmatrix} \mathbf{w} = \begin{bmatrix} \boldsymbol{\varepsilon} \\ \mathbf{0} \\ \mathbf{0} \end{bmatrix}, \tag{5.16}$$

where β is a weighting constant that controls the symmetry of the fracture.

To quantify the constraints that **G** imposes on fracture elements at different locations, we define a term called "data sensitivity", as

$$\chi_i = \sqrt{\sum_{j=1}^{M} G_{ji}^2}, i = 1, 2, \cdots, N, \tag{5.17}$$

and then χ is normalized into $\begin{bmatrix} 0 & 1 \end{bmatrix}$ following

$$\boldsymbol{\chi} = \frac{\boldsymbol{\chi} - \chi_{\min}}{\chi_{\max} - \chi_{\min}}, \tag{5.18}$$

where $\chi_{\max}$ and $\chi_{\min}$ represent the maximum and minimum values in the vector χ, respectively.

5.2.3 Markov chain Monte Carlo Method

Non-uniqueness is always an essential challenge in most inverse problems. To resolve this challenge, inversion algorithms have to be constrained by *a priori* information. MCMC methods are well suited for generating samples from the target distribution of the model data, allowing for inference of the unknown parameters as well as quantifying the associated uncertainties (Efendiev et al. 2005; Wang et al. 2017). To better understand LF-DAS strain data constraint and inverted model uncertainty, MCMC simulations are

conducted. The general framework of MCMC starts with a random initial model from a priori distribution, which is perturbed randomly until it finds a model that produces a smaller error. Then the model is updated with the current one and the process is repeated until the iteration number is achieved. After recording a final model, the algorithm starts a new initial model and repeats the aforementioned process until the maximum number of final models is reached. The statistics (e.g. mean and standard derivation) of the final models can straightforwardly illustrate the data sensitivity, which means, in this specific study, how many constraints can be imposed on width distribution along the fracture. The detailed algorithm in the inversion of LF-DAS strain data in this study reads as the following.

Summary of the MCMC algorithm.

1. **DO** *ichain* = 1, *max_chain*:
2. $\mathbf{w} = \mathbf{w}^0$; $\mathbf{w}^0$: randomly generated initial widths (model)
3. $err = \sum_i e_i^2 = \mathbf{e}^T\mathbf{e} = \left(\mathbf{Gw} - \boldsymbol{\varepsilon}\right)^T \left(\mathbf{Gw} - \boldsymbol{\varepsilon}\right)$ (Eq. (5.9))
4. **DO** *iter* = 1, *max_iteration*:
5. $\mathbf{w}^p = \mathbf{w} + \delta\mathbf{w}$; $\delta\mathbf{w}$: random perturbation
6. $err^p = \left(\mathbf{Gw}^p - \boldsymbol{\varepsilon}\right)^T \left(\mathbf{Gw}^p - \boldsymbol{\varepsilon}\right)$
7. **IF** $err^p < err$ **THEN**:
8. $\mathbf{w} = \mathbf{w}^p$
9. $err = err^p$
10. **END IF**
11. **END DO**
10. $\mathbf{W}[:, ichain] = \mathbf{w}$, matrix storing the final model of each *ichain* iteration.
11. $\mathbf{E}[ichain] = err$, vector storing the associated data error of each *ichain* iteration.
12. **END DO**
13. *index* = **E** < *tolerance*, find the models with errors less than the predefined *tolerance*.
14. $\mathbf{W} = \mathbf{W}[:, index]$

15. Calculate the statistics (i.e. mean and variance) of **W**.

5.3 Inversion Algorithm Performance for Single Fracture

In this section, the inversion algorithm performance is tested through a synthetic case. The synthetic data, including dynamic fracture geometries during fracture propagation and the corresponding fracture-induced strain field monitored along a horizontal monitoring well, are used to demonstrate the inversion algorithms. Fracture propagation is simulated using an in-house simulator developed by Wu (2014), which couples linear-elastic rock deformation with non-Newtonian fluid flow in fractures and the horizontal wellbore. The real-time fracture-induced strains along the monitoring well are calculated by the efficient geomechanical model presented in Chapter 2.

5.3.1 Synthetic Data Preparation

The relevant geomechanical and completion parameters for simulating fracture propagation are listed in Table 5.1. We assume the fracture height is constant, which is confined by the pay-zone thickness. Figure 5.2 shows fracture half-length evolution during fluid injection and fracture width profiles at various time steps. Figure 5.3 schematically illustrates the well configuration along with the fracture geometry at the end of fluid injection. A hydraulic fracture initiates at and propagates from the treatment well, and the fiber attached to the monitoring well records the strain perturbations induced by the propagating fracture. The spacing between these two parallel horizontal wells is 100 m.

The real-time strain field measured along the horizontal monitoring well during the fluid injection process is shown in Figure 5.4. The gauge length used in Figure 5.4 is

5 m. After fracture hit, the fiber section along the fracture path is extended indicated by the red band, while sections on both sides of the fracture are compressed forming the blue stress-shadow regions. In synthetic data, the width of the red extension zone is equal to the gauge length (Liu et al. 2020a). These time-serial strain data along the monitoring well in Figure 5.4 will serve as 'data' for the inversion algorithm.

Table 5.1 Relevant geomechanical and completion parameters for the fracture propagation model (adapted from Liu et al. 2021c).

Parameter	Unit	Value
Young's Modulus	GPa	21.4
Poisson's Ratio	-	0.26
Minimum Horizontal Stress	MPa	41.34
Maximum Horizontal Stress	MPa	45.74
Injection Rate	m^3/min	3.18
Injection Time	min	61
Fluid Viscosity	cp	5
Interval Thickness	m	21.3

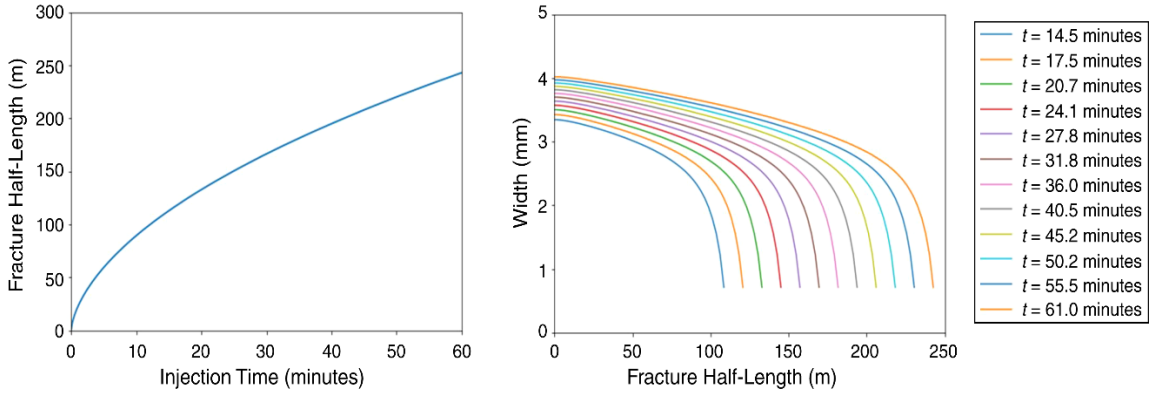

(a) (b)

Figure 5.2 (a) Fracture-half-length evolution and (b) fracture-width profiles at various timesteps (reprinted from Liu et al. 2021c).

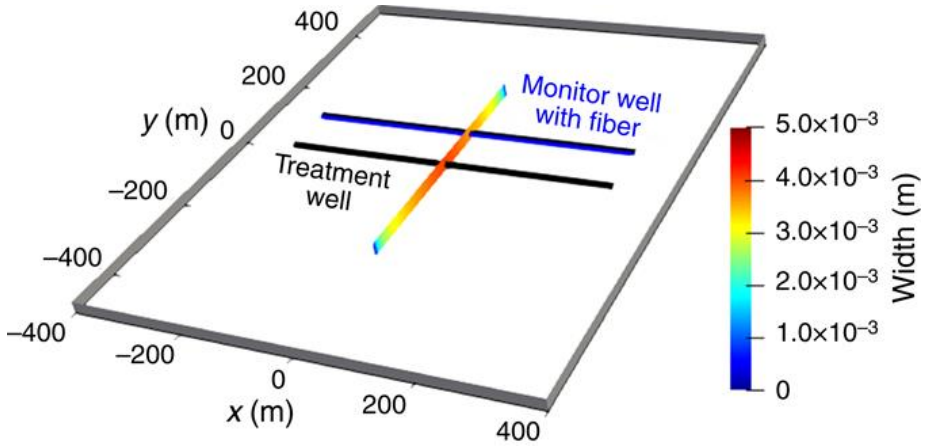

Figure 5.3 Schematic of the well pair consisting of a treatment well and a monitoring well, and the fracture geometry at the end of injection. The well spacing is 100 m (reprinted from Liu et al. 2021c).

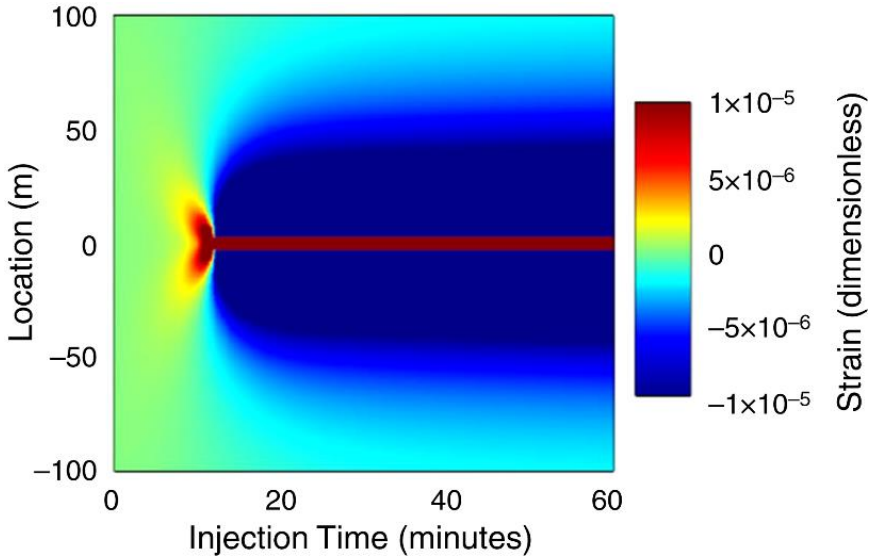

Figure 5.4 Waterfall plot of strain measured along the monitoring well during fracture propagation (reprinted from Liu et al. 2021c).

5.3.2 Forward-Model Verification

In this specific example, Figure 5.5(a) illustrates the spatial distribution of displacement in *x*-direction induced by a seed fracture element with unit width located at the origin, denoted by $\tilde{\mathbf{T}}$, and Figure 5.5(b) visualizes the values of the **G** matrix, calculated following the procedure outlined in Section 5.2.1. In this example shown in Figure 5.3, there are 201 sensing points along the monitoring well and 202 elements of the potential fracture.

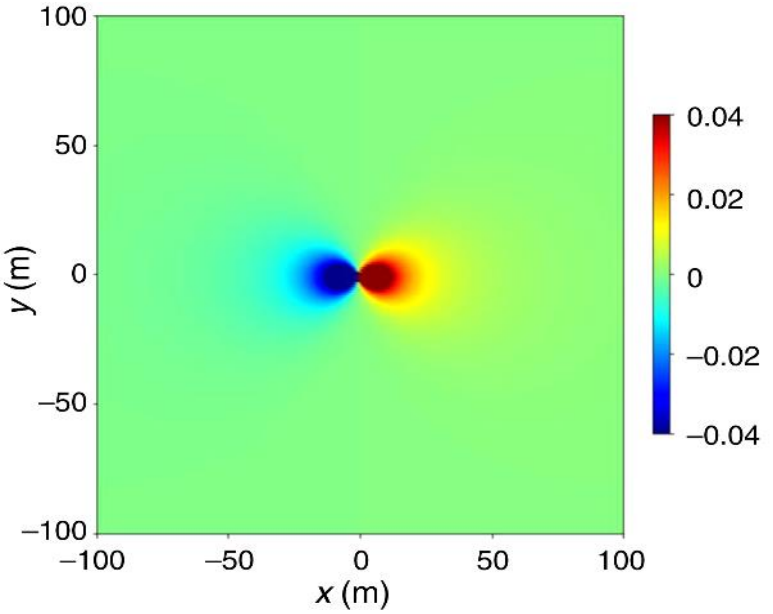

(a)

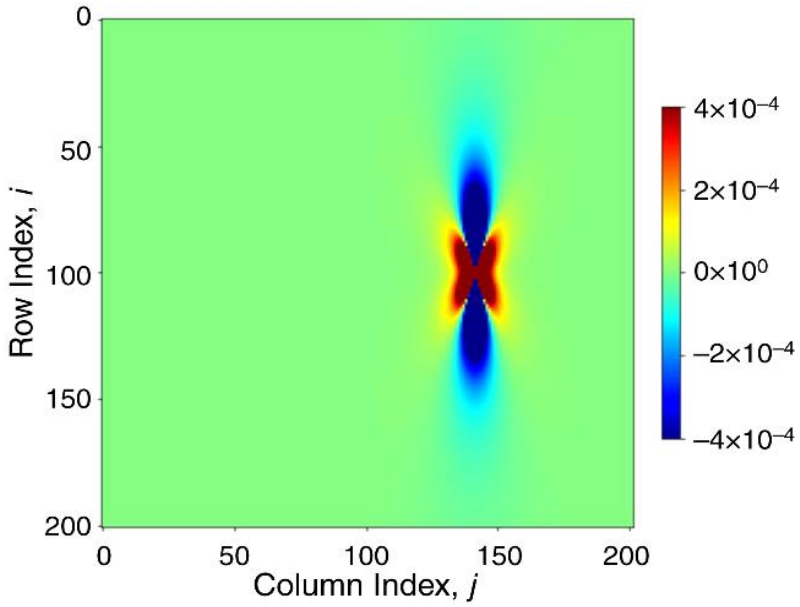

(b)

Figure 5.5 (a) Influence coefficients over the spatial domain induced by a seed-fracture element located at the origin; (b) example of Green-function matrix (reprinted from Liu et al. 2021c).

Taking the final fracture geometry at the end of injection in Figure 5.2 as an example, we compare the strain distribution along the monitoring well calculated by the proposed procedure (Section 5.2.1) against those directly obtained from the geomechanical model (i.e., strains at the last timestep in Figure 5.4). The good agreements shown in Figure 5.6 validate the presented forward model. Specifically, the implementation of constructing the **G** matrix is verified.

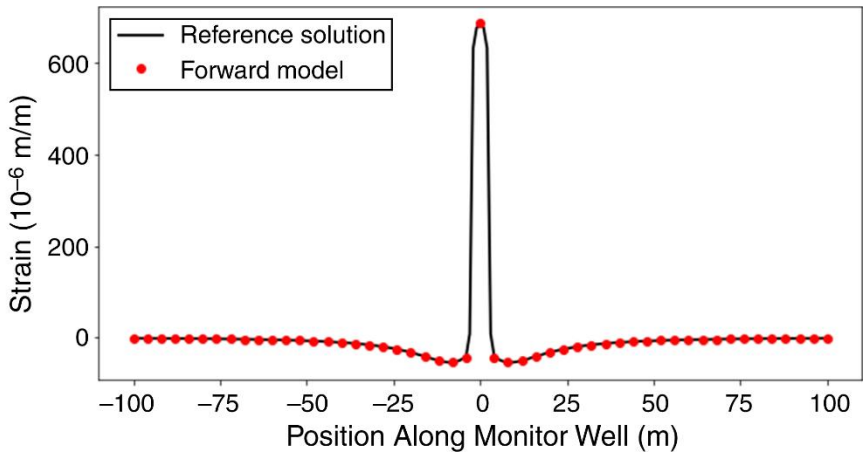

Figure 5.6 Comparison of strain distribution along the monitoring well calculated by the proposed forward model and the reference strain distribution obtained from the fracture model (Wu 2014; Liu et al. 2020d) (reprinted from Liu et al. 2021c).

5.3.3 Results of Linear Least-Squares Method

The fracture geometry and the corresponding strain data along the monitoring well at the end of the injection are used for analysis in this subsection. Without any regularization, Eq. (5.10) gives unstable and chaos inversion results, as shown in Figure

5.7. This is because the $\mathbf{G}^{\mathbf{T}}\mathbf{G}$ matrix is ill-conditioned, and its condition number is extremely large (approximately 5×10^{11}). In addition, it can be seen straightforwardly from Figure 5.5(b) that the values in several rows are nearly identical and close to zero, which makes the linear system underdetermined, resulting in unstable inversion results. Adding a smoothness constraint can help to stabilize the inversion, Figure 5.8 shows the comparisons of true width distribution along the fracture and inverted width distributions with three different smoothness weighting coefficients (i.e. inverting Eq. (5.13)), as well as the comparisons among the true strain distribution along the monitoring well and the calculated strain distributions using the inverted widths. Figure 5.8(b) indicates that all the three cases can induce almost the same strain field along the monitoring well as the synthetic true strain data. However, the inverted fracture width profiles cannot match the true width profile, as shown in Figure 5.8(a). The magnitude of α does not have a significant effect on the inversion results.

It is worth noticing that the inverted width is nearly equal to the true width at the fracture-hit location (i.e., 100 m away from the perforation), where the data sensitivity also shows the maximum value. The results indicate that the strain data measured by LF-DAS along the monitoring well has maximum constraints on fracture geometry at the fracture-hit location, and only with minimum smoothness constraint, the Green-function-based linear inversion algorithm could produce accurate estimation at the fracture-hit location.

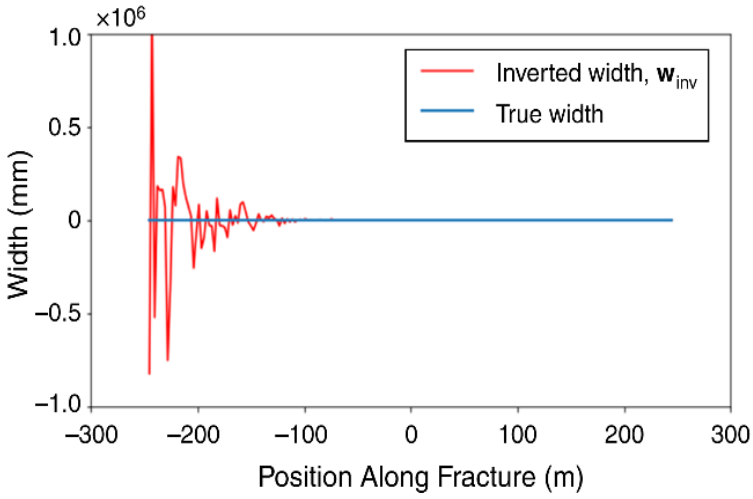

(a)

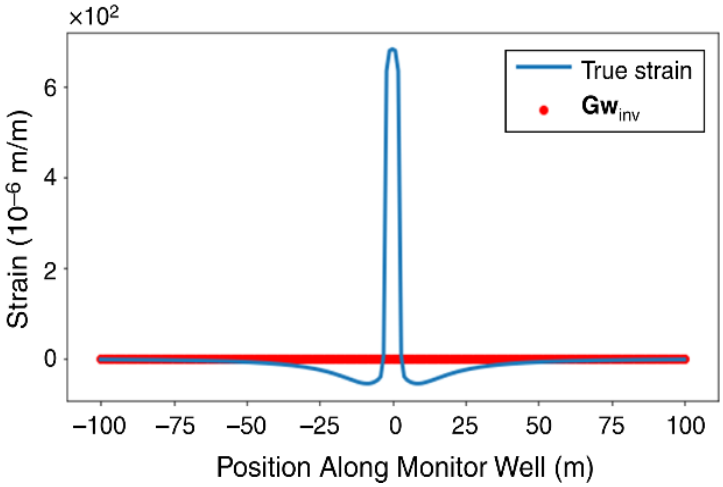

(b)

Figure 5.7 Comparisons of (a) true widths and inverted widths and (b) true strains and calculated strains using inverted widths for the least square method without regularization (reprinted from Liu et al. 2021c).

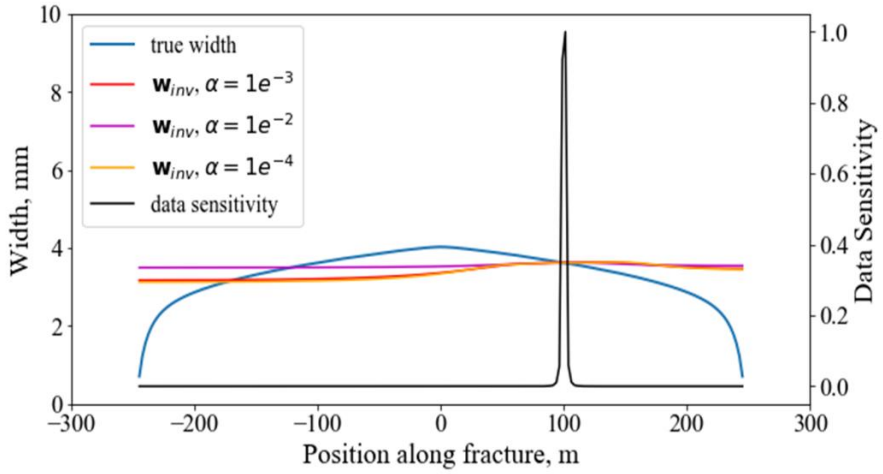

(a)

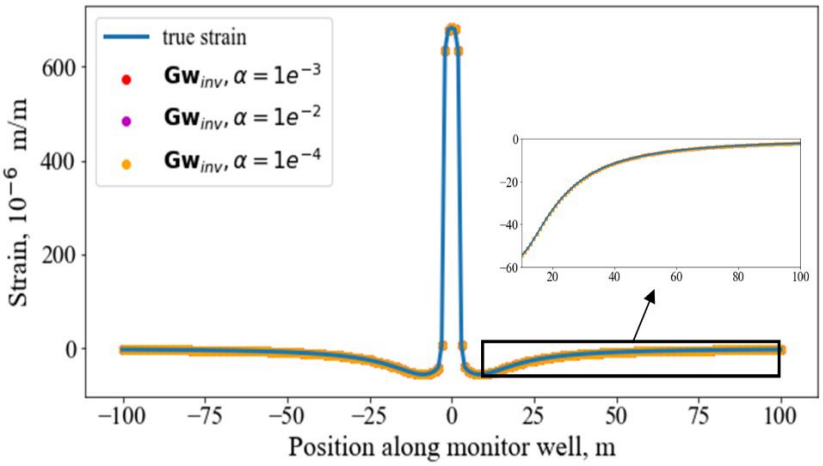

(b)

Figure 5.8 Comparisons of (a) true widths and inverted widths and (b) true strains and calculated strains using inverted widths for the smoothness-regularized least square method with three different weighting coefficients α (reprinted from Liu et al. 2021c).

To investigate if the inversion results can be improved by adding more constraints derived from some basic knowledge on fracture geometry, we add another regularization term to the linear system of equations assuming the fracture is symmetric about the perforation point (refer to Eq. (5.16)). Figure 5.9 presents the inverted width profiles and the corresponding calculated strain fields monitored along the monitoring well with three different weighting coefficients for symmetric regularization. As illustrated by Figure 5.9(b), the strain data of all the three cases can match the true strain data, but the inverted width profiles are sensitive to the weighting coefficient β. When β is small, the symmetry regularization term does not impose many constraints on the fracture width distribution, as illustrated by the yellow curve in Figure 5.9(a).

With an appropriate weighting coefficient, the inverted widths may show a good agreement with the true width, such as the realization represented by the purple curve in Figure 5.9(a). However, it is hardly possible to determine the proper weighting coefficient in real cases without having the reference solution. Nevertheless, the inverted width at the fracture-hit location is usually almost equal to the true width, no matter how the regularization terms are defined, as evidenced by both Figure 5.8(a) and Figure 5.9(a).

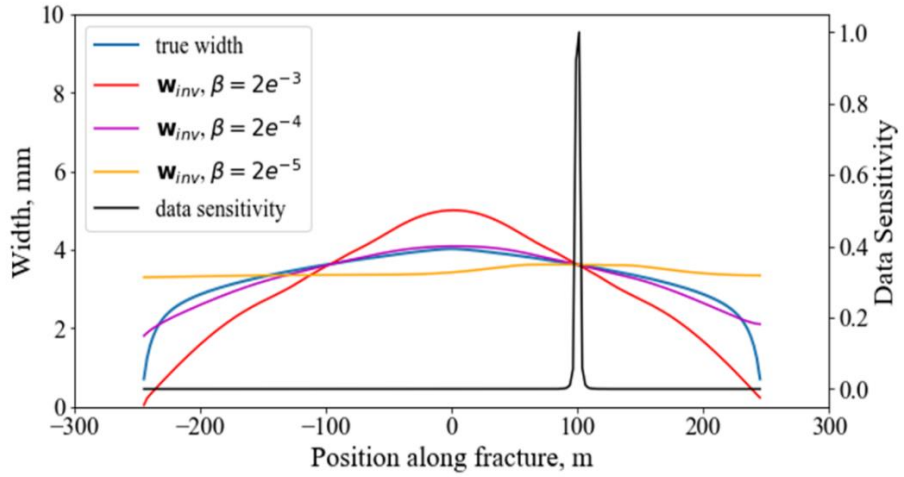

(a)

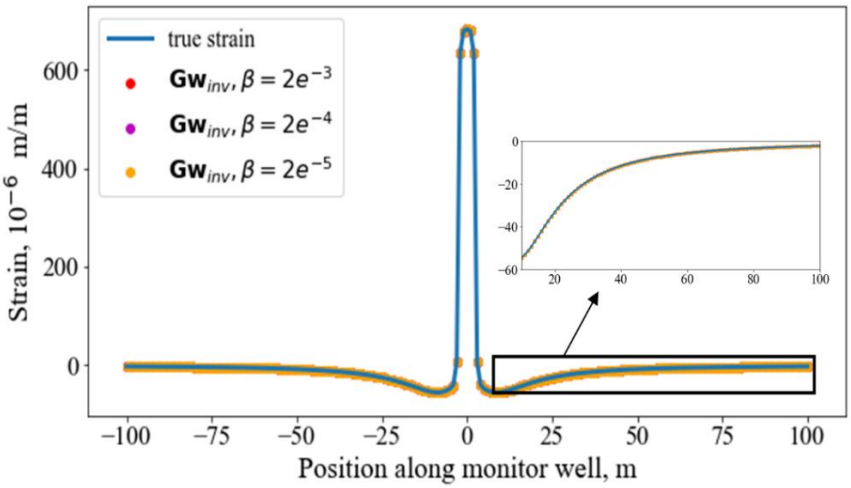

(b)

Figure 5.9 Comparisons of (a) true widths and inverted widths and (b) true strains and calculated strains using inverted widths for the smoothness- and symmetry-regularized least square method with three different weighting coefficients β; $\alpha = 1.0 \times 10^{-3}$ (reprinted from Liu et al. 2021c).

According to those analyses, it seems that the LF-DAS strain data measured along the offset monitoring well is dominantly influenced by the fracture segments near the monitoring well, where the data sensitivity, an inherent property of the **G** matrix, exhibits extremely high value. To testify this hypothesis and quantify the uncertainties associated with the constraints that the LF-DAS data can impose on hydraulic fracture geometry, we conduct MCMC simulations, the results of which are discussed in the following subsection.

5.3.4 Results of MCMC Simulation

Following the procedure presented in Section 5.2.3, we conduct a set of MCMC simulations using the same fracture geometry and strain data as those used in Section 5.3.3. To reduce the number of unknowns, we set several interpolation points where the widths are calculated, and then the width profile along the whole fracture is determined by linear interpolation. Expressed mathematically, the residual vector (**e**) in Eq. (5.9) becomes $\mathbf{e} = \mathbf{GLw}^* - \boldsymbol{\varepsilon}$, where $\mathbf{L}$ represents the interpolation operator and $\mathbf{w}^*$ contains the widths at the control points.

The initial widths are generated randomly within a range of 0 and 10 mm. The number of Markov chains (*max_chain*) is set to be 1000 and the iteration number (*max_iteration*) is 1000 within each Markov chain. With the relative mismatch threshold (*tolerance*) being 5%, the resultant width profile along the potential fracture path and the associated uncertainties of the initial models are presented in Figure 5.10, while those of the final models after MCMC simulations are presented in Figure 5.11 using the boxplots.

It should be noted that the slight oscillations in the box plots are due to the interpolation process. The variances at points between two control points are smaller than those right at the control points due to averaging effect of linear interpolation.

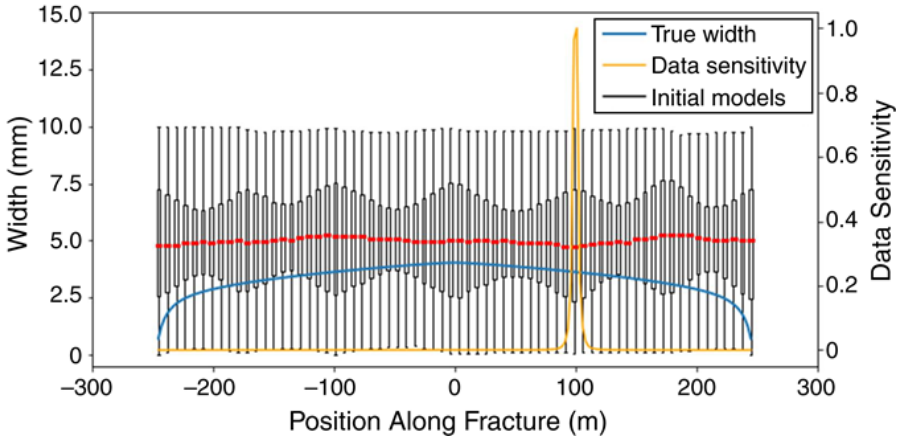

Figure 5.10 Boxplot of 1000 randomly generated initial fracture-width distributions. Red color indicates the median (reprinted from Liu et al. 2021c).

A comparison between Figure 5.10 and Figure 5.11(a) indicates that the variances in the near fracture-hit location region are decreased after MCMC simulation. It can also be clearly seen from Figure 5.11(a) that the distribution of the mean values of widths along the fracture cannot closely match the desired width distribution (i.e. the true widths), but the variances of widths keep decreasing as the locations get closer to the fracture-hit location. Right at the fracture-hit location, there is almost negligible variance (less than 0.03 mm) and the mean value (3.65 mm) is very close to the true fracture width (3.62 mm) with the relative error being less than 1%. Moreover, as shown in Figure 5.11(b), the variances of all the strain data at the sensing locations along the monitoring well are

vanished with the mean values being equal to the true strain data. The results confirm that LF-DAS strain data are insensitive to the fracture widths far away from the fracture-hit location. In other words, inversion of LF-DAS strain data results in accurate width estimation at the fracture-hit location, but it cannot constrain the fracture width away from the monitoring well location. However, it provides opportunities to characterize the whole fracture geometry with the accurate fracture width at the fracture-hit location and other constraints.

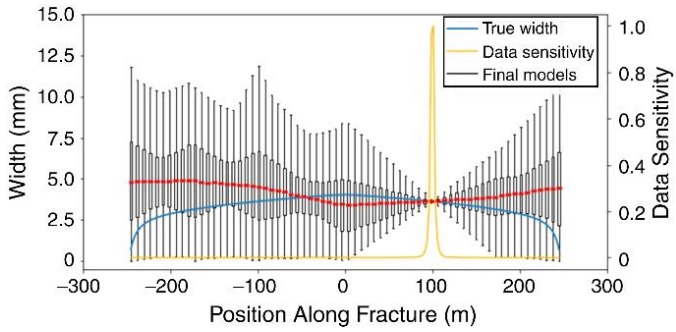

(a)

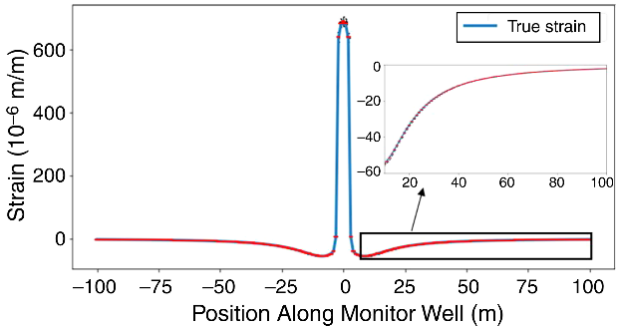

(b)

Figure 5.11 Boxplots of MCMC simulation models with relative mismatch error less than 5%: (a) inverted widths and associated statistics as well as data sensitivity; (b) calculated strains along the monitoring well. Red color indicates the median (reprinted from Liu et al. 2021c).

5.3.5 Impact of LF-DAS Measurement Bias

In the preceding analyses, the whole strain data set measured by a section of fiber along the monitoring well is used for inversion. However, in real cases, the LF-DAS data may not accurately represent the fracture-induced strain variation due to the decoupling between the fiber/cement and the formation rock, and the thermal effects (Jin and Roy 2017; Sherman et al. 2019; Liu et al. 2020a). When the fracture approaches the monitoring well, the sudden separation of rock may break the coupling between the formation and the cement/fiber, such that the LF-DAS cannot accurately capture the rock deformation at the fracture-hit location. Moreover, the fracturing fluid may induce temperature change that can also be detected by LF-DAS, leading to measurement bias near the fracture-hit locations.

To examine the effects of biased LF-DAS data on the inversion results, we modify the strains near the fracture-hit location to 25% of the true values. As shown in Figure 5.12, the final strain results of MCMC simulations cannot fit the true strain due to the existence of the nonphysical perturbations of the strain in the vicinity of the fracture-hit location. Correspondingly, the inverted width at the fracture-hit is also diverted from the true value, although the variances of widths keep decreasing as the locations get close to the fracture-hit location. In addition, we conduct another experiment with the strain data being the compressional strains 15 m away from the fracture-hit location. Figure 5.13 presents the MCMC inversion results, which show a very close match of the strain data and accurate inverted width at the fracture-hit location. Therefore, it is recommended to

exclude the measurements near the fracture-hit location. The range should be at least one-half of the gauge length on both sides of the fracture (Liu et al. 2020a, 2020c).

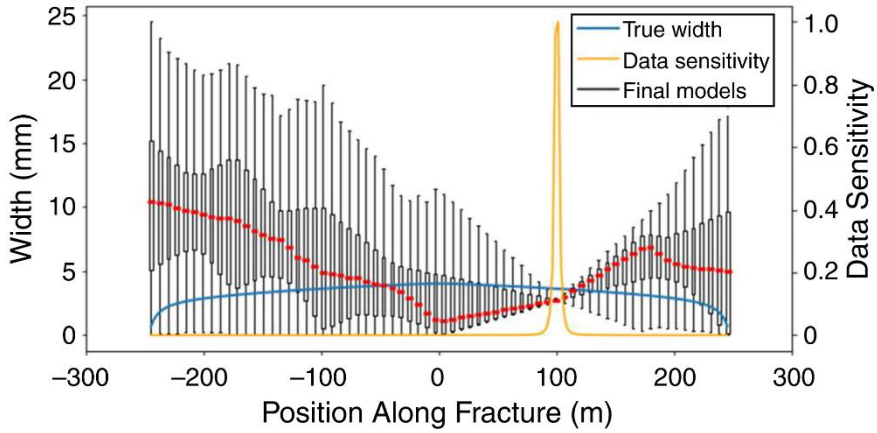

(a)

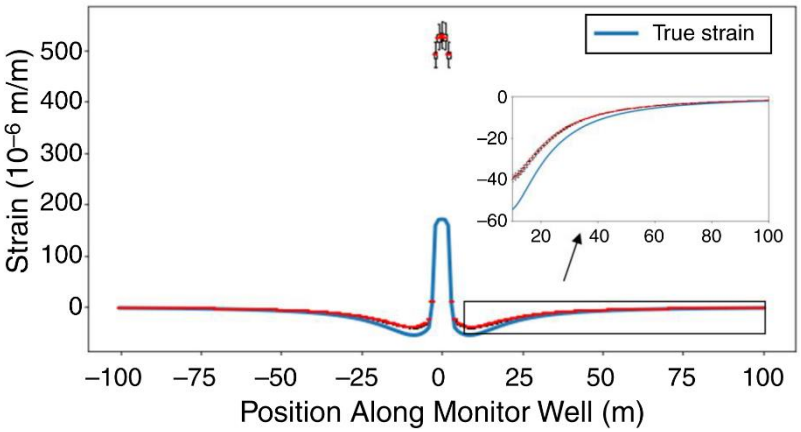

(b)

Figure 5.12 Boxplots of MCMC simulation models with biased strain data: (a) inverted widths and associated statistics as well as data sensitivity; (b) calculated strains along the monitoring well. Red color indicates the median (reprinted from Liu et al. 2021c).

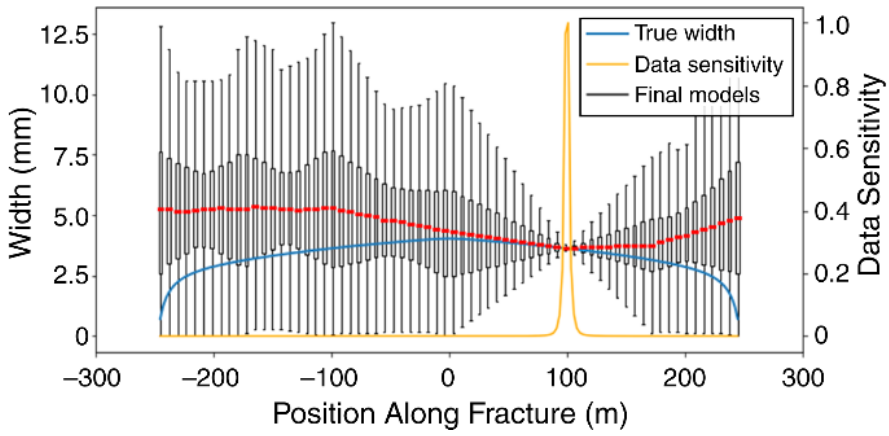

(a)

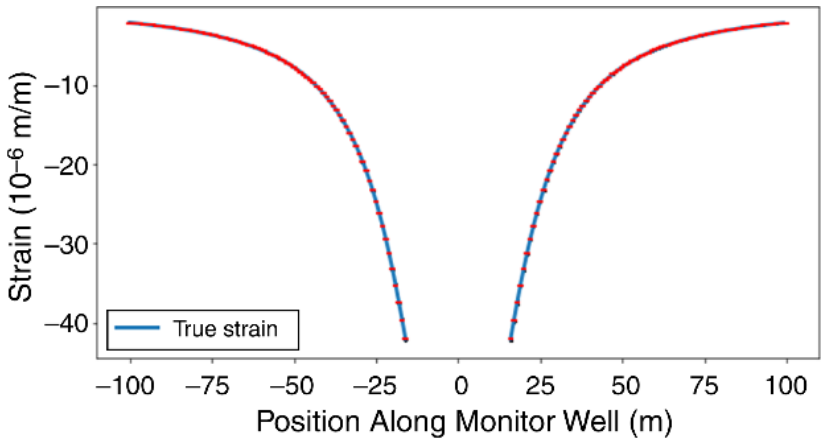

(b)

Figure 5.13 Boxplots of MCMC simulation models with compression strain data: (a) inverted widths and associated statistics as well as data sensitivity; (b) calculated strains along the monitoring well. Red color indicates the median (reprinted from Liu et al. 2021c).

5.3.6 Time-Dependent Fracture-Width Inversion

The preceding analyses indicate that LF-DAS strain data are only sensitive to the fracture widths near the fracture-hit location. To be specific, the inversion of LF-DAS

strain data can give an accurate estimation of fracture width at the fracture-hit location. In this section, we apply the presented Green-function-based algorithm to estimate the width evolution at the fracture-hit location after the fracture hits the monitoring well. The time steps are consistent with those shown in Figure 5.2(b). For MCMC inversion, the width at each time step is the mean of final models with data misfit less than 5%. Figure 5.14 compares the true widths and the inverted widths using both MCMC inversion and the least-square method with minimal smoothness constraint at multiple time steps. The good agreement validates the robustness and accuracy of the Green-function-based inversion algorithm.

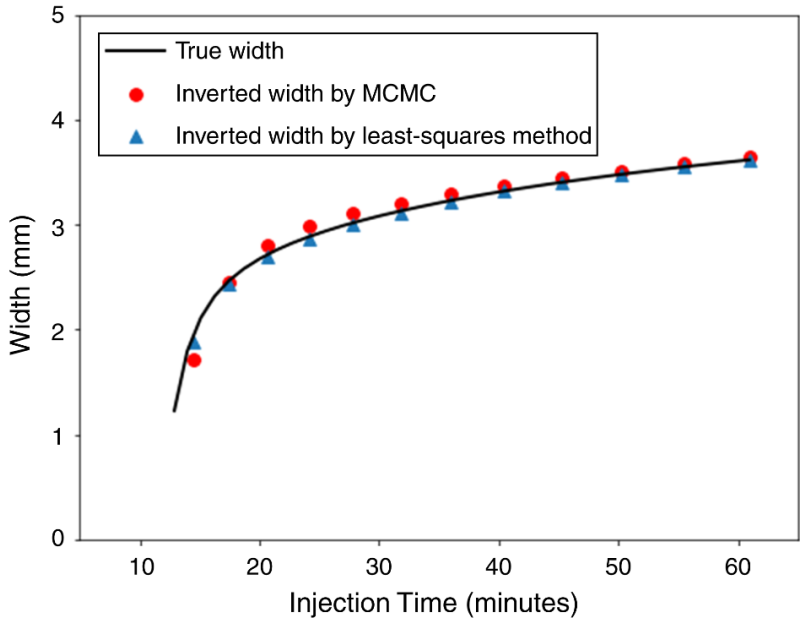

Figure 5.14 Comparison of true widths and inverted widths using both MCMC method and least-squares method at different timesteps after fracture hit (reprinted from Liu et al. 2021c).

In addition, since MCMC simulations confirm that widths of fracture sections away from the fracture-hit location have minimal impacts on the inversion results. We can assume a single width value for a fracture, representing the average width of fracture elements around the fracture-hit location (denoted as the "single-width" approach). In such a way, there is no matrix/vector multiplication, which could significantly reduce the computational cost. Specifically, the error vector **e** in Eq. (5.9) is reduced from $\mathbf{e} = \mathbf{G}\mathbf{w} - \boldsymbol{\varepsilon}$ to $\mathbf{e} = \mathbf{g}\bar{w} - \boldsymbol{\varepsilon}$, where **g** is a vector for which the components are the summation of each row in **G**, and $\bar{w}$ is the single-width variable that needs to be solved. Under the same Markov chains, Figure 5.15 compares the inversion results using various widths along the fracture and the "single-width" approach with the true width evolution as a function of injection time. Except for the early time after the fracture encounters the monitoring well, there are negligible differences between the widths obtained using a single width for the whole fracture and the true widths. The relative errors of the first three timesteps obtained by the "single-width" approach are about 22%, 12%, and 4%, respectively. The relatively larger errors in the first few timesteps are caused by the more dramatic width variations near the fracture tip. As illustrated by the fracture width profile when t = 14.5 min in Figure 5.2(b), the width decreases significantly with respect to fracture half-length at 100 m, leading to the average width is slightly lower than the true width right at 100 m (i.e. the fracture-hit location). Nevertheless, the computational cost-saving "single-width" approach still generates satisfactory inversion results at later times.

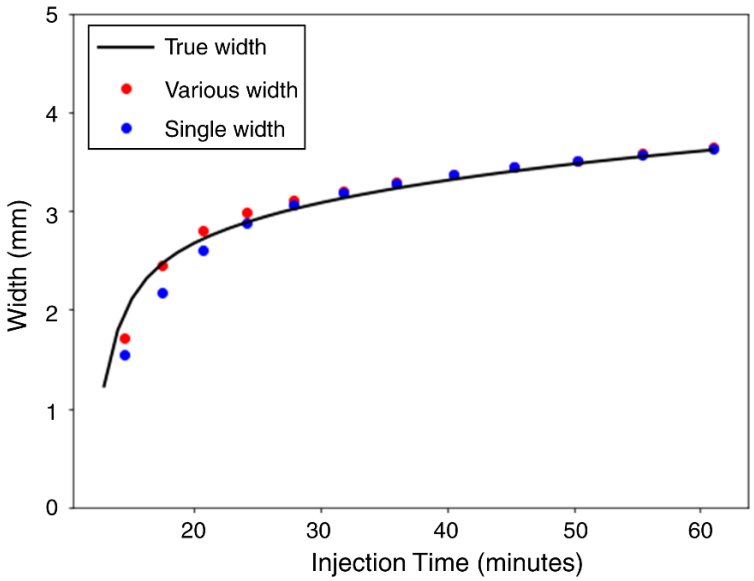

Figure 5.15 Comparison of true widths and inverted widths at different timesteps after fracture hit (reprinted from Liu et al. 2021c).

5.3.7 Height Sensitivity

In the proposed algorithm, the height of the seed fracture element, used for the construction of the Green-function matrix, is constant with a predefined value. However, the fracture height may change dynamically during fracture propagation, and the value is hardly known. To investigate the sensitivity of inversion results to the seed fracture element height, we construct another four single-fracture synthetic cases with different heights. The geomechanical and fluid properties are the same as those listed in Table 5.1. Some other parameters and resultant final fracture geometries are listed in Table 5.2. Figure 5.16 shows the fracture geometries of all four cases at the end of injection. The fracture is not discretized in Cases A through C, while it is discretized into 11 elements

along the fracture-height direction in Case D such that the fracture width is non-uniform along the height.

Table 5.2 Model parameters and fracture geometries of synthetic cases for height sensitivity analysis (adapted from Liu et al. 2021b).

Case ID	Case A	Case B	Case C	Case D
Leak-off Coefficient, $m/sec^{0.5}$	0.0002	0.00009	0.000025	0.00009
Fracture height, m	10	20	50	20
Fracture half-length, m	258.47	260.91	256.03	260.91
Element number in height direction	1	1	1	11

(a) (b) (c) (d)

Figure 5.16 Final fracture width distribution of (a): Case A, (b): Case B, (c): Case C, (d): Case D (reprinted from Liu et al. 2021b).

We set the seed fracture-element height to be 20 m for inversion. Figure 5.17 compares the inverted widths and true widths at the fracture-hit location as a function of injection time. The accurate width estimations for all cases indicate that the inversion algorithm is insensitive to fracture height. Specifically, when the true fracture height is different from the height of the seed element used for constructing the Green-function matrix, the algorithm still gives a close width estimation to the true value. This can be explained by the dominant sensitivity of LF-DAS strain data to the fracture segment near

the monitoring well, as demonstrated in Section 5.3.4. Since the fracture segments away from the monitoring well are loosely constrained, their inverted widths could be changed under different inversion conditions such as different heights of the seed element. However, the width at the fracture-hit location can be determined and match well the true value.

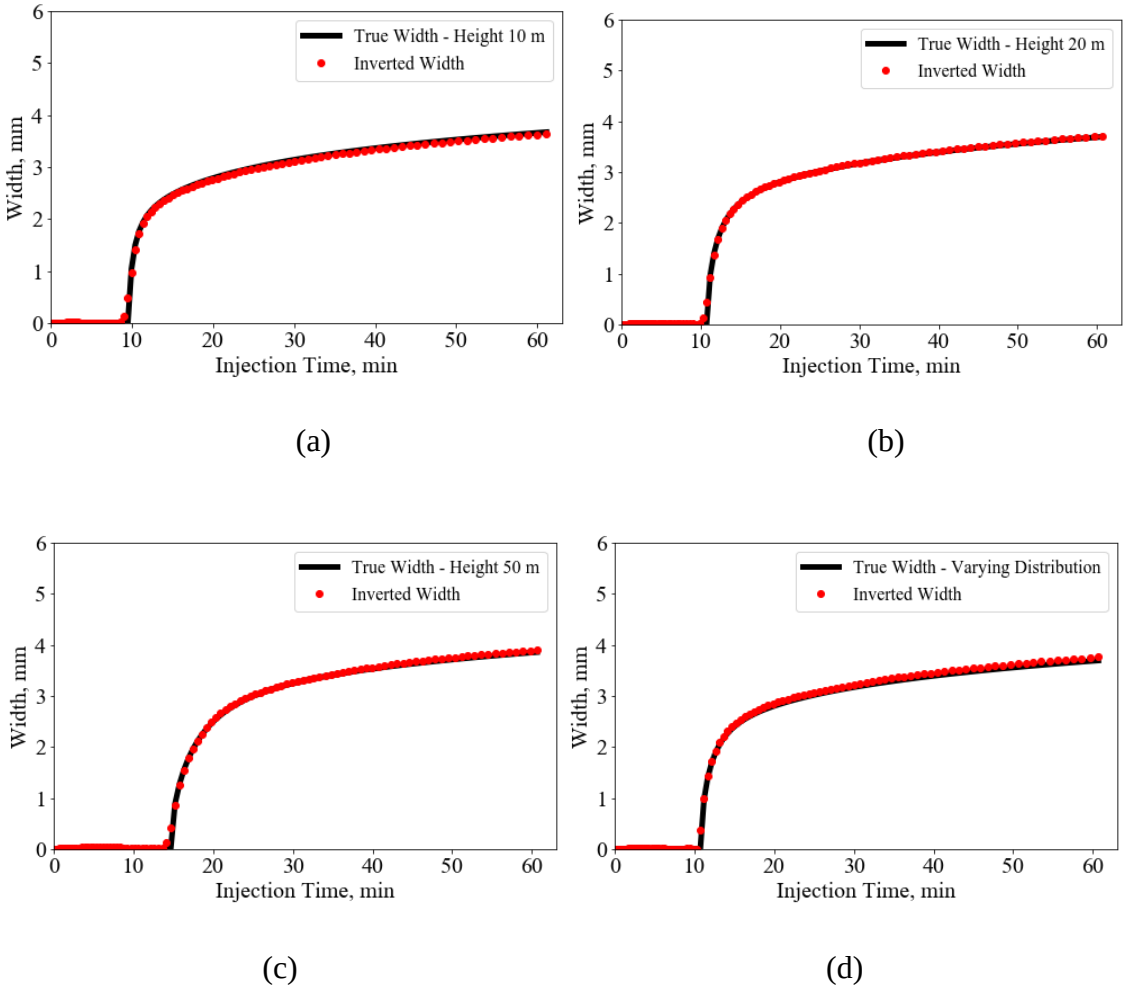

Figure 5.17 Comparison of inverted widths and true widths of (a): Case A, (b): Case B, (c): Case C, and (d): Case D (reprinted from Liu et al. 2021b).

5.3 Inversion Algorithm Development for Multiple Fractures

Because the multicluster plug-and-perf completion scheme is commonly adopted in recent hydraulic fracturing treatments, it is necessary to extend the inversion algorithm to be applicable for multifracture. Therefore, in this section, we present the extended algorithm, and test its robustness and accuracy through a multifracture synthetic case.

5.3.1 Green-Function Matrix Assembly

As shown in Figure 5.18, there are *M* sensing points along a monitoring well and *F* potential fractures, and each fracture is divided into *N* segments. As described in Section 5.2.1, the strain field at the *M* sensing points induced by fracture *f* can be expressed as

$$\mathbf{G}_f \mathbf{w}_f = \boldsymbol{\varepsilon}_f , \tag{5.19}$$

where $\mathbf{G}_f$ denotes the Green-function matrix associated with fracture *f*, $\mathbf{w}_f$ is the fracture width vector, and $\boldsymbol{\varepsilon}_f$ is the strain vector induced by fracture *f*, which are written as

$$\mathbf{G}_f = \begin{bmatrix} G_{1f_1} & \cdots & G_{1f_i} & \cdots & G_{1f_N} \\ \vdots & \ddots & \vdots & \ddots & \vdots \\ G_{jf_1} & \cdots & G_{jf_i} & \cdots & G_{jf_N} \\ \vdots & \ddots & \vdots & \ddots & \vdots \\ G_{Mf_1} & \cdots & G_{Mf_i} & \cdots & G_{Mf_N} \end{bmatrix}_{M\times N}, \ \mathbf{w}_f = \begin{bmatrix} w_{f_1} \\ \vdots \\ w_{f_i} \\ \vdots \\ w_{f_N} \end{bmatrix}_{N\times 1}, \ \boldsymbol{\varepsilon}_f = \begin{bmatrix} \varepsilon_{f_1} \\ \vdots \\ \varepsilon_{f_j} \\ \vdots \\ \varepsilon_{f_M} \end{bmatrix}_{M\times 1}, \tag{5.20}$$

where G_{jf_i} represents the Green function corresponding to the *i*th element of fracture *f* and the *j*th sensing point. For the whole system that contains *F* fractures, the LF-DAS measured strain field along the monitoring well is the superposition of the contributions

of each fracture element. Therefore, the resulting system of linear equations can be written as

$$\mathbf{G}\mathbf{w} = \boldsymbol{\varepsilon}, \tag{5.21}$$

and

$$\mathbf{G} = \begin{bmatrix} \mathbf{G}_1 & \mathbf{G}_2 & \cdots & \mathbf{G}_f & \cdots & \mathbf{G}_{F-1} & \mathbf{G}_F \end{bmatrix}, \tag{5.22}$$

$$\mathbf{w} = \begin{bmatrix} \mathbf{w}_1 \\ \mathbf{w}_2 \\ \vdots \\ \mathbf{w}_f \\ \vdots \\ \mathbf{w}_{F-1} \\ \mathbf{w}_F \end{bmatrix}, \tag{5.23}$$

$$\boldsymbol{\varepsilon} = \boldsymbol{\varepsilon}_1 + \boldsymbol{\varepsilon}_2 + \cdots + \boldsymbol{\varepsilon}_f + \cdots \boldsymbol{\varepsilon}_{F-1} + \boldsymbol{\varepsilon}_F, \tag{5.24}$$

where the subscripts indicate the fracture index. The detailed procedure to construct $\mathbf{G}_f$ was explained in Section 5.2.1.

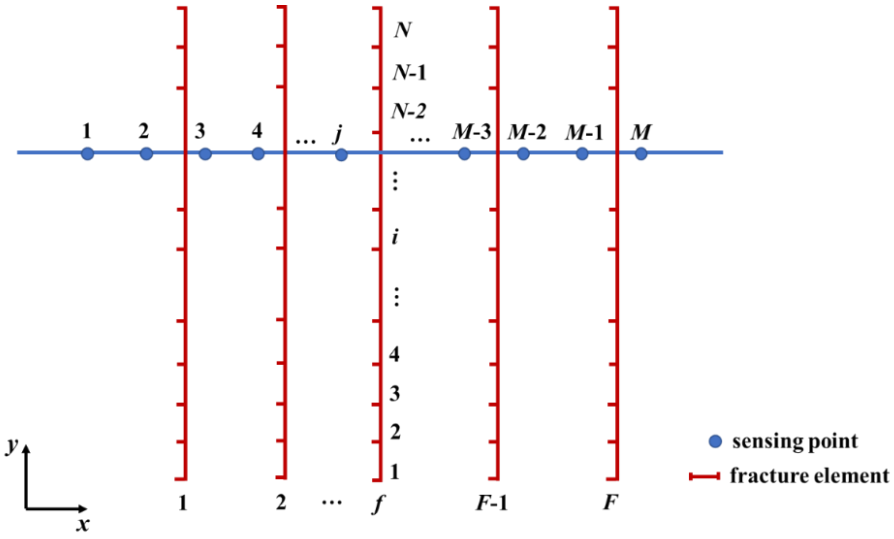

Figure 5.18 Conceptual illustration of multifracture and sensing locations along a monitoring well (reprinted from Liu et al. 2021b).

Based on the preceding analysis with a single fracture, we concluded that regularization is required to stabilize the inversion process. Smoothness constraint is sufficient for stable inversion and does not introduce significant error to the system. For a single fracture, this smoothness constraint can be written in a matrix-vector form as

$$\mathbf{S}_f \mathbf{w}_f = \mathbf{0}, \tag{5.25}$$

where $\mathbf{S}_f$ denotes the smoothness-regularization matrix corresponding to fracture *f*, the explicit expression is Eq. (5.12). For multiple fractures, such as *F* fractures in Figure 5.18, the smoothness constraint is written as

$$\mathbf{S}\mathbf{w} = \mathbf{0}, \tag{5.26}$$

and

$$\mathbf{S}=\begin{bmatrix} \mathbf{S}_1 & \mathbf{0} & \mathbf{0} & \mathbf{0} & \mathbf{0} & \mathbf{0} & \mathbf{0} \\ \mathbf{0} & \mathbf{S}_2 & \mathbf{0} & \mathbf{0} & \mathbf{0} & \mathbf{0} & \mathbf{0} \\ \mathbf{0} & \mathbf{0} & \ddots & \mathbf{0} & \mathbf{0} & \mathbf{0} & \mathbf{0} \\ \mathbf{0} & \mathbf{0} & \mathbf{0} & \mathbf{S}_f & \mathbf{0} & \mathbf{0} & \mathbf{0} \\ \mathbf{0} & \mathbf{0} & \mathbf{0} & \mathbf{0} & \ddots & \mathbf{0} & \mathbf{0} \\ \mathbf{0} & \mathbf{0} & \mathbf{0} & \mathbf{0} & \mathbf{0} & \mathbf{S}_{F-1} & \mathbf{0} \\ \mathbf{0} & \mathbf{0} & \mathbf{0} & \mathbf{0} & \mathbf{0} & \mathbf{0} & \mathbf{S}_F \end{bmatrix}, \tag{5.27}$$

and **w** is the same as Eq. (5.23). Combining Eqs. (5.21) and (5.26) leads to the regularized linear system of equations as

$$\begin{bmatrix} \mathbf{G} \\ \alpha\mathbf{S} \end{bmatrix}\mathbf{w}=\begin{bmatrix} \boldsymbol{\varepsilon} \\ \mathbf{0} \end{bmatrix}, \tag{5.28}$$

where α is a weighting coefficient that controls the smoothness of fracture-width variation.

5.3.2 Mitigation of Non-Unique Inversion Solutions

Because of the LF-DAS measurement bias near the fracture hits caused by the decoupling between the fiber and the formation rock, as well as the thermal perturbation (Jin and Roy 2017; Sherman et al. 2019), the strain data near the fracture-hit locations should be excluded (Liu et al. 2020b) from the inversion. However, this could introduce uncertainties in quantifying the contributions of each individual fracture to the strain field, which, in turn, generates biased inversion results. Although LF-DAS cannot accurately measure the fracture-induced strain variations near the fracture-hit locations, it captures the general dynamics of simultaneously propagating fractures in the same well under the same completion design. In other words, the LF-DAS measurement at each timestep is

consistent with the physical process of fracture opening or closing (e.g. positive strain rate indicates width increase, while negative strain rate indicates width decrease) at the monitoring well location. Therefore, we can add a time-dependent constraint to the inversion algorithm. For each fracture, the fracture width at the fracture-hit location can be written as

$$\beta w_{hit}^{t} = \beta\left(w_{hit}^{t-1} + \Delta w_{hit}^{t}\right), \tag{5.29}$$

where β is a weighting coefficient, subscript *hit* represents fracture-hit location, and superscript *t* is the timestep index. Δw_{hit}^{t} is approximated following the definition of strain rate ($\dot{\varepsilon}^{t} \times \Delta t \times L$), where $\dot{\varepsilon}^{t}$ is the strain rate measurement from LF-DAS at timestep *t*, Δt is the time interval, and *L* is the gauge length. Because the measurements at fracture-hit locations are not accurately representing the fracture-induced strain, the weighting coefficient β is used to reduce the contribution of data measured at the fracture-hit locations to the overall error.

Incorporating the time-dependent constraint into Eq. (5.28) results in the final linear equations, written as

$$\begin{bmatrix} \mathbf{G} \\ \alpha\mathbf{S} \\ \beta\mathbf{T} \end{bmatrix} \mathbf{w} = \begin{bmatrix} \boldsymbol{\varepsilon} \\ \mathbf{0} \\ \beta\mathbf{w'} \end{bmatrix}, \tag{5.30}$$

where the time-dependent constraint matrix **T** is constructed as

$$\mathbf{T}=\begin{bmatrix} \mathbf{T}_1 & \mathbf{0} & \mathbf{0} & \mathbf{0} & \mathbf{0} & \mathbf{0} & \mathbf{0} \\ \mathbf{0} & \mathbf{T}_2 & \mathbf{0} & \mathbf{0} & \mathbf{0} & \mathbf{0} & \mathbf{0} \\ \mathbf{0} & \mathbf{0} & \ddots & \mathbf{0} & \mathbf{0} & \mathbf{0} & \mathbf{0} \\ \mathbf{0} & \mathbf{0} & \mathbf{0} & \mathbf{T}_f & \mathbf{0} & \mathbf{0} & \mathbf{0} \\ \mathbf{0} & \mathbf{0} & \mathbf{0} & \mathbf{0} & \ddots & \mathbf{0} & \mathbf{0} \\ \mathbf{0} & \mathbf{0} & \mathbf{0} & \mathbf{0} & \mathbf{0} & \mathbf{T}_{F-1} & \mathbf{0} \\ \mathbf{0} & \mathbf{0} & \mathbf{0} & \mathbf{0} & \mathbf{0} & \mathbf{0} & \mathbf{T}_F \end{bmatrix}, \tag{5.31}$$

and the subarray $\mathbf{T}_f$ that corresponds to fracture f is a row vector, the components of which are zeros except for the one related to the fracture element at the fracture-hit location being unity. $\mathbf{w}'$ is a column vector, the size of which is the same as the fracture number F, expressed as

$$\mathbf{w}'=\begin{bmatrix} w_{1,hit}^{t-1}+\Delta w_{1,hit}^{t} \\ w_{2,hit}^{t-1}+\Delta w_{2,hit}^{t} \\ \vdots \\ w_{f,hit}^{t-1}+\Delta w_{f,hit}^{t} \\ \vdots \\ w_{F-1,hit}^{t-1}+\Delta w_{F-1,hit}^{t} \\ w_{F,hit}^{t-1}+\Delta w_{F,hit}^{t} \end{bmatrix}. \tag{5.32}$$

This mathematical treatment is derived based on the fact that the change of fracture width is continuous in time and LF-DAS measurements at fracture-hit locations are less reliable but capture the fracture propagation characteristics.

5.3.3 Fracture Height Estimation

Since the LF-DAS strain data is not sensitive to fracture sections away from the monitoring well, the inverted widths can be treated as the average widths for the fractures. We calculate the strain profiles along the monitoring well by the forward model, i.e., Eq.

(5.21) with different fracture heights. The absolute error should be decreasing as the height gets close to the true value. Thus, we can roughly estimate the fracture height by searching the minimum strain error, defined as

$$\delta = \frac{\sum_{m=1}^{M} \left| \varepsilon_m^c - \varepsilon_m \right|}{M}, \tag{5.33}$$

where ε_m^c is the calculated strain at sensing point m.

5.4 Inversion Algorithm Performance for Multiple Fractures

In this section, the accuracy of the extended algorithm to estimate fracture widths near the monitoring well during simultaneous multifracture propagation is tested through a synthetic case.

5.4.1 Synthetic Data Preparation

A fracture propagation model developed by Wu (2014) is used to simulate a four-cluster simultaneous fracture propagation process. The real-time fracture-induced strains along a parallel offset monitoring well are calculated by the efficient geomechanical model presented in Chapter 2. Table 5.3 lists the relevant fluid, geomechanical, and completion parameters for the synthetic case.

Table 5.3 Relevant geomechanical and completion parameters for the fracture propagation model (adapted from Liu et al. 2021b).

Parameter	Unit	Value
Young's Modulus	GPa	21.4
Poisson's Ratio	-	0.26
Minimum Horizontal Stress	MPa	45
Maximum Horizontal Stress	MPa	65
Injection Rate	m^3/min	12.72
Injection Time	min	60
Fluid Viscosity	cp	5
Interval Thickness	m	20

Figure 5.19(a) shows the fracture half-length evolution during fluid injection, while the final fracture geometries together with the well configuration are presented in Figure 5.19(b). Hydraulic fractures initiate at and propagate from the treatment well, and the fiber (labeled in blue) installed in the monitoring well records the strain field induced by the propagating fractures. The well spacing is 150 m. Because of fracture interactions (i.e., stress shadow), the inner two fractures are slightly shorter than the outer two fractures. Figure 5.20 illustrates the fracture width profiles at various timesteps during the fluid-injection phase. The real-time strains measured along the monitoring well are shown in Figure 5.21. The gauge length used in this synthetic case is 5 m. These spatial-temporal strains in Figure 5.21 will serve as the "data" for the inversion algorithm.

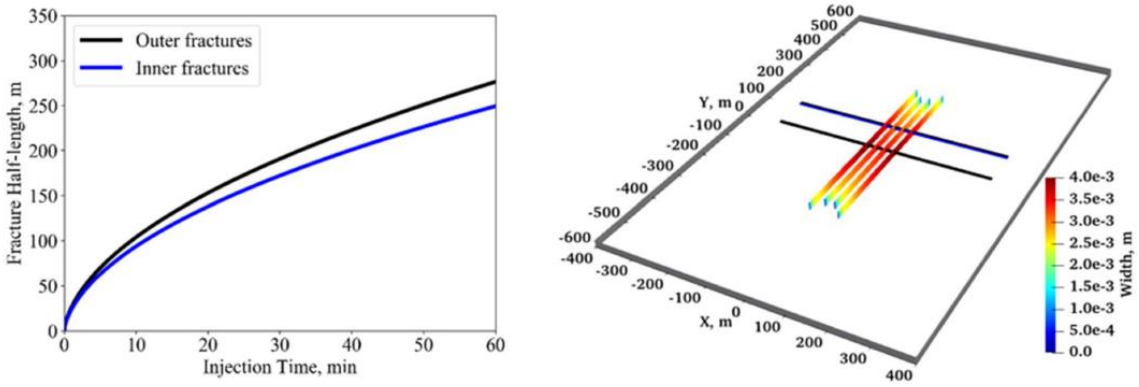

(a) (b)

Figure 5.19 (a) Fracture half-length as a function of injection time; (b) Final fracture geometries and well configuration (reprinted from Liu et al. 2021b).

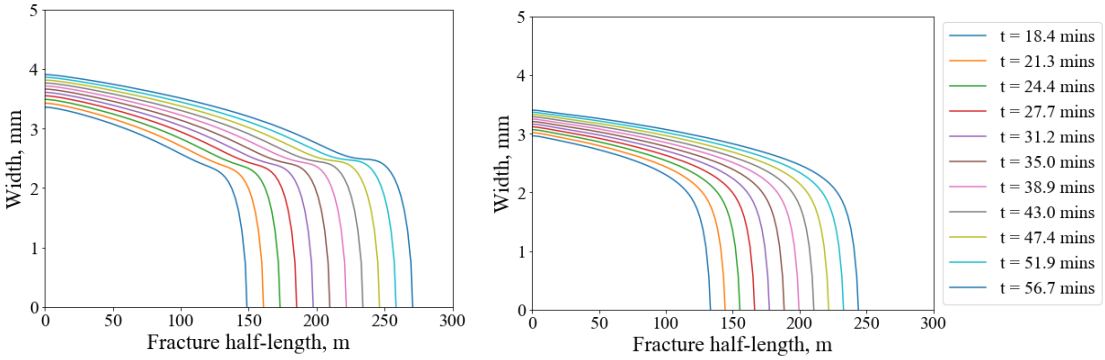

(a) (b)

Figure 5.20 Fracture width profiles of (a) outer fractures and (b) inner fractures at various timesteps (reprinted from Liu et al. 2021b).

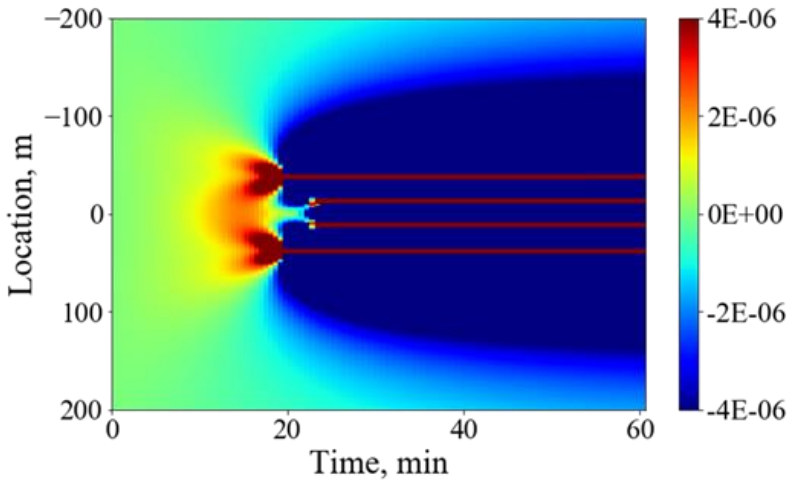

Figure 5.21 Waterfall plot of strain measured along the monitoring well during the fluid-injection process (reprinted from Liu et al. 2021b).

5.4.2 Multifracture Width-Inversion Results

Detailed analyses on the LF-DAS data sensitivity were conducted in Section 5.2 and the conclusion was that inversion of LF-DAS strain data gives accurate fracture width estimation near the monitoring well, whereas the geometries of fracture sections away from the monitoring well cannot be directly obtained without additional assumptions or constraints. Therefore, we focus on the time-dependent width estimation near the monitoring well in this study.

In the ideal condition, the strains along the entire fiber length can be used as the data. When the model is stabilized only by the smoothness constraint (Eq. (5.28)), Figure 5.22(a) shows the summation of the widths near the monitoring well of all four fractures as a function of injection time, whereas Figure 5.22(b) shows the width evolution of individual fractures during the fluid-injection period. The inversion results show good

agreements with the true values in both presentations, illustrating the accuracy of the proposed inverse algorithm. Correspondingly, the strains along the monitoring well calculated using the inverted widths are shown in Figure 5.23, which are almost identical to the true strain data shown in Figure 5.21. Figure 5.24 compares the calculated strains and true strains along the monitoring well at two specific times to quantitatively illustrate the good fitting.

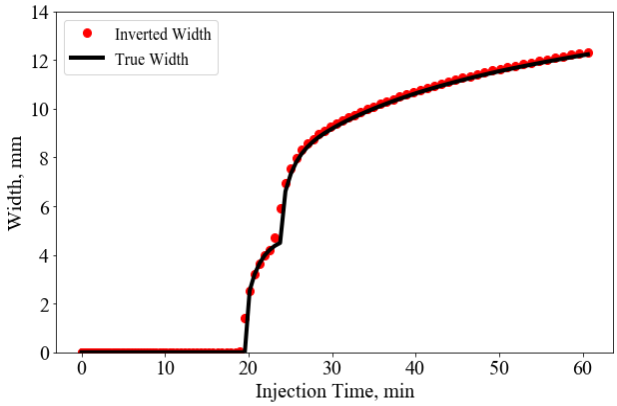

(a)

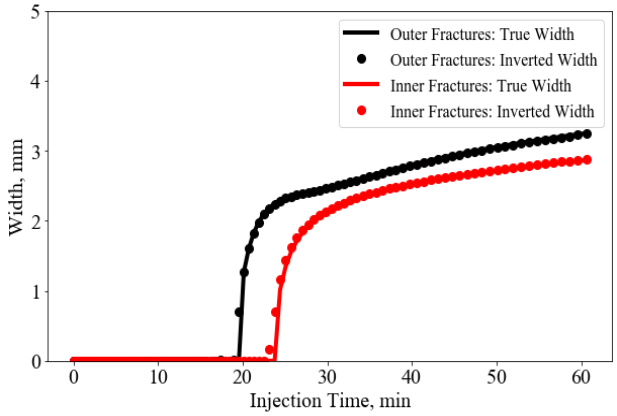

(b)

Figure 5.22 Evolution of (a) width summation of all fractures and (b) width of each individual fracture of the synthetic case with all the strain data (reprinted from Liu et al. 2021b).

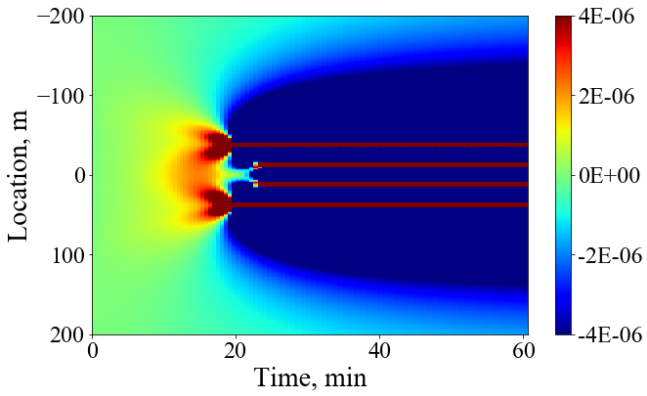

Figure 5.23 Waterfall plot of strain data calculated using the inverted widths during the fluid-injection process (reprinted from Liu et al. 2021b).

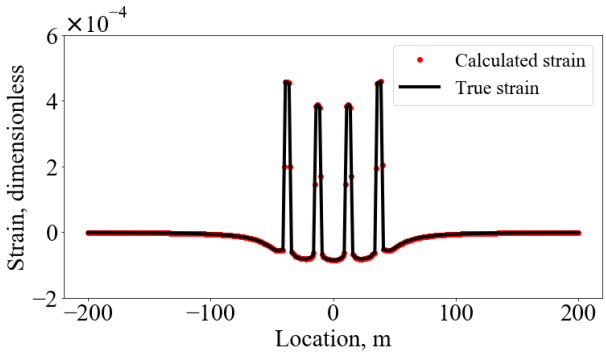

(a)

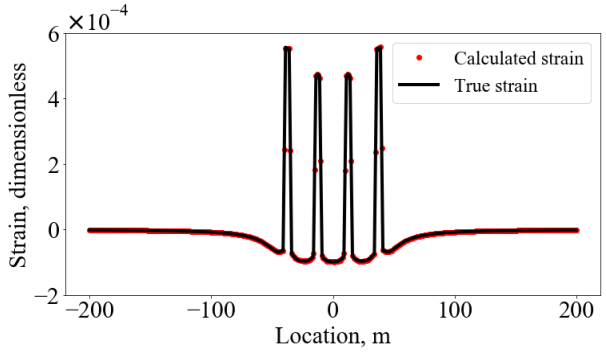

(b)

Figure 5.24 Comparison between calculated strain and true strain along the monitoring well at two different times. (a): 31.2 min; (b): 50.2 min (reprinted from Liu et al. 2021b).

This analysis indicates that the inversion algorithm is applicable for multifracture without additional treatments such as the time-dependent constraints at the fracture-hit locations (Eq. (5.30)) when the entire strain data set is available. However, the LF-DAS measurements near the fracture-hit locations are usually biased due to the decoupling between fiber and formation rock or the thermal effects (Jin and Roy 2017b; Sherman et al. 2019), which could lead to unreliable inversion results (Liu et al. 2020a). In addition, there may be no available data at all between adjacent fracture hits when the cluster spacing is close to the gauge length (Liu et al. 2020d). To test the model performance with limited strain data, in addition to excluding the data within one gauge length on both sides of each fracture, we removed the strain data between the outer fractures and the inner fractures representing the worst scenario (i.e., no available data between adjacent fractures), as shown in Figure 5.25.

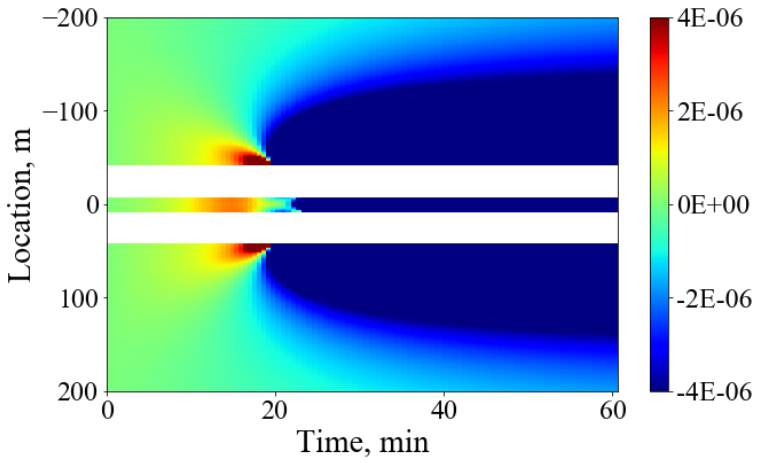

Figure 5.25 Waterfall plot of limited strain data along the monitoring well during the injection period (reprinted from Liu et al. 2021b).

Figure 5.26 shows the evolution of both the summarized width of all fractures and the width of each individual fracture. As illustrated by Figure 5.26(a), the summations of the inverted widths at different injection time are consistent with the true values. However, the width evolution of each individual fracture shows obvious deviations from the true widths, as shown in Figure 5.26(b). This is because an incomplete dataset leads to nonunique inversion solutions (Bernauer et al. 2014). In this example, due to the missing of strain data at some intervals, especially the extensions near the fracture-hit locations, the inverted widths of individual fractures show large errors.

To resolve the aforementioned issue that could be commonly encountered in field cases with multifracture, we add the time-dependent constraint to the inversion algorithm (Eq. (5.30)), and the inverted width profiles are shown in Figure 5.27. In addition to the good agreements between the summations of inverted widths and true widths (Figure 5.27(a)), the widths of each individual fracture show a close match to the true values with negligible differences. In Figure 5.28, the corresponding calculated strains at two specific times are compared with the true limited strain data. The results indicate that the inversion algorithm under the time-dependent constraints is robust for multifracture and the width profiles of individual fractures can be distinguished even when the strain data are limited.

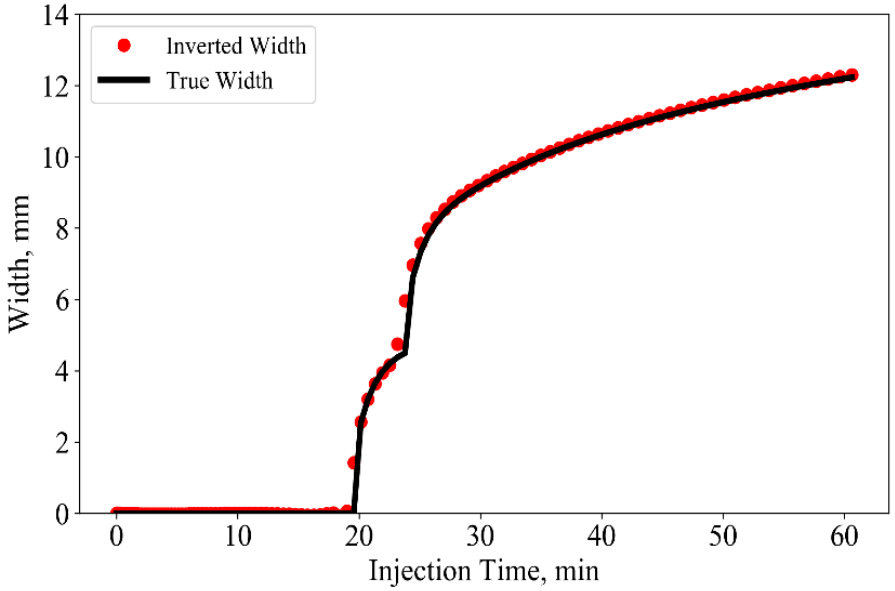

(a)

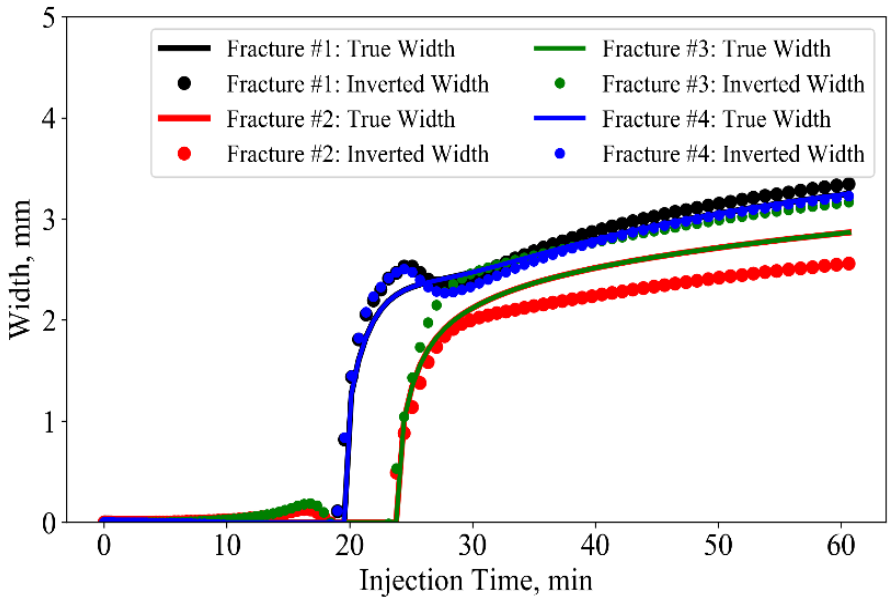

(b)

Figure 5.26 Evolution of (a) width summation of all fractures and (b) width of each individual fracture of the synthetic case with limited strain data (reprinted from Liu et al. 2021b).

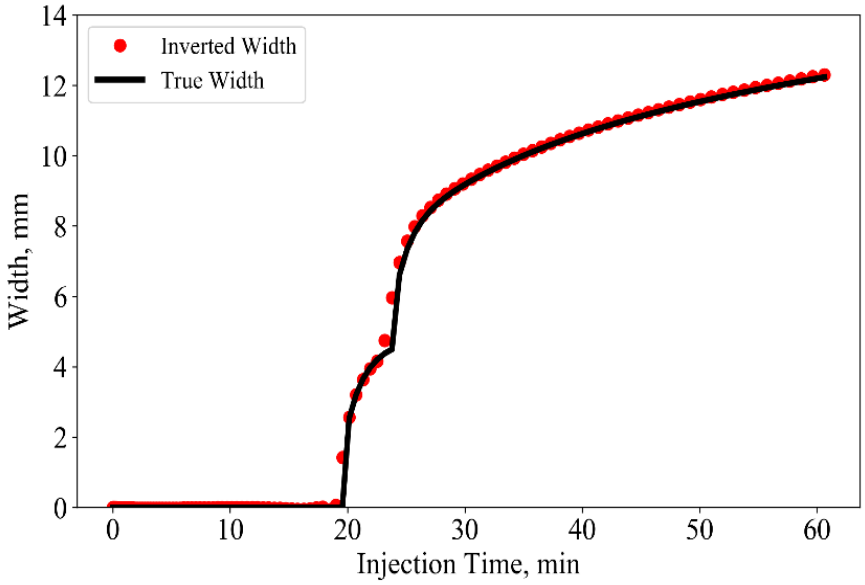

(a)

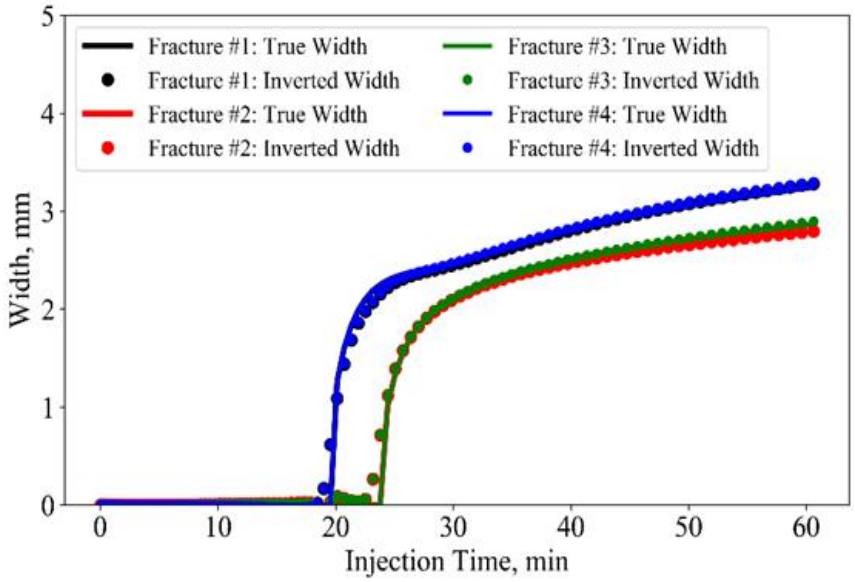

(b)

Figure 5.27 Evolution of (a) width summation of all fractures and (b) width of each individual fracture of the synthetic case under the time-dependent constraint (reprinted from Liu et al. 2021b).

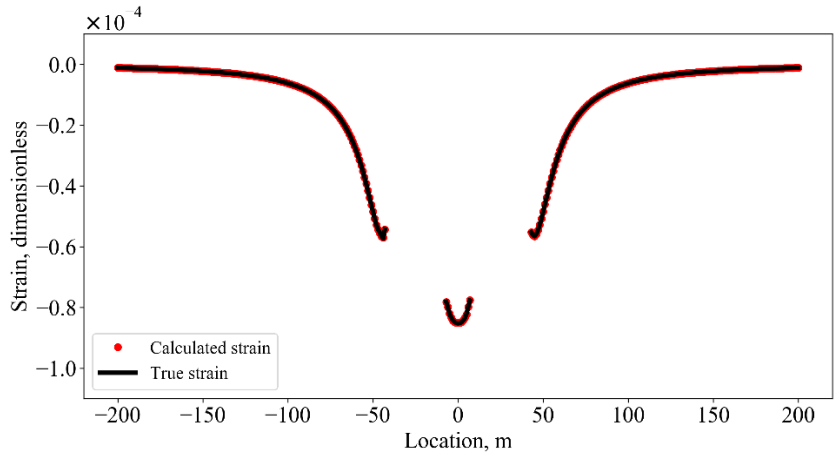

(a)

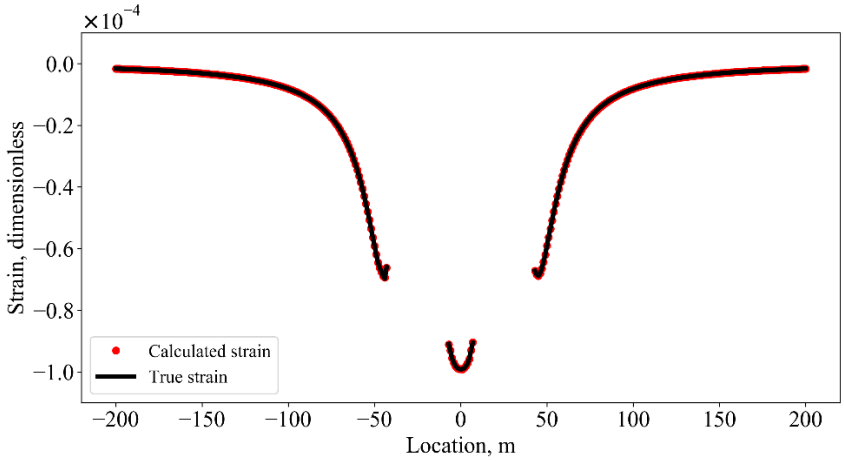

(b)

Figure 5.28 Comparison between calculated strain under the time-dependent constraint and true strain along the monitoring well at two specific times: (a) 31.2 minutes; (b) 50.2 minutes (reprinted from Liu et al. 2021b).

5.4.3 Height Estimation

After we obtain the fracture widths at the fracture-hit locations, we assume they represent the average width near the monitoring well. We calculate the strain profiles using various heights with a strong smooth weight and the error between the calculated strain and true strain should be minimum when the height is close to the true value. As shown in Figure 5.29(a), the strain profile along the monitoring well calculated with 20 m fracture height (i.e., true value) matches best with the true strains. Correspondingly, the average absolute strain error is lowest when fracture height is equal to 20 m (Figure 5.29(b)). In this quick assessment, we assume the heights of all the fractures are the same.

Moreover, the fracture length evolution may be evaluated by the equation proposed by Shapiro et al. (1997, 2002), written as

$$L = \sqrt{4\pi Dt}\ , \tag{5.34}$$

where L is equivalent to the fracture half-length, t is the treatment time. D is a scalar called hydraulic diffusivity, which can be determined by the offset distance between the treatment well and the monitoring well in LF-DAS and the fracture-hit time. Once the hydraulic diffusivity is determined, the fracture length evolution can be calculated. However, it should be noted that this equation is derived for the seismic triggering front in an effective isotropic homogeneous poroelastic medium. Therefore, the result predicted by Eq. (5.34) maybe not accurate enough. In addition, fracture length may be constrained under strong assumptions on fracture shape coupled with material balance equation or by other fracture diagnostic techniques such as microseismicity (Shapiro et al. 2002, 2006), which is not the focus of this dissertation. The contribution of this research is to

quantitatively characterize fracture width and height by the inversion of LF-DAS strain data without introducing any strong assumptions.

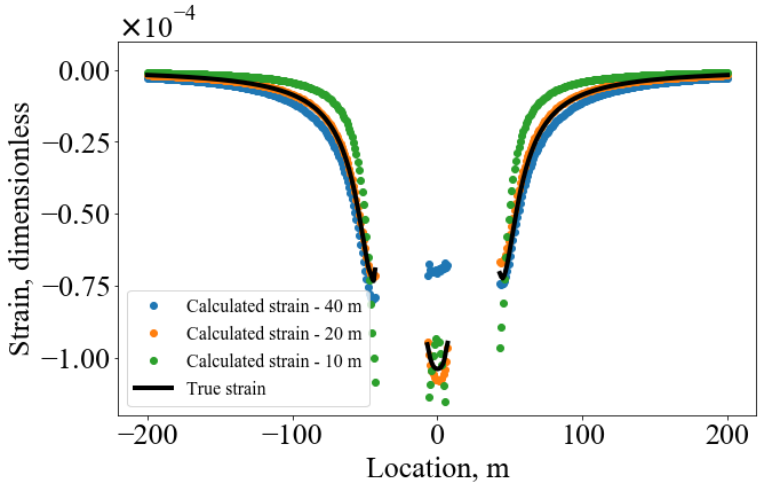

(a)

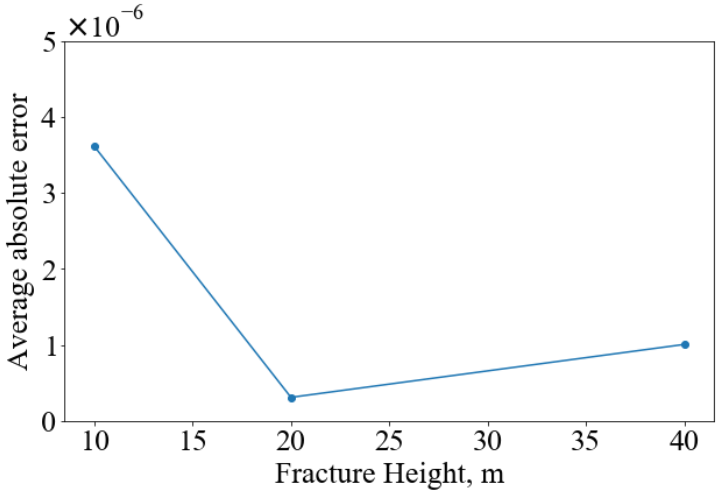

(b)

Figure 5.29 (a) Comparisons among calculated strains using different fracture heights and the true strain data along the monitoring well; (b) average absolute errors of different fracture heights (reprinted from Liu et al. 2021b).

5.5 Summary

In this chapter, we presented a Green-function-based algorithm for the inversion of LF-DAS strain data. The stability and accuracy of the inversion algorithm for fracture-width estimation were tested firstly through a single-fracture synthetic case. The linear least-squares method with regularization can be used to solve the linear system of equations. MCMC simulations were conducted to quantify the uncertainties associated with the unknown parameters, which confirmed that the LF-DAS data are only sensitive to the fracture segments near the monitoring well. The effects of LF-DAS measurement bias around the fracture hits and height sensitivity were examined as well.

Then, we extended the Green-function-based inversion algorithm to determine multifracture geometry. The robustness and accuracy of the inversion algorithm were tested through a four-fracture synthetic case with consideration of the LF-DAS measurement bias. A time-dependent constraint at the fracture-hit locations was added to the model to mitigate the nonunique inversion solutions caused by the limited strain dataset. After obtaining the fracture widths, we can roughly estimate the fracture height by minimizing the error between the calculated strain profile and true data. The analyses in this chapter demonstrated the potential of LF-DAS data for quantitative hydraulic-fracture geometry characterization and provided insights on better use of LF-DAS data.

CHAPTER 6

FIELD APPLICATION OF GREEN-FUNCTION-BASED INVERSION ALGORITHM*

6.1 Overview

In this chapter, we apply the proposed two-step workflow in Chapter 5 to a set of field examples. The field cases are stages T2, T3, and T4 presented in Chapter 4. Firstly, we use the Green-function-based inversion algorithm to estimate time-dependent fracture widths near the monitoring well. Secondly, we estimate the fracture height at the end of fluid injection by matching the measured strain profile with various fracture heights, assuming the inverted widths at the fracture-hit locations represent the average fracture widths near the monitoring well. As discussed in Chapter 4, the designed cluster number is 8 per stage and the cluster spacing is about 22-23 ft. The LF-DAS data were recorded along a horizontal monitoring well that is parallel to the treatment well. The two wells are in the same depth and the well spacing is 1300 ft. More details regarding the field cases were explained in Section 4.3.

6.2 Fracture Width Inversion

In this section, we focus on the fracture width inversion for three stages (i.e., T2 to T4 in Chapter 4). The details of the fracture-hit detection process were presented in Chapter 4 and are briefly reviewed in the following sections for completeness. After converting the LF-DAS data into strain rates using Eq. (4.2), the strain data (ε) are obtained by integrating the strain rates ($\dot{\varepsilon}$) over time (t), written as

$$\varepsilon\left(x,t_n\right)=\sum_{i=1}^{n}\dot{\varepsilon}\left(x,t_i\right)\Delta t\,, \tag{6.1}$$

where the subscript i is the timestep index, and Δt is the time interval. The strain data, excluding measurement bias around fracture-hit locations, are used for inversion.

6.2.1 Field Example One—Stage T2

Figure 6.1(a) shows the waterfall plot of strain rates over a large range of wellbore length, and Figure 6.1(b) is a zoomed-in view that is adapted from Chapter 4, in which the fractures that hit the monitoring well are labeled by the dash lines. There are five fractures in the current stage that hit the monitoring well, labeled by the black dash lines. Three fractures from the previous stage are re-activated because fracturing fluid leaks off into the previous stage during the stimulation process, labeled by red dash lines. The fractures are numbered in ascending order from the toe side to the heel side, as labeled by the white arrows in Figure 6.1(b).

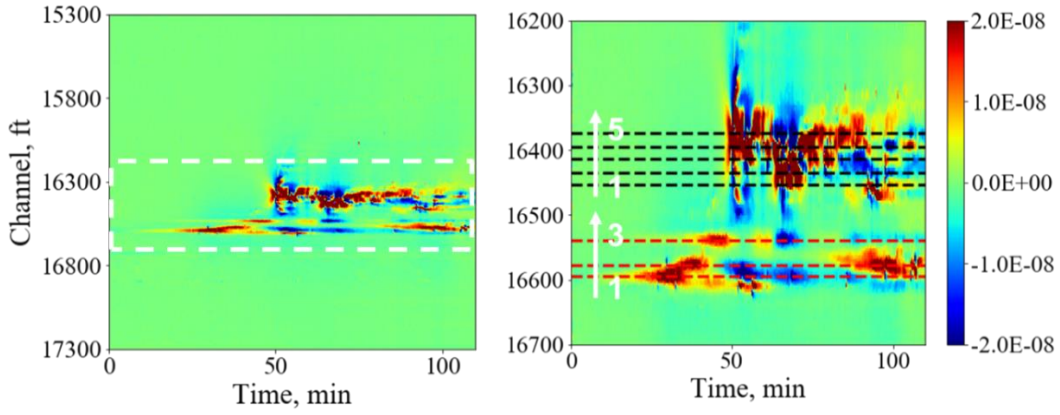

(a) (b)

Figure 6.1 (a) Waterfall plot of field strain-rate data (s^{-1}) and (b) zoom-in view of strain-rate waterfall plot with identified fracture hits (adapted from Liu et al. 2020d): five fractures in the current stage (labeled by black dash lines) and three re-activated fractures from the previous stage (labeled by red dash lines) (reprinted from Liu et al. 2021b).

Figure 6.2 presents the waterfall plots of LF-DAS measured strain data used for inversion (Figure 6.2(a)) and those calculated using the inverted widths (Figure 6.2(b)). The profile of the calculated strain data matches well with that of the field strain data. For a more straightforward comparison, Figure 6.3 compares the calculated strains and true strains along the monitoring well at two specific times, both showing good agreements.

Figure 6.4 shows different width profiles as a function of treatment time, together with the pumping curves. The summation of widths near the monitoring well of all eight fractures is shown in Figure 6.4(a), and the width summations of fractures in different stages are shown in Figure 6.4(b). The fracture width profiles in Figure 6.4(a) and Figure 6.4(b) can be divided into three periods, as labeled in Figure 6.4(a):

1. Before the first fracture hits the monitoring well in the current stage (~ 50 min), labeled by the black dash line, the width increase is attributed to the reopened fractures from the previous stage because of fracturing-fluid leakoff, which is illustrated by the zero fracture width in the current stage (red markers) and gradually increased fracture width in the previous stage (blue markers) in Figure 6.4(b).
2. Once the fractures in the current stage start hitting the monitoring well (Period 2), we observe an increasing trend of the width summation of fractures in the current stage and a decreasing trend of that in the previous stage before the injection stops, labeled by the black solid line in Figure 6.4(b). This is because the growth of fractures in the current stage suppresses the surrounding formation rock, which leads to closure of nearby fractures.
3. After the injection stops (Period 3), the total width summation keeps increasing (Figure 6.4(a)). Specifically, the width summation of the current stage shows a slight increase, while the width summation of the previous stage shows a more obvious increase (Figure 6.4(b)).

The aforementioned fracture-width behaviors are consistent with the LF-DAS strain-rate measurements (Figure 6.1(b)). Strong positive (red) strain rate signals are observed from the previous stage in the beginning (Period 1). After the fractures in the current stage hit the monitoring well, positive (red) strain-rate signals are obvious in the current stage, whereas the fiber sections in the previous stage detect negative (blue) signals indicating fracture closure. Finally, after the injection stops, positive (red) signals are

observed in the previous stage, especially at the channels corresponding to Fracture 2. On the contrary, negative (blue) signals are generally observed in the current stage, except for channels related to Fractures 3 and 4.

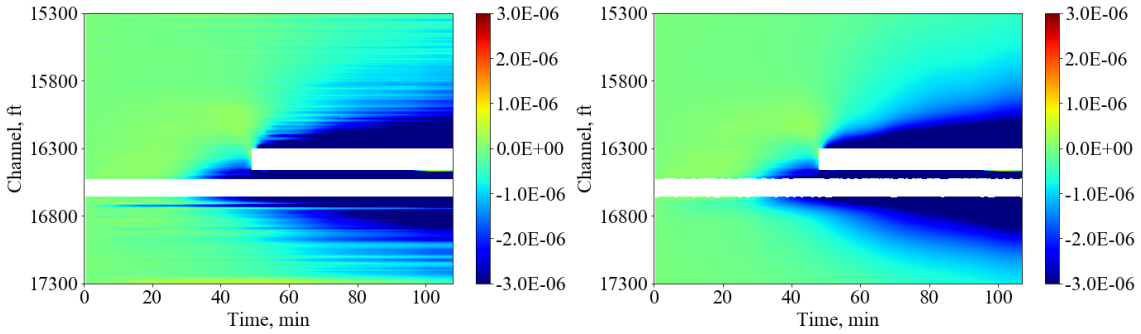

(a) (b)

Figure 6.2 Waterfall plots of (a) field strain data used for inversion and (b) calculated strain data for Stage T2 (reprinted from Liu et al. 2021b).

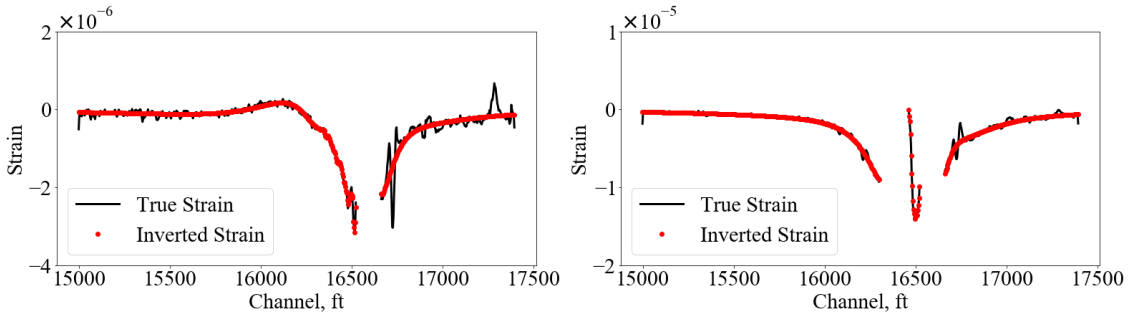

(a) (b)

Figure 6.3 Comparison of LF-DAS measured strain data and calculated strain data using the inverted widths at two times for Stage T2. (a): 42.4 min and (b): 98 min (reprinted from Liu et al. 2021b).

Figure 6.4(c) and Figure 6.4(d) show the width evolution of each individual fracture in the current stage and the previous stage, respectively. Similar to the width summation profiles, the time-serial width of each fracture is consistent with the LF-DAS measurements. At the end of fluid injection, the widths of open fractures near the monitoring well range from 0.2 mm to 0.4 mm in the current stage.

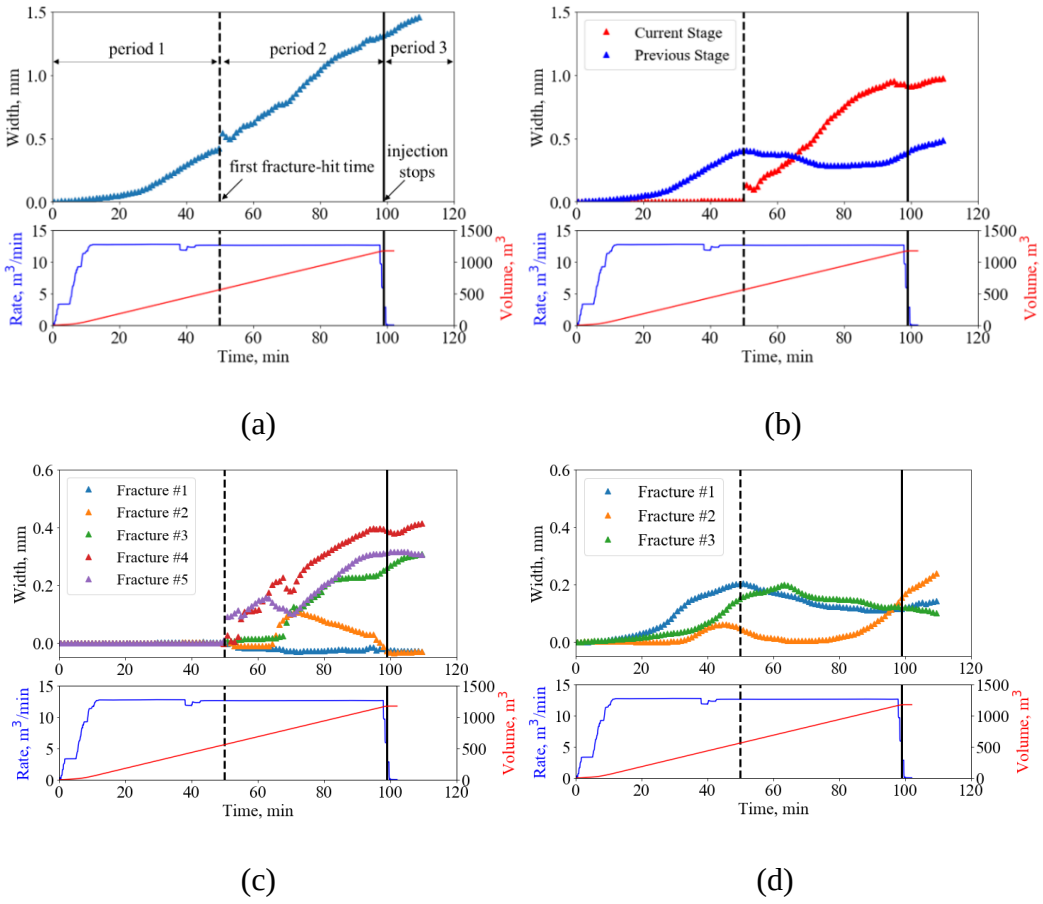

Figure 6.4 Fracture widths near the monitoring well as a function of treatment time of Stage T2. (a): width summation of all fractures; (b): width summation of fractures at each stage; (c): width of each individual fracture in the current stage; (d): width of each individual fracture in the previous stage. Black dash line indicates the first fracture-hit time; black solid line indicates the end of injection (reprinted from Liu et al. 2021b).

Taking Fracture 5 as an example (purple markers), this fracture hit of the current stage occurs at about 50 min when the width starts increasing until about 65 min. The LF-DAS measurements show a decreasing trend between 65 min and 75 min, and correspondingly the width keeps decreasing within this time interval. After that, the width shows an increasing trend until the end of injection, which is consistent with the LF-DAS strain-rate responses as well.

6.2.2 Field Example Two—Stage T3

Figure 6.5(a) shows the strain rates converted from the field LF-DAS measurements and Figure 6.5(b) is a zoomed-in view with identified fracture hits labeled by the dash lines for Stage T3. Similar to Stage T2, during the stimulation treatment of the presented field example, the fracturing fluid leaks off into the previous stage that re-activates existing fractures, as labeled by the red dash lines. Four fractures that hit the monitoring well are identified labeled by the black dash lines. The fractures are number in ascending order from the toe side to the heel side in each stage, indicated by the white arrows in Figure 6.5(b).

The strain-rate data in Figure 6.5(a) is integrated in time to obtain the strain data for inversion. Figure 6.6 compares the field LF-DAS strain data used for inversion (Figure 6.6(a)) and the calculated strain profile using the inverted fracture widths (Figure 6.6 (b)). It should be noted that the strain data near the fractures are excluded for the inversion due to the measurement bias. Clearly, the calculated strains using the inverted widths match well with the field LF-DAS strain data for all time steps. Figure 6.7 compares quantitatively the field strain profiles and the calculated ones along the monitoring well at

two specific time steps (i.e. 42.4 min and 62.5 min), both showing good agreements. The good fittings of the strain profiles confirm that the inverted widths are reliable.

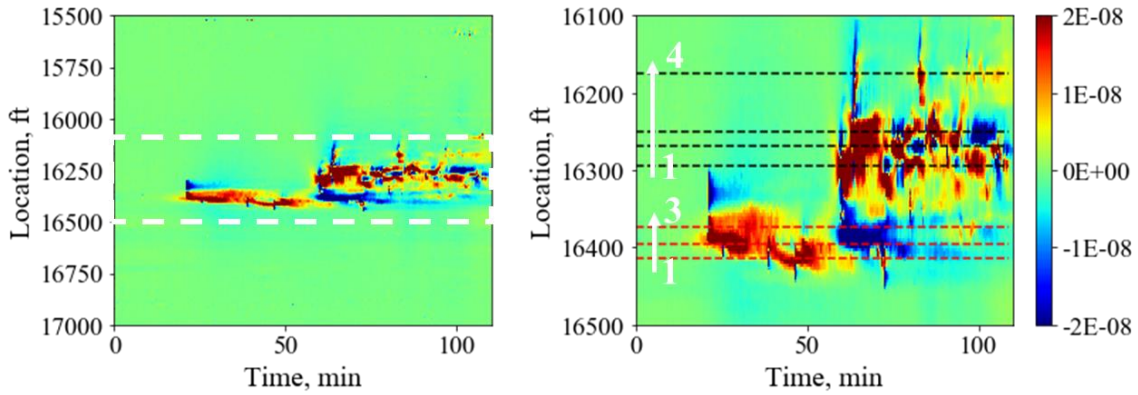

(a) (b)

Figure 6.5 (a) Waterfall plot of field strain-rate data (s^{-1}) and (b) zoom-in view of strain-rate waterfall plot with identified fracture hits (adapted from Liu et al. 2020d): four fractures in the current stage (labeled by black dash lines) and three re-activated fractures from the previous stage (labeled by red dash lines) (reprinted from Liu et al. 2021a).

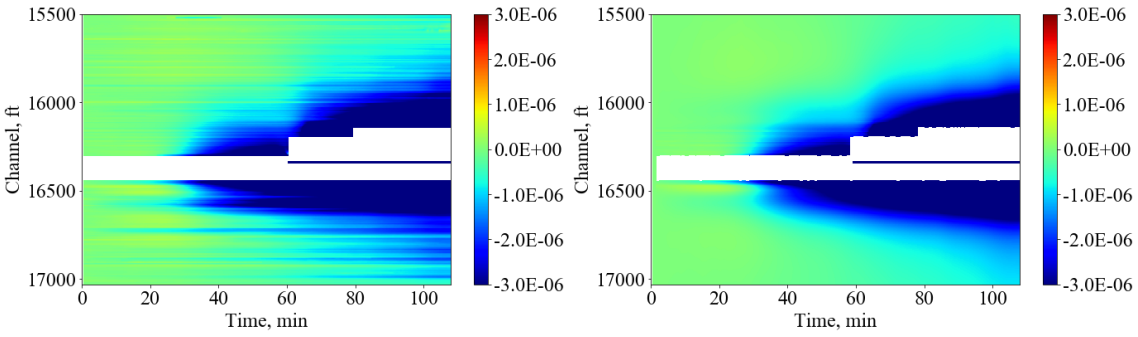

(a) (b)

Figure 6.6 Waterfall plots of (a) field LF-DAS strain data and (b) calculated strain data by the inversion algorithm for Stage T3 (reprinted from Liu et al. 2021a).

We present the width profiles in the same presentations as those of Stage T2. Figure 6.8 shows different width profiles as a function of treatment time. Figure 6.8(a) is the width summation of all the seven fractures from both the current and previous stages, whereas Figure 6.8(b) presents the width summations of fractures in the two separate stages. Between 20 min and 60 min, the width increase is mainly due to the fracture re-activation from the previous stage. At about 60 min, the first fracture in the current stage hits the monitoring well, followed by another two fractures afterward shortly, and Fracture 4 hits the monitoring well at about 80 min, as shown in Figure 6.8(b). Therefore, starting from 60 min, the width of fractures at the current stage increases, as indicated by the red markers in Figure 6.8(b).

It is interesting to note the decreasing trend of fracture width from the previous stage between 60 min and about 76 min. This is because the fractures in the current stage have reached the monitoring well and the growth of these fractures suppresses the surrounding matrix, which leads to fracture closure in the previous stage. The inversion results are consistent with the LF-DAS strain-rate measurements: strong negative (blue) signals are observed in this period indicating fracture closure.

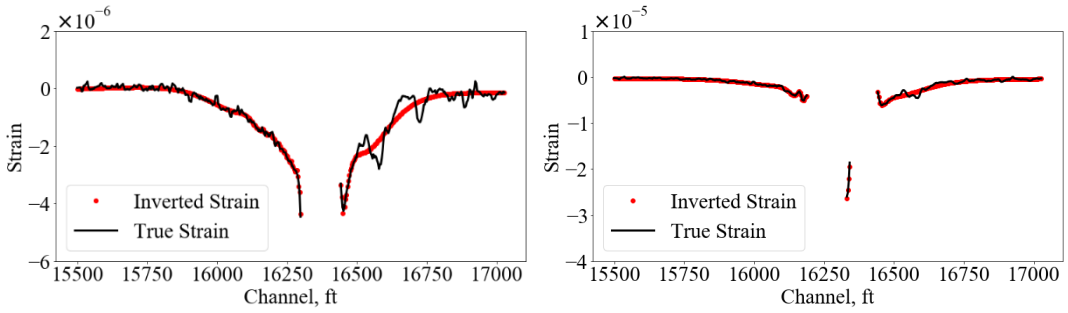

(a) (b)

Figure 6.7 Comparison of LF-DAS measured strain data and calculated strain data using the inverted widths at two times for Stage T3. (a): 42.4 min and (b): 62.5 min (reprinted from Liu et al. 2021a).

Figure 6.8 (c) and Figure 6.8(d) show the time-dependent width profile of each fracture in the current stage and in the previous stage during the treatment, respectively. The dynamic fracture-width variations (i.e. opening/closing) due to fracture interactions are captured, which are consistent with the field LF-DAS measurements. For instance, Fracture 3 in the current stage hits the monitoring well around 60 min and the width starts increasing from 60 min. At about 75 min, the width shows a slight decrease until about 80 min. Correspondingly, the LF-DAS measurements are negative in this time interval, clearly shown in Figure 6.6(b). Then, the width increases again until about 98 min, after which it shows an obvious reduction. This is because the injection stops at about 98 min, and Fracture 3 closes. Overall, the inversion results are consistent with the LF-DAS measurements.

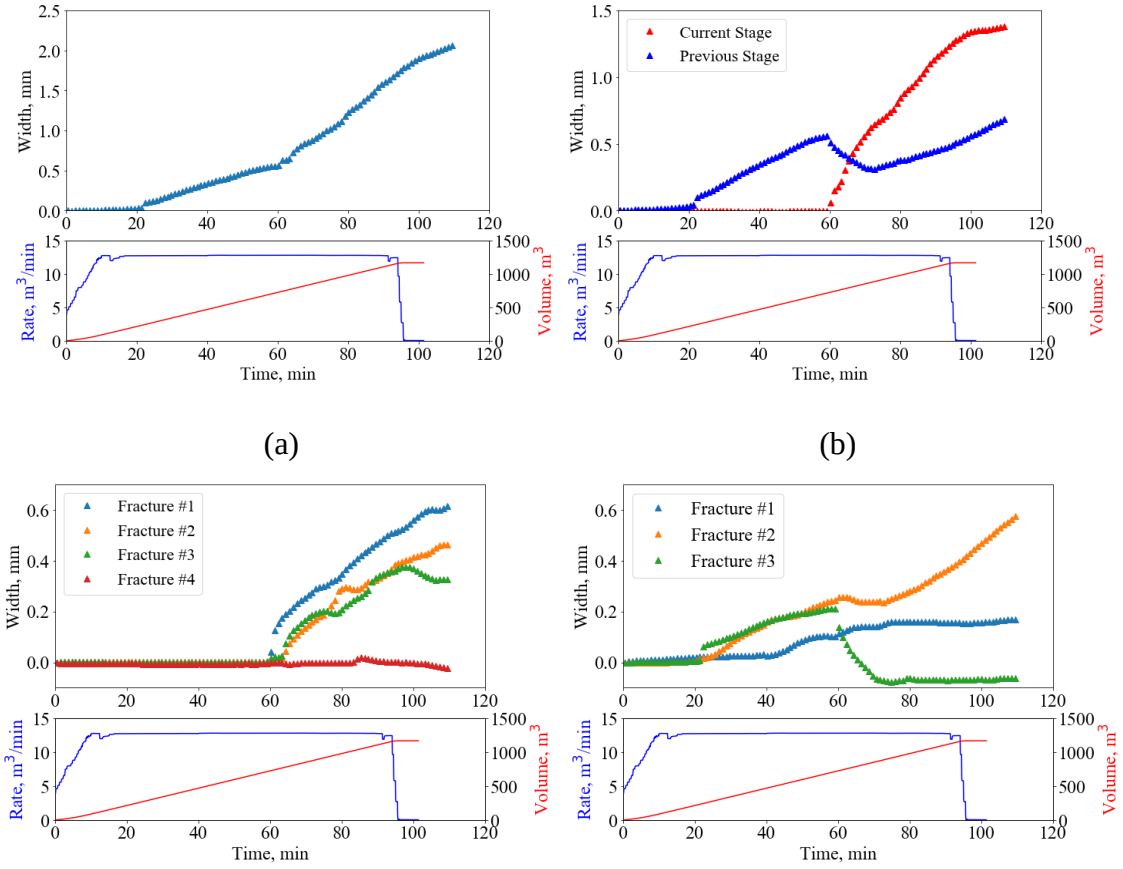

Figure 6.8 Fracture widths near the monitoring well as a function of treatment time of Stage T3. (a): width summation of all fractures; (b): width summation of fractures at each stage; (c): width of each individual fracture in the current stage; (d): width of each individual fracture in the previous stage (adapted from Liu et al. 2021a).

6.2.3 Field Example Three—Stage T4

Field example three is stimulated following the second example presented above. Figure 6.9(a) presents the LF-DAS strain-rate data and Figure 6.9(b) shows a zoomed-in

view with detected fracture hits labeled by the dash lines. Five out of eight designed fractures hit the monitoring well, as labeled by the black dash lines. Two fractures from the previous stage take fracturing fluid and are re-activated, as indicated by the red dash lines. Figure 6.10(a) is the strain data used for the inversion and Figure 6.10(b) presents the calculated strain data, which shows good agreement with the input data. Similar to the preceding field examples, we compare the strain profiles at two selected times (i.e. 42.4 min and 62.5 min) in Figure 6.11, which straightforwardly illustrates the good matches between the true data and calculated data.

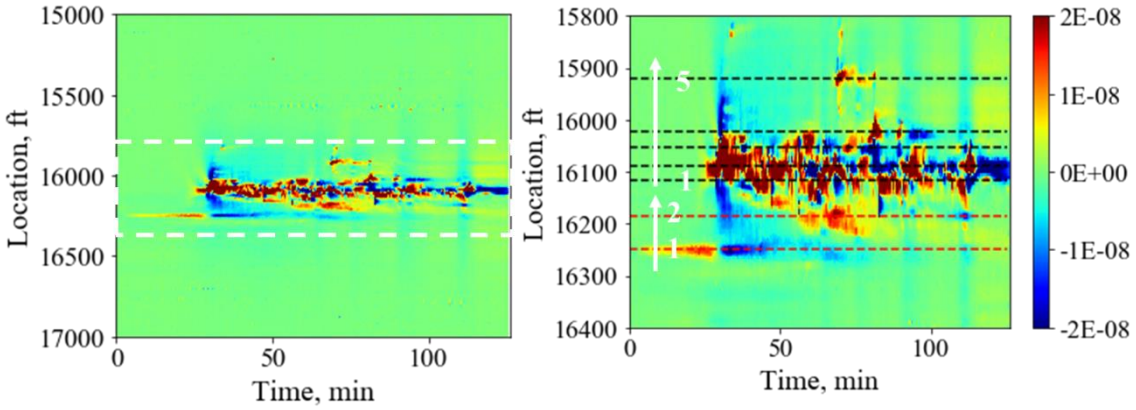

(a) (b)

Figure 6.9 (a) Waterfall plot of field strain-rate data (s^{-1}) and (b) zoom-in view of strain-rate waterfall plot with identified fracture hits (adapted from Liu et al. 2020d): five fractures in the current stage (labeled by black dash lines) and two re-activated fractures from the previous stage (labeled by red dash lines) (reprinted from Liu et al. 2021a).

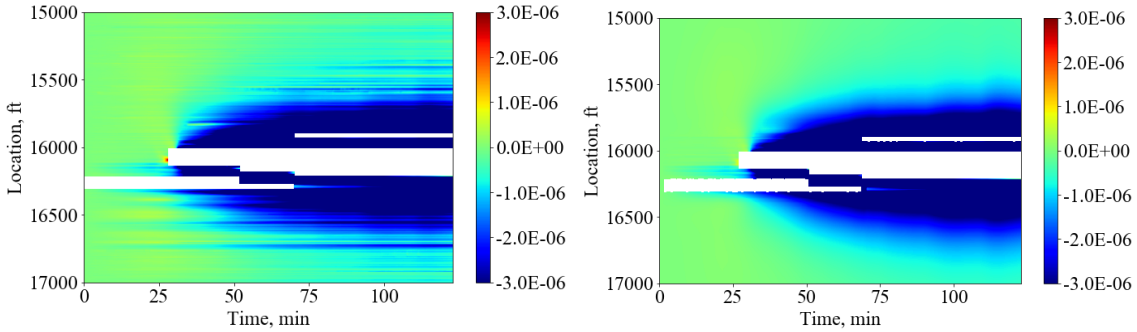

(a) (b)

Figure 6.10 Waterfall plots of (a) field LF-DAS strain data and (b) calculated strain data by the inversion algorithm for Stage T4 (reprinted from Liu et al. 2021a).

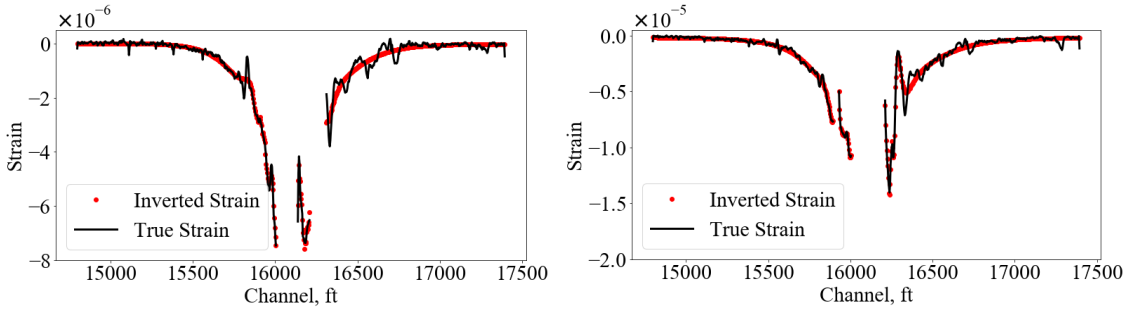

(a) (b)

Figure 6.11 Comparison of LF-DAS field strain data and calculated strain by the inversion algorithm at two specific time steps for Stage T4. (a): 42.4 min; (b): 73.9 min (reprinted from Liu et al. 2021a).

Figure 6.12 shows the width evolutions in different forms as a function of treatment time. The width summation of all the seven fractures from both the current and previous stages is shown in Figure 6.12(a), while the width summations of fractures in different stages are shown in Figure 6.12(b). The width summation in Figure 6.12(a) starts showing an obvious increase at about 30 min when the first fracture in the current stage

hits the monitoring well. Before 30 min, the width summation shows a slight increase mainly due to the reopening of Fracture 1 in the previous stage. This minimal contribution from the previous stage to the width increase indicates that there is little fracturing fluid leaking off into the previous stage, which is evidenced by the weak LF-DAS signals at locations (channels) corresponding to the previous stage, as shown in Figure 6.9(b).

Figure 6.12(c) and Figure 6.12(d) show the width variations of each individual fracture in the current stage and the previous stage, respectively. In general, the width profiles are consistent with the LF-DAS measurements, which exhibit obvious fracture interactions (i.e. dynamic fracture opening/closing). Taking Fracture 2 in the current stage as an example, it firstly hits the monitoring well at about 30 min and its width keeps growing until about 60 min. After 60 min, the width profile shows a waving signature, which is a reliable result of inversion of the compressing-alternating-extending LF-DAS measurements, as shown in Figure 6.9(b). This waving signature is due to the competition among individual fractures through stress-shadow effects. When one fracture is opening, the adjacent fractures may be closing. The other width profiles also show consistent behaviors with the LF-DAS signals.

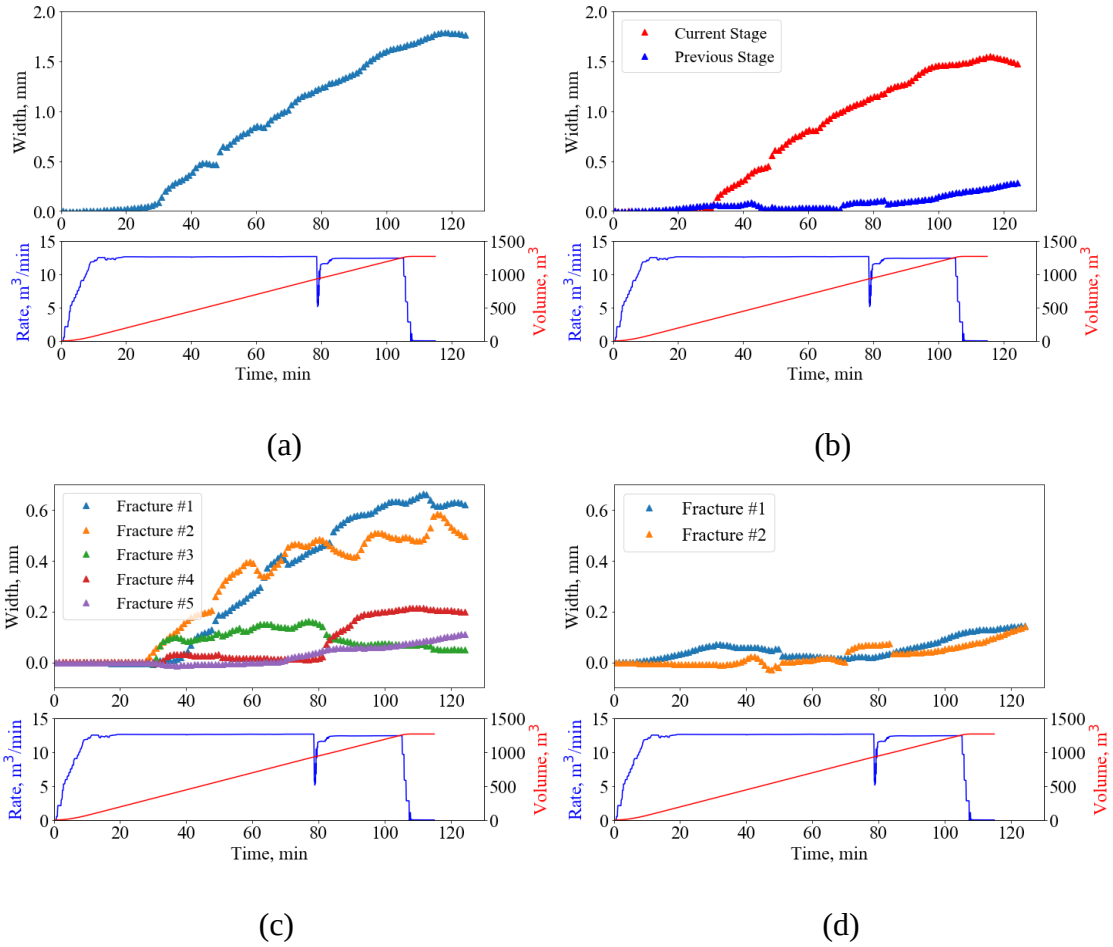

Figure 6.12 Fracture widths near the monitoring well as a function of treatment time of Stage T4. (a): width summation of all fractures; (b): width summation of fractures at each stage; (c): width of each individual fracture in the current stage; (d): width of each individual fracture in the previous stage (adapted from Liu et al. 2021a).

6.3 Fracture Height Estimation

After obtaining the inverted fracture widths, we could roughly estimate the fracture height by matching the LF-DAS field strain data, assuming the inverted widths represent the average widths near the monitoring well. We further assume the heights of fractures

in each stage are the same. In Stage T1, due to the lacking information regarding the estimated height of fractures from the previous stage, we assume the same height for all eight fractures. We calculate the strain profiles with different fracture heights, ranging from 40 meters to 100 meters. Figure 6.13(a) shows the average absolute errors between calculated strains and measured strains with different fracture heights, normalized by the minimum error. The results indicate that the error is smallest when the fracture height is approximately 80 m, beyond which the error does not show much difference. To visualize the differences, Figure 6.13(b) compares the strain profiles calculated with different heights against the measured true strains along the monitoring well, which clearly shows that the strain profiles match well with the true data when the height is over 80 meters.

Following the same procedure, we estimate the heights for the Stage T3 and Stage T4. Figure 6.14 and Figure 6.15 present the errors and strain profiles for Stage T3 and Stage T4, respectively. The results indicate that the fracture height of Stage T3 is approximately 55 m and that of Stage T4 is about 80 m. The range of fracture height obtained from this study is similar to that inferred from the analyses of DAS, microseismic, and pressure data recorded along a vertical well in the same formation (Raterman et al. 2018).

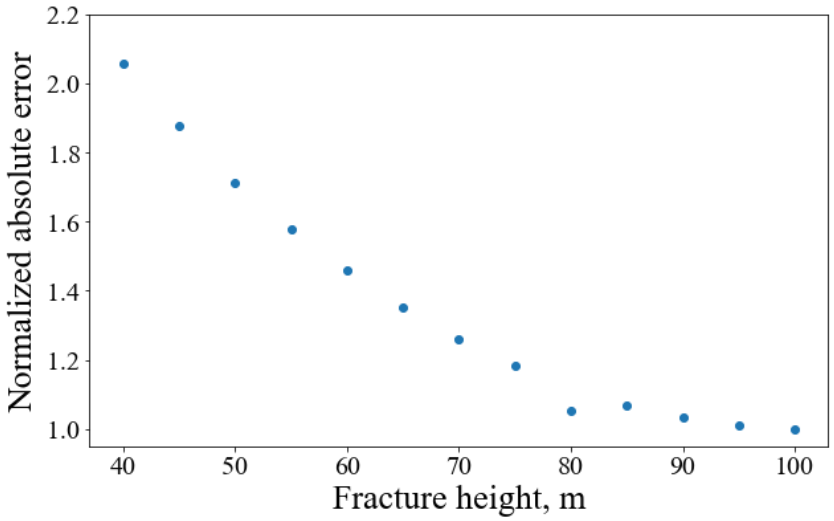

(a)

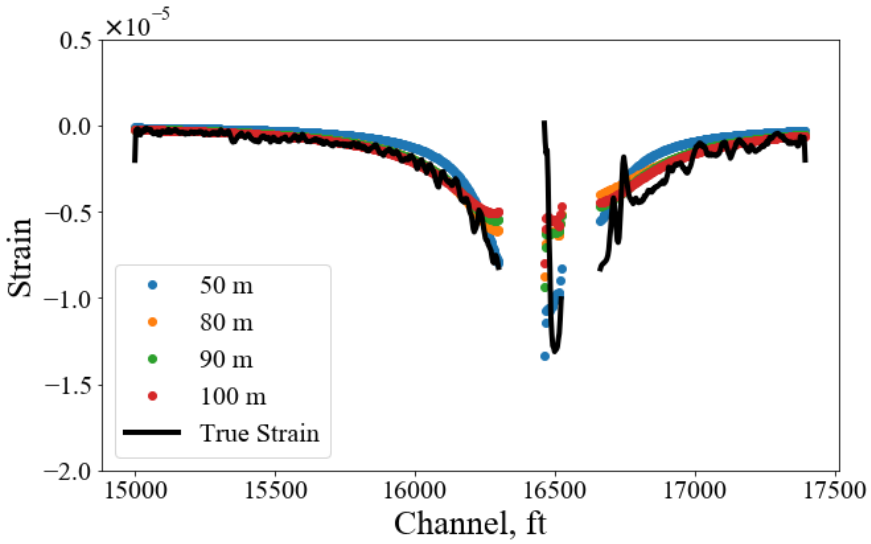

(b)

Figure 6.13 (a) Normalized absolute errors between calculated strains and measured strains with different fracture heights; (b) strain profiles calculated with fracture heights of 50 m, 80 m, 90 m, and 100 m, together with measured field strain profile for Stage T2.

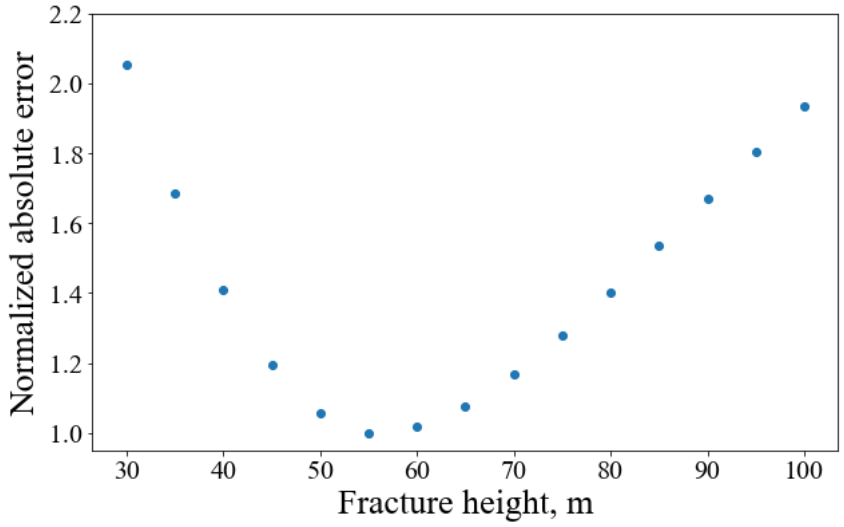

(a)

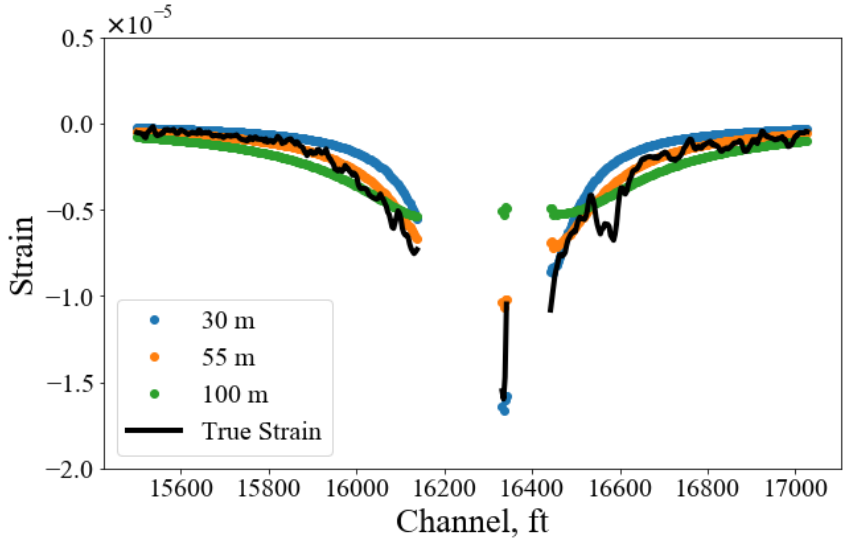

(b)

Figure 6.14 (a) Normalized absolute errors between calculated strains and measured strains with different fracture heights; (b) strain profiles calculated with fracture heights of 30 m, 55 m, and 100 m, together with measured field strain profile for Stage T3 (reprinted from Liu et al. 2021a).

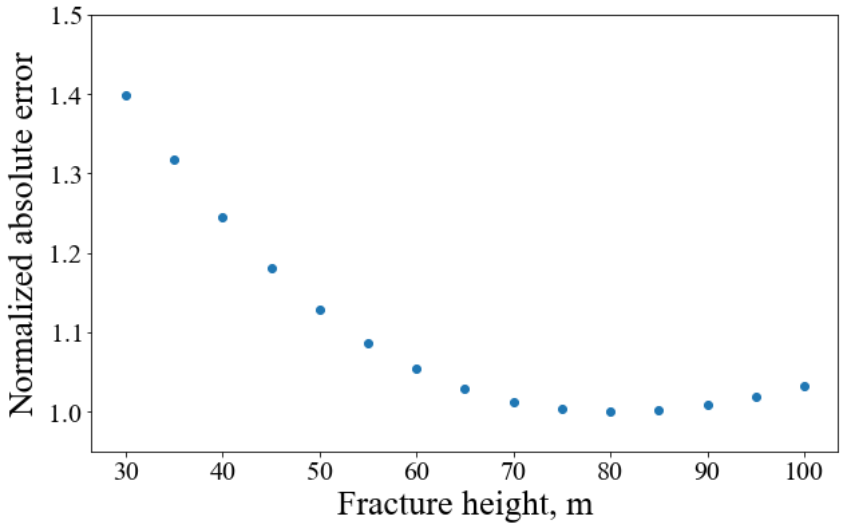

(a)

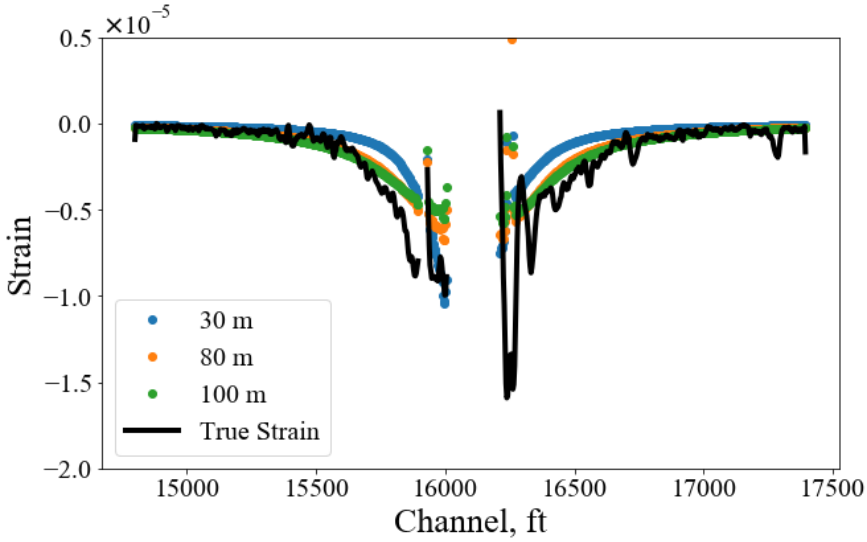

(b)

Figure 6.15 (a) Normalized absolute errors between calculated strains and measured strains with different fracture heights; (b) strain profiles calculated with fracture heights of 30 m, 80 m, and 100 m, together with measured field strain profile for Stage T4 (reprinted from Liu et al. 2021a).

6.3 Summary

In this chapter, we applied the proposed Green-function-based inversion algorithm to a set of field examples with an eight-cluster completion design. The workflow consists of two steps: firstly, we inverted the fracture widths near the monitoring well. After we obtained the fracture widths, we further estimated the fracture height with additional assumptions. For example, in this study, we assumed the inverted widths are average fracture widths near the monitoring well. Then the error between the calculated strains and field measurements should be decreasing, as the fracture height gets close to the true value. After obtaining the fracture width and height, the fracture length can be constrained under additional assumptions such as regular fracture shape and injected fluid mass balance. However, in multifracture cases, we may have little information about fractures that do not hit the monitoring well, which introduces complexity and uncertainties in characterizing the full fracture dimensions. Nevertheless, these challenges can be addressed by well design and fiber deployment. For instance, it is recommended to have multiple monitoring wells with different offset distances or to combine with in-well fiber optic sensing data to better constrain the hydraulic fracture geometry.

CHAPTER 7

QUANTIFICATION OF THERMAL EFFECTS ON CROSS-WELL LOW-FREQUENCY DISTRIBUTED ACOUSTIC SENSING MEASUREMENTS*

7.1 Overview

LF-DAS measures formation rock strains or strain rates, induced by both mechanically and thermally induced deformations near the monitoring well. During cold fluid injection into subsurface reservoirs, the temperature difference between injected fluid and reservoir temperature may induce significant rock deformation. Without considering thermal-induced rock deformation may lead to inaccurate interpretation of LF-DAS signals. In Chapter 7, we present a two-dimensional thermoelastic model in an integral equation formulation to quantify the contribution of temperature perturbation to LF-DAS measurements. The model is developed based on the theory of thermoelasticity that incorporates linear elasticity and linear heat conduction, which is solved using a fictitious heat source method.

Different numerical experiments are conducted with various initial and boundary conditions, which represent a wide range of reservoir types including fractured unconventional and geothermal reservoirs. The temporal strains along a fiber are recorded

*Part of this chapter is reprinted with permission from "Quantification of Thermal Effects on Cross-Well Low-Frequency Distributed Acoustic Sensing Measurements" by Liu, Y., Wu, K., Jin, G., and Moridis, G., 2021. *Unconventional Recourses Technology Conference*, Copyright [2021] by Society of Petroleum Engineers.

and analyzed. The results provide practical insights on the interpretation of LF-DAS data in reservoirs where it is necessary to take temperature into consideration.

7.2 Fundamentals of Thermoelasticity

In this section, we briefly review the fundamentals of thermoelasticity, followed by the two-dimensional fundamental solutions for temperature, stresses, and displacements induced by a continuous point heat source. The theory of thermoelasticity couples the linear elastic constitutive equations and linear heat conduction (Banerjee 1994). In an isotropic formation, the linear elastic constitutive equations can be separated into two components: the deviatoric response and the volumetric response. The deviatoric component is written as

$$\varepsilon_{ij} = \frac{\sigma_{ij}}{2G}\left(i \neq j\right), \tag{7.1}$$

where ε_{ij} denotes the deviatoric strain, σ_{ij} denotes the deviatoric stress, and G represents the shear modulus. $i, j = 1, 2$ for two-dimensional problems. The volumetric component, including the thermal coupling term, is written as

$$\varepsilon_{kk} = \frac{\sigma_{kk}}{3K} + \alpha^T T\ , \tag{7.2}$$

where ε_{kk} denotes the volumetric strain, $\sigma_{kk}/3$ is the volumetric stress (mean stress), T is temperature, K is rock bulk modulus, and α^T is the volumetric thermal expansion coefficient. Combining Eqs. (7.1) and (7.2), the constitutive equation can also be written into a stress form as

$$\sigma_{ij} = 2G\varepsilon_{ij} + \frac{2G\nu}{(1-2\nu)}\varepsilon_{ij}\delta_{ij} + K\alpha^T T\delta_{ij}, \tag{7.3}$$

where ν is Poisson's ratio and δ_{ij} is Dirac delta function. Assuming infinitesimal deformation, strain components are related to the rock displacements following

$$\varepsilon_{ij} = \frac{1}{2}\left(\frac{\partial u_i}{\partial x_j} + \frac{\partial u_j}{\partial x_i}\right). \tag{7.4}$$

Satisfying the momentum balance

$$\sigma_{ij,j} = 0, \tag{7.5}$$

we obtain the partial differential equations for the displacement field by substituting Eqs. (7.3) and (7.4) into Eq. (7.5), neglecting the body force, written as

$$Gu_{i,jj} + \left(\frac{G}{1-2\nu}\right)u_{j,ji} - \alpha^T K T_{,i} = 0. \tag{7.6}$$

Heat flow is described by the Fourier's law, which is written as

$$q_i^T = -k^T T_{,i}, \tag{7.7}$$

where k^T represents the thermal conductivity. The linearized entropy balance equation is (Ghassemi and Zhang 2004)

$$T_a \frac{\partial \varsigma}{\partial t} + q_{i,i} = \vartheta \tag{7.8}$$

where T_a is the absolute temperature. ς denotes the entropy of the rock per unit reference volume that is written as $\varsigma = \left(\rho c_p T\right)/T_a$ and c_p is the rock specific heat. ρ is rock density and ϑ denotes a heat source/sink term. Combining Eqs. (7.7) and (7.8), we obtain the equation for the temperature field as

$$\frac{\partial T}{\partial t} = c^T T_{,ii} + \frac{1}{\rho c_p}\vartheta, \tag{7.9}$$

where c^T is the thermal diffusivity, which is expressed as $c^T = k^T / \left(\rho c_p\right)$.

The 2D fundamental solutions for temperature, stresses, and displacements induced by a point heat source are given as (Zhang 2004, Ghassemi and Zhang 2004, Shen et al. 2003)

$$T^* = \frac{1}{4\pi k} Ei\left(\xi^2\right), \tag{7.10}$$

$$\sigma_{xx}^* = \frac{E\alpha}{24\pi k\left(1-\nu\right)}\left[\left(1-\frac{2x^2}{r^2}\right)\frac{1-e^{-\xi^2}}{\xi^2} - Ei\left(\xi^2\right)\right], \tag{7.11}$$

$$\sigma_{xy}^* = \frac{E\alpha}{24\pi k\left(1-\upsilon\right)}\left[\left(-\frac{2xy}{r^2}\right)\frac{1-e^{-\xi^2}}{\xi^2}\right], \tag{7.12}$$

$$\sigma_{yy}^* = \frac{E\alpha}{24\pi k\left(1-\upsilon\right)}\left[\left(1-\frac{2y^2}{r^2}\right)\frac{1-e^{-\xi^2}}{\xi^2} - Ei\left(\xi^2\right)\right], \tag{7.13}$$

$$u_x^* = \frac{\alpha\left(1+\upsilon\right)}{4\pi k\left(1-\upsilon\right)} r\left\{\frac{x}{r}\left[\frac{\left(1-e^{-\xi^2}\right)}{2\xi^2} + \frac{1}{2}Ei\left(\xi^2\right)\right]\right\}, \tag{7.14}$$

$$u_y^* = \frac{\alpha\left(1+\upsilon\right)}{4\pi k\left(1-\upsilon\right)} r\left\{\frac{y}{r}\left[\frac{\left(1-e^{-\xi^2}\right)}{2\xi^2} + \frac{1}{2}Ei\left(\xi^2\right)\right]\right\}, \tag{7.15}$$

where $r = \sqrt{x^2 + y^2}$, $\xi^2 = r^2 / \left(4c^T t\right)$, $Ei\left(u\right) = \int_u^\infty \frac{e^{-z}}{z} dz$. Eqs. (7.10)-(7.15) form the basis for the fictitious heat source method to solve the thermoelastic problem.

7.3 Fictitious Heat Source Method

For fracture-related problems, the fractures are treated as internal boundaries of an infinite, isotropic and homogeneous medium. The temperature field on the boundary can be approximated at any time by performing spatial integration over all boundary elements and temporal integration over time, written as

$$T\left(\mathbf{x},t\right)=\int_0^t\int_A T^{iH}\left(\mathbf{x}-\mathbf{x}',t-t'\right)D_H\left(\mathbf{x}',t'\right)dA\left(\mathbf{x}'\right)dt'+T_0\left(\mathbf{x}\right), \tag{7.16}$$

where A is the boundary surface area, t is evaluation time and T_0 is the temperature at the initial condition. T^{iH} is the instantaneous temperature change at $\mathbf{x}$ due to a unit heat source at $\mathbf{x}'$, which is calculated by integrating Eq. (7.10) over the element with half-length of a, written as

$$T^{iH}=\int_{-a}^{a}T^{*}ds=\frac{1}{4\pi k}\int_{-a}^{a}Ei\left(\xi^2\right)ds. \tag{7.17}$$

Temporal discretization is achieved by dividing the time domain into a number of constant time intervals and adopting a time marching scheme. For example, divide the fracture boundary into M total elements and divide the evaluation time t into N total time steps. The temperature integral equation can be written in a discretized form as

$$\begin{aligned}T\left(\mathbf{x},t\right)&=\int_0^t\int_A T^{iH}\left(\mathbf{x}-\mathbf{x}',t-t'\right)D_H\left(\mathbf{x}',t'\right)dA\left(\mathbf{x}'\right)dt'\\&=\left[\sum_{m=1}^{M}\int_{A_e}T^{iH}\left(\mathbf{x}-\mathbf{x}',\Delta t\right)dA\left(\mathbf{x}'\right)\right]\mathbf{D}_H\left(N\Delta t\right)\\&\quad+\sum_{l=1}^{N-1}\left[\sum_{m=1}^{M}\int_{A_e}T_{N-l+1}^{iH}\left(\mathbf{x}-\mathbf{x}',\Delta t\right)dA\left(\mathbf{x}'\right)\right]\mathbf{D}_H\left(l\Delta t\right)\end{aligned}, \tag{7.18}$$

where $\mathbf{D}_H\left(N\Delta t\right)$ is the unknown heat source vector that needs to be solved and $\mathbf{D}_H\left(l\Delta t\right)$ are the heat source vectors corresponding to time step *l*. At each time step, with initial and boundary temperature conditions, the heat source intensity can be solved, which is then used to calculate temperature, stresses, and displacements at any arbitrary observation point. Similar to Eq. (7.18), the discretized integral equations for stresses and displacements are written as follows

$$\begin{aligned}\sigma_{xx}\left(\mathbf{x},t\right) &= \int_0^t\int_A \sigma_{xx}^{iH}\left(\mathbf{x}-\mathbf{x}',t-t'\right)D_H\left(\mathbf{x}',t'\right)dA\left(\mathbf{x}'\right)dt' \\ &= \left[\sum_{m=1}^{M}\int_{A_e}\sigma_{xx}^{iH}\left(\mathbf{x}-\mathbf{x}',\Delta t\right)dA\left(\mathbf{x}'\right)\right]\mathbf{D}_H\left(N\Delta t\right) \\ &\quad +\sum_{l=1}^{N-1}\left[\sum_{m=1}^{M}\int_{A_e}\sigma_{xx}^{iH}\left(\mathbf{x}-\mathbf{x}',\Delta t\right)dA\left(\mathbf{x}'\right)\right]\mathbf{D}_H\left(l\Delta t\right)\end{aligned} \quad , \tag{7.19}$$

$$\begin{aligned}\sigma_{xy}\left(\mathbf{x},t\right) &= \int_0^t\int_A \sigma_{xy}^{iH}\left(\mathbf{x}-\mathbf{x}',t-t'\right)D_H\left(\mathbf{x}',t'\right)dA\left(\mathbf{x}'\right)dt' \\ &= \left[\sum_{m=1}^{M}\int_{A_e}\sigma_{xy}^{iH}\left(\mathbf{x}-\mathbf{x}',\Delta t\right)dA\left(\mathbf{x}'\right)\right]\mathbf{D}_H\left(N\Delta t\right) \\ &\quad +\sum_{l=1}^{N-1}\left[\sum_{m=1}^{M}\int_{A_e}\sigma_{xy}^{iH}\left(\mathbf{x}-\mathbf{x}',\Delta t\right)dA\left(\mathbf{x}'\right)\right]\mathbf{D}_H\left(l\Delta t\right)\end{aligned} \quad , \tag{7.20}$$

$$\begin{aligned}\sigma_{yy}\left(\mathbf{x},t\right) &= \int_0^t\int_A \sigma_{yy}^{iH}\left(\mathbf{x}-\mathbf{x}',t-t'\right)D_H\left(\mathbf{x}',t'\right)dA\left(\mathbf{x}'\right)dt' \\ &= \left[\sum_{m=1}^{M}\int_{A_e}\sigma_{yy}^{iH}\left(\mathbf{x}-\mathbf{x}',\Delta t\right)dA\left(\mathbf{x}'\right)\right]\mathbf{D}_H\left(N\Delta t\right) \\ &\quad +\sum_{l=1}^{N-1}\left[\sum_{m=1}^{M}\int_{A_e}\sigma_{yy}^{iH}\left(\mathbf{x}-\mathbf{x}',\Delta t\right)dA\left(\mathbf{x}'\right)\right]\mathbf{D}_H\left(l\Delta t\right)\end{aligned} \quad , \tag{7.21}$$

$$
\begin{aligned}
u_x(\mathbf{x},t) &= \int_0^t \int_A u_x^{iH}(\mathbf{x}-\mathbf{x}', t-t') D_H(\mathbf{x}', t')\, dA(\mathbf{x}')\, dt' \\
&= \left[\sum_{m=1}^{M} \int_{A_e} u_x^{iH}(\mathbf{x}-\mathbf{x}', \Delta t)\, dA(\mathbf{x}')\right] \mathbf{D}_H(N\Delta t) \\
&+ \sum_{l=1}^{N-1} \left[\sum_{m=1}^{M} \int_{A_e} u_x^{iH}(\mathbf{x}-\mathbf{x}', \Delta t)\, dA(\mathbf{x}')\right] \mathbf{D}_H(l\Delta t)
\end{aligned}, \tag{7.22}
$$

$$
\begin{aligned}
u_y(\mathbf{x},t) &= \int_0^t \int_A u_y^{iH}(\mathbf{x}-\mathbf{x}', t-t') D_H(\mathbf{x}', t')\, dA(\mathbf{x}')\, dt' \\
&= \left[\sum_{m=1}^{M} \int_{A_e} u_y^{iH}(\mathbf{x}-\mathbf{x}', \Delta t)\, dA(\mathbf{x}')\right] \mathbf{D}_H(N\Delta t) \\
&+ \sum_{l=1}^{N-1} \left[\sum_{m=1}^{M} \int_{A_e} u_y^{iH}(\mathbf{x}-\mathbf{x}', \Delta t)\, dA(\mathbf{x}')\right] \mathbf{D}_H(l\Delta t)
\end{aligned}, \tag{7.23}
$$

where the influence coefficients are obtained by integrating the point source fundamental solutions (i.e., Eqs. (7.10)-(7.15)) into solutions for a line source with a length of 2*a*.

As discussed in Chapter 2, the LF-DAS strain is linearly scaled strain over a predefined gauge length, therefore it is calculated from the displacements following

$$
\varepsilon_{ff} = \frac{u_f^{i+L/2} - u_f^{i-L/2}}{L}, \tag{7.24}
$$

where *f* indicates the direction along the fiber. *L* represents the predefined gauge length.

7.4 Model Validation

The implementation of the fictitious heat source method is validated against a point source problem, presented in Shen et al. (2013). The problem is simulated as a small wellbore with a constant heat source located within an infinite domain, as shown in Figure 7.1. The wellbore radius is assumed to be 0.1 m and the applied heat flux is then calculated as $1/2\pi R = 1.59$ W/m^2. The analytical solutions to this problem are basically the fundamental solutions given in Eqs. (7.10)-(7.15). In the numerical case, the wellbore is

divided into 60 boundary elements. The thermal and geomechanical properties as well as the initial and boundary conditions are summarized in Table 7.1.

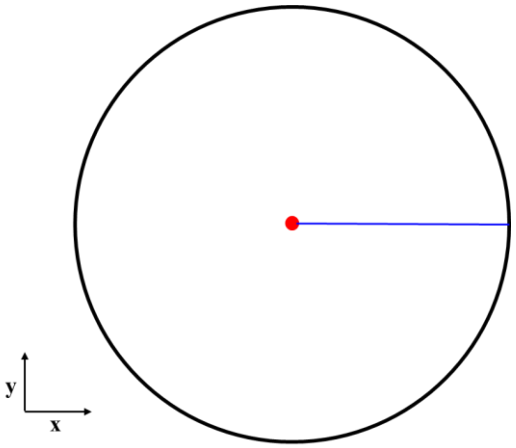

Figure 7.1 Schematic of an infinite radial domain with a heat source located in the center.

Table 7.1 Mechanical and thermal rock properties as well as initial and boundary conditions for a point heat source problem within a 2D infinite medium (adapted from Liu et al. 2021d).

Parameter (unit)	Value
Initial rock temperature (°C)	0
Young's modulus (GPa) and Poisson's ratio	75, 0.21
Rock specific heat (J/(kg•K))	1000
Rock density (kg/m^3)	2000
Rock thermal conductivity (W/(m•K))	4.0
Rock thermal expansion coefficient (1/K)	5.0×10^{-6}
Heat source strength (W)	1.0

Figure 7.2, Figure 7.3, and Figure 7.4 compare the numerical solutions against the analytical solutions of temperature, radial displacement, and stresses as a function of distance to the heat source along the *x*-axis (i.e., labeled by the blue line in Figure 7.1), respectively. The good agreements validate the implementation of this thermoelastic model using the fictitious heat source method.

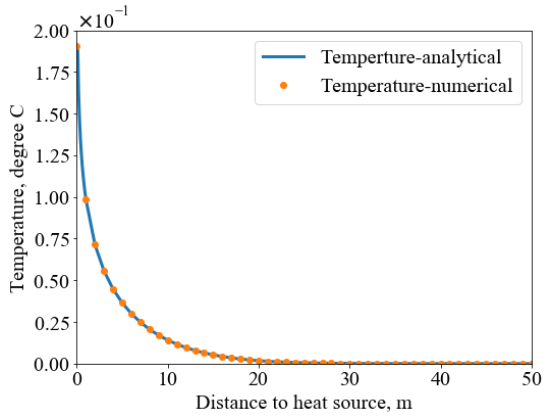

Figure 7.2 Comparison of temperature profiles as a function of distance to the wellbore between the numerical solution and analytical solution (reprinted from Liu et al. 2021d).

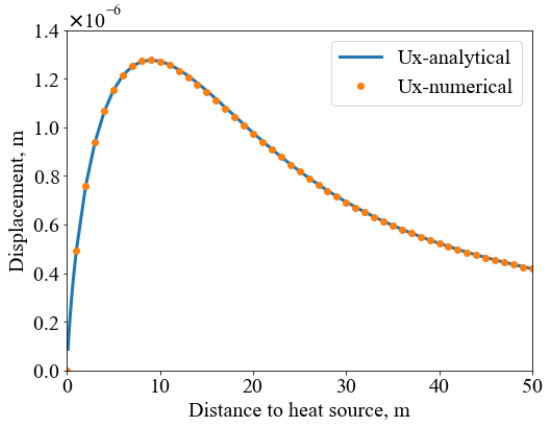

Figure 7.3 Comparison of displacement in the *x* direction as a function of distance to the wellbore between the numerical solution and analytical solution (reprinted from Liu et al. 2021d).

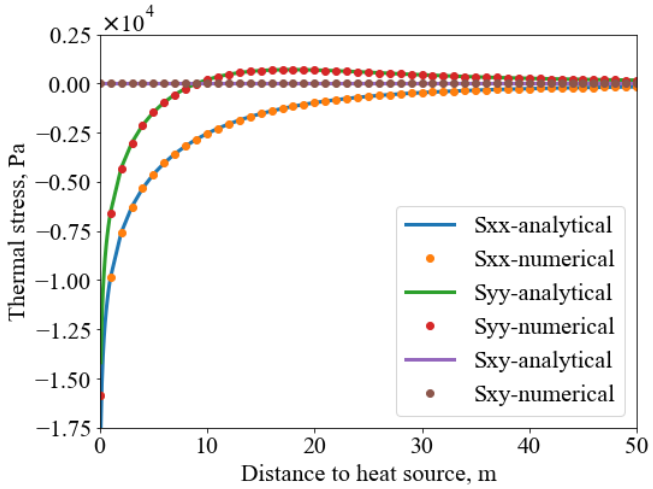

Figure 7.4 Comparison of stresses as a function of distance to the wellbore between the numerical solution and analytical solution (reprinted from Liu et al. 2021d).

7.5 Numerical Analysis of Thermal-Induced Rock Deformation around a Fracture

In this section, we quantify the thermal-induced rock deformation under various initial and boundary temperature conditions that represent the typical in-situ conditions of unconventional shale reservoirs and geothermal reservoirs. Figure 7.5 shows a schematic of the model setup that is used for the following simulation cases. There is a single planar fracture with a half-length of 75 m that is symmetric to the origin (0, 0). The fiber is located at x = 30 and parallel to the y-axis. In the following discussion, through Case 1, we firstly present the spatial distributions of temperature, displacement, and stress in the y-direction around the fracture to demonstrate the rock deformation characteristics induced by cold water injection. Then we focus on the temperature, displacement, and strain along the fiber.

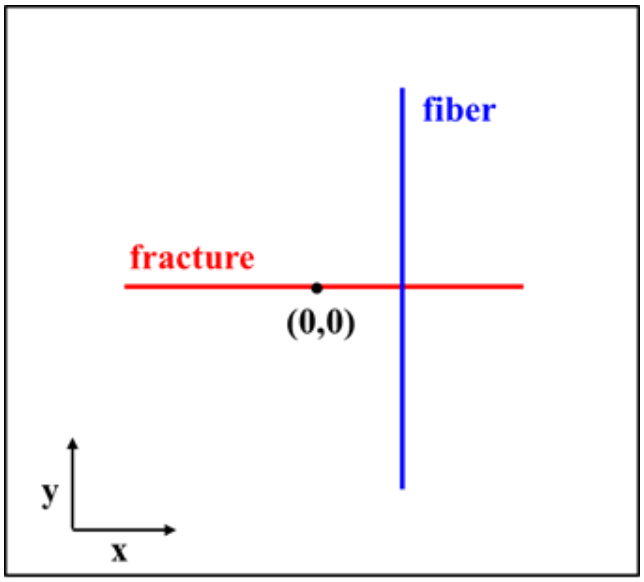

Figure 7.5 Schematic of simulation model setup consisting of a single planar fracture and a DAS fiber (reprinted from Liu et al. 2021d).

The geomechanical and thermal rock properties, initial reservoir temperature, and fracture temperature are summarized in Table 7.2. This model setting employs the downhole condition of typical unconventional reservoirs. The initial reservoir temperature is referred from the distributed temperature sensing (DTS) measurements from the Eagle Ford formation in Raterman et al. (2018). The DTS data also indicates that, when the fracturing fluid flows across the perforation during a stimulation job, the DTS measured temperature is about 40-50 °C. Therefore, we assume that the fracture temperature is 50 °C in Case 1. It should be noted that fracturing fluid may be warmed up by the formation in the far field (i.e., at cross wells). However, our cases in this chapter, assuming a constant fracture temperature with a pronounced difference to the reservoir temperature, are the extreme examples that maximize the thermal responses. If little thermal strain can be observed in those cases, it is unlikely that thermal strain is significant in the field data.

Table 7.2 Mechanical and thermal rock properties as well as initial and boundary conditions for Case 1 (adapted from Liu et al. 2021d).

Parameter (unit)	Value
Initial rock temperature (°C)	130
Young's modulus (GPa) and Poisson's ratio	27.5, 0.25
Rock specific heat (J/(kg•K))	1000
Rock density (kg/m^3)	2600
Rock thermal conductivity (W/(m•K))	3.0
Rock thermal expansion coefficient (1/K)	5.0×10^{-6}
Fracture temperature (°C)	50

Figure 7.6 shows the temperature distributions around the fracture after 1 day and 10 days. Clearly, the temperature gradually decreases in the vicinity of the fracture, but the temperature diffusion process is very slow and the associated area with temperature perturbation is also limited. Figure 7.7 shows the displacement field in the *y* direction (i.e., the direction along the fiber). After 1 day and 10 days. Fracture cooling shrinks the surrounding rock, indicated by the rock on each side of the fracture moving towards each other (i.e., fracture closing). As a result of fracture cooling, we observe tensile stress on the sides of the fracture, while compressive stress is observed around the fracture tips, as shown in Figure 7.8. Overall, the thermally induced rock deformation in the presented condition is not significant. In specific, the maximum induced displacement is less than 1 mm and the maximum induced stress (in the order of 10^5 Pa) is concentrated around the fracture tips after 10 days.

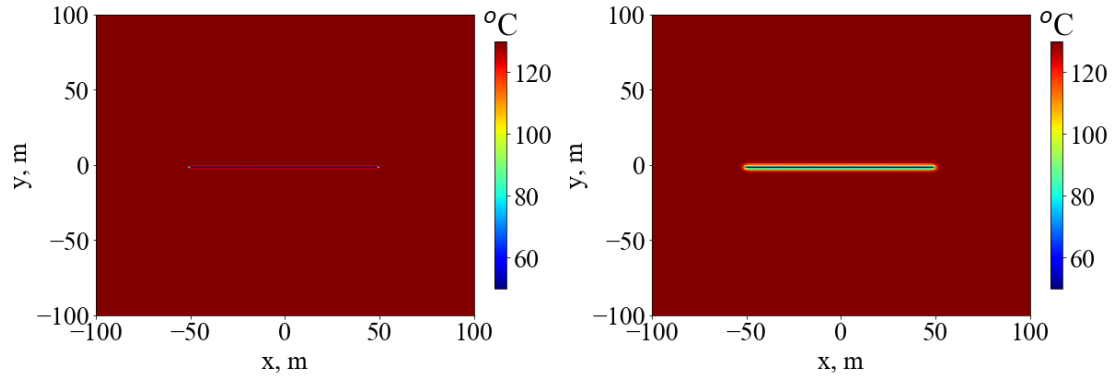

Figure 7.6 Temperature distribution after (a) 1 day and (b) 10 days (reprinted from Liu et al. 2021d).

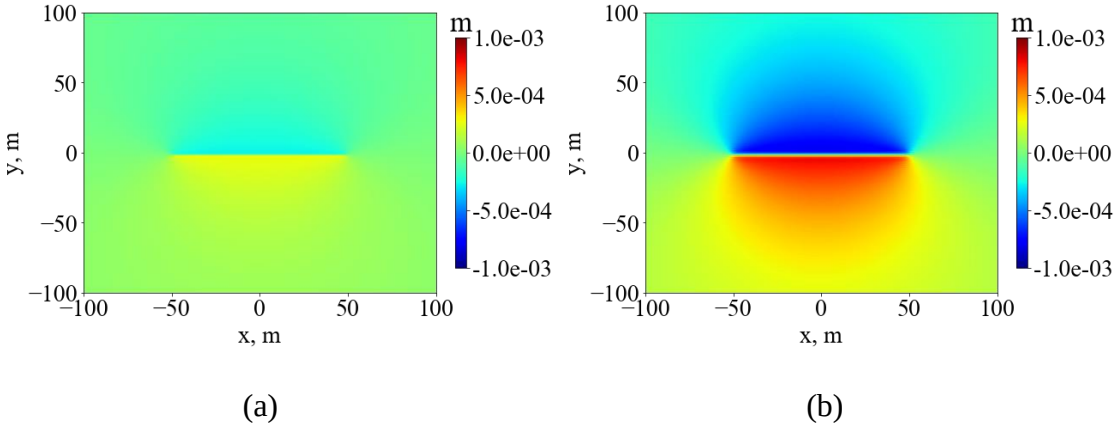

Figure 7.7 Spatial distribution of thermally induced displacement in the y direction after (a) 1 day and (b) 10 days (reprinted from Liu et al. 2021d).

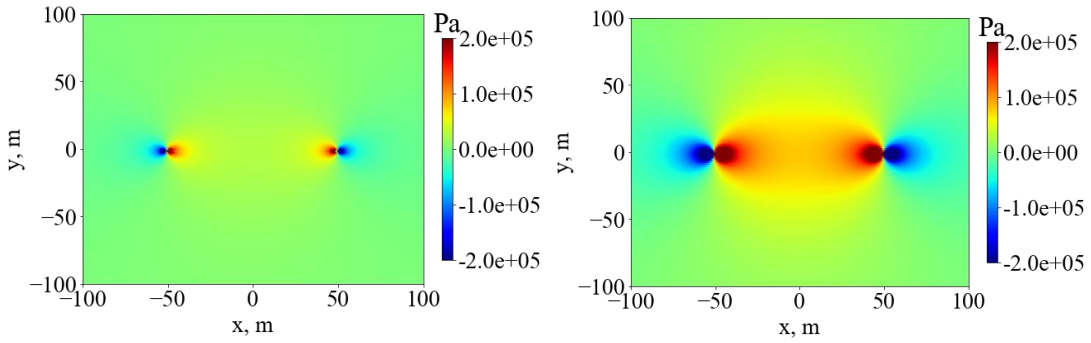

Figure 7.8 Spatial distribution of thermally induced stress in the y direction after (a) 1 day and (b) 10 days (reprinted from Liu et al. 2021d).

Figure 7.9, Figure 7.10, and Figure 7.11 show the temperature, displacement, and strain profiles along the fiber after 1 day and 10 days, respectively. The thermal effects are limited within 5 meters on each side of the fracture after 10 days, as indicated by the temperature profile along the fiber in Figure 7.9. Although the induced displacements gradually increase, the maximum value after 10 days is still less than 1 mm, as shown in Figure 7.10. The maximum strain after 1 day is about 1.0×10^{-4}, while it is about 3.0×10^{-4}, at 10 days. From Chapters 3 and 5, we can tell that the strains around the fractures induced by fracture opening are usually in the order of 10^{-3}. It should be noted that the stimulation process usually just lasts for about 2-3 hours for each stage. Within such a short period of time, the thermal effects may be negligible considering that it takes about 10 days for the maximum thermally induced strain to reach the order of 10^{-4}.

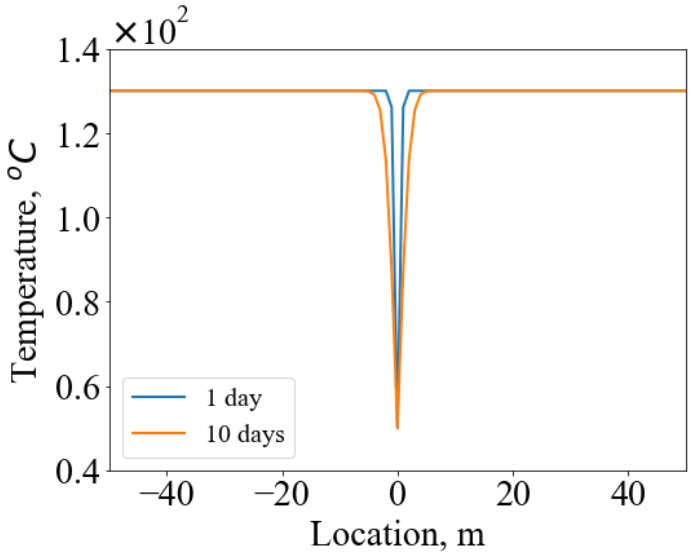

Figure 7.9 Temperature profiles along the fiber at two different times (i.e., 1 day and 10 days) of Case 1 (reprinted from Liu et al. 2021d).

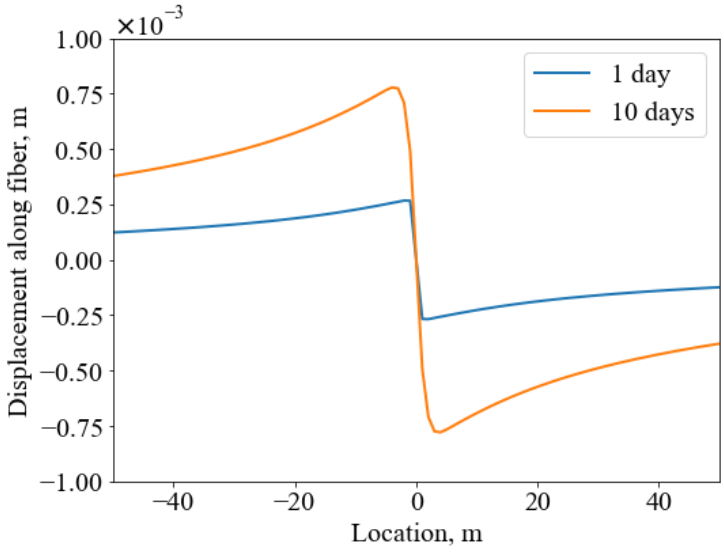

Figure 7.10 Displacement profiles along the fiber at two different times (i.e., 1 day and 10 days) of Case 1 (reprinted from Liu et al. 2021d).

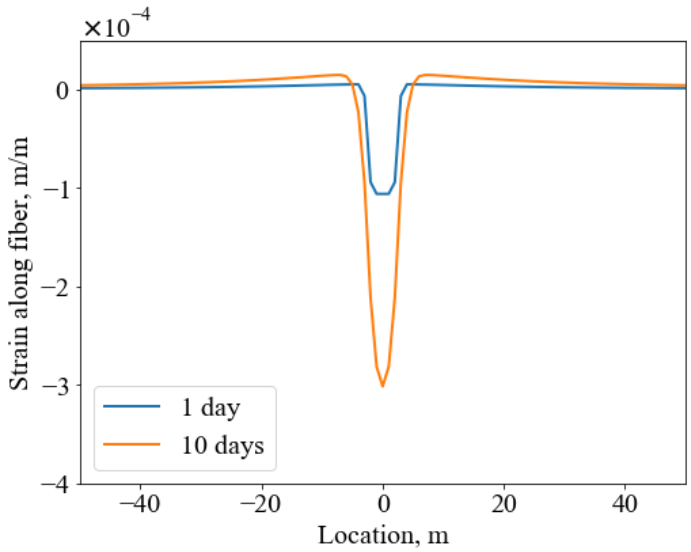

Figure 7.11 Strain profiles along the fiber at two different times (i.e., 1 day and 10 days) of Case 1 (reprinted from Liu et al. 2021d).

To investigate the thermally induced rock deformation under a larger difference between reservoir temperature and fracture temperature, we construct another two cases by increasing the reservoir temperature to 150 °C and 200 °C in Case 2 and Case 3, respectively. Figure 7.12, Figure 7.13, and Figure 7.14 compare the temperature, displacement, and strain profiles along the fiber among Cases 1-3 after 1-day simulation, respectively. Although we observe larger rock deformations as the temperature difference increases, the affected region does not show many changes, which is still limited to about 5 meters away from the fracture surface. Even when the temperature difference is as large as 150 °C, the maximum compression around the fracture-hit location still within the order of 10^{-4}.

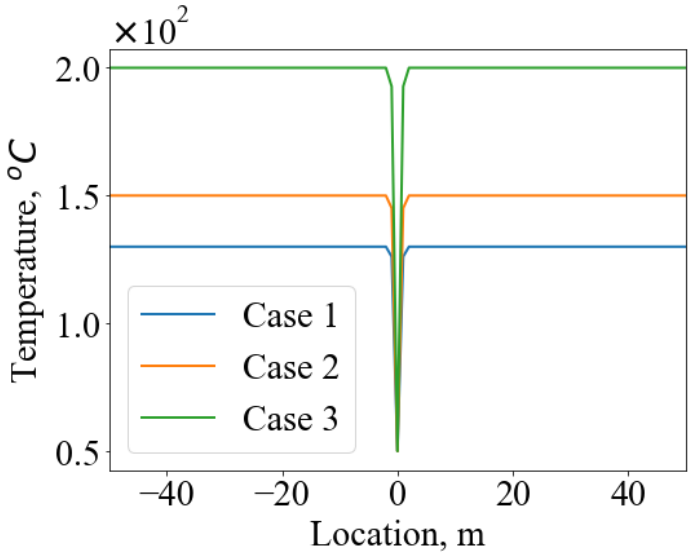

Figure 7.12 Comparison of temperature profiles along the fiber after 1 day among Case 1, Case 2, and Case 3 with different initial reservoir temperatures (reprinted from Liu et al. 2021d).

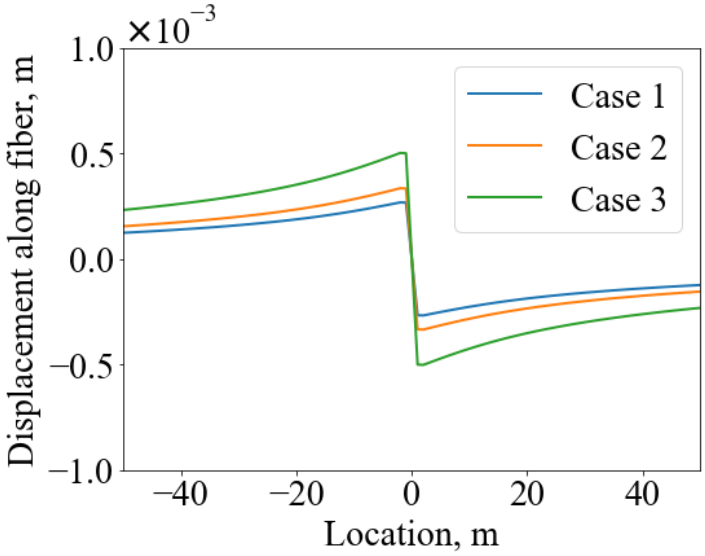

Figure 7.13 Comparison of displacement profiles along the fiber after 1 day among Case 1, Case 2, and Case 3 with different initial reservoir temperatures (reprinted from Liu et al. 2021d).

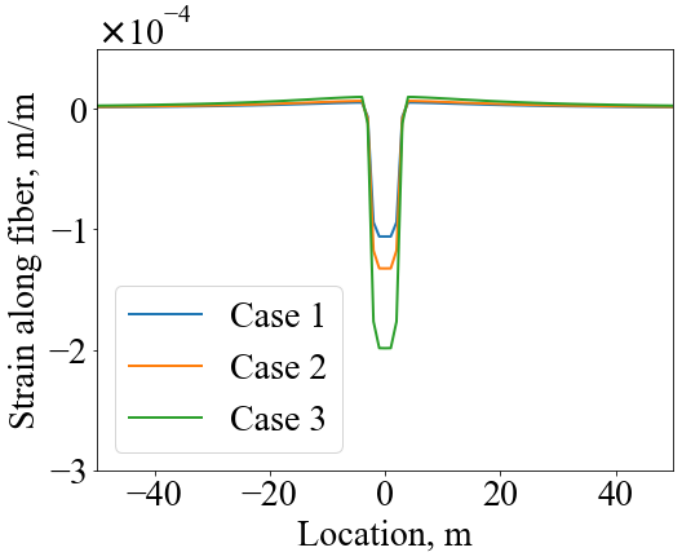

Figure 7.14 Comparison of strain profiles along the fiber after 1 day among Case 1, Case 2, and Case 3 with different initial reservoir temperatures (reprinted from Liu et al. 2021d).

In addition, the rock thermal conductivity may slightly vary because of different minerals. For shale reservoirs, the thermal conductivity is usually less than 5 W/(m•K) (Labus and Labus 2018; Balkan et al. 2017). Therefore, we construct another two cases to investigate the effect of thermal conductivity. The thermal conductivity is changed to 4 W/(m•K) in Case 4, while it is changed to 5 W/(m•K) in Case 5. Figure 7.15, Figure 7.16, and Figure 7.17 respectively show the temperature, displacement, and strain profiles along the fiber of Case 1 and Cases 4-5 after 1-day simulation. Similar to the impacts of temperature difference, rock deformation is more pronounced with higher thermal conductivity. However, the thermally induced deformations are negligible compared to those induced by fracture opening. In summary, thermal effects on LF-DAS measurements in unconventional reservoirs are limited to the near-fracture region and the maximum

thermally induced strain is usually more than one order smaller than that induced by mechanical deformation during hydraulic fracturing treatments.

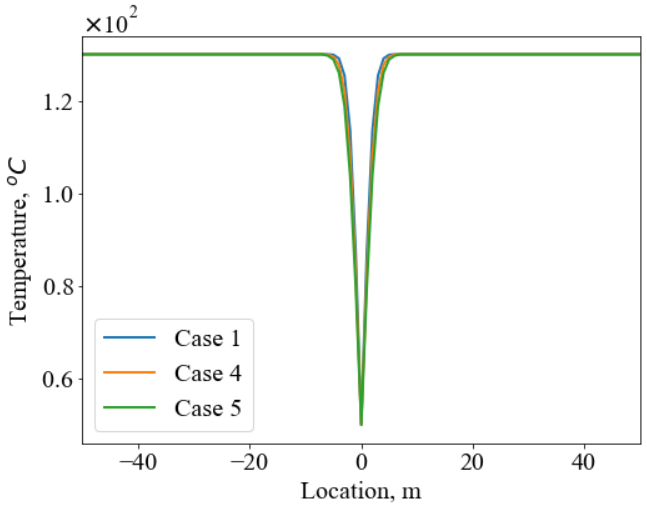

Figure 7.15 Comparison of temperature profiles along the fiber after 1 day among Case 1, Case 4, and Case 5 with different thermal conductivities (reprinted from Liu et al. 2021d).

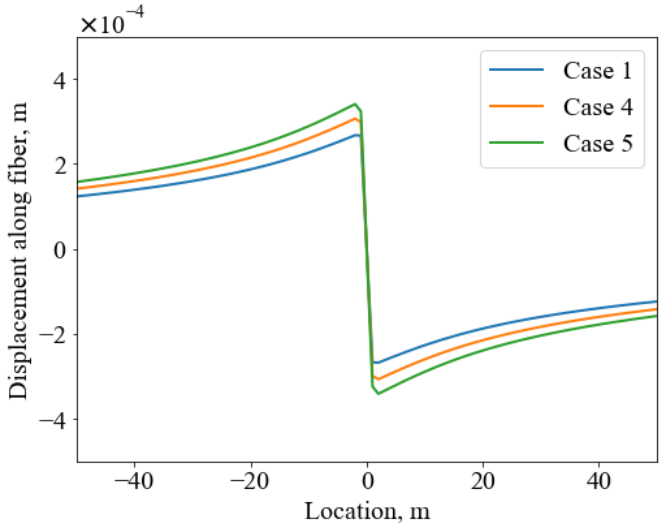

Figure 7.16 Comparison of displacement profiles along the fiber after 1 day among Case 1, Case 4, and Case 5 with different thermal conductivities (reprinted from Liu et al. 2021d).

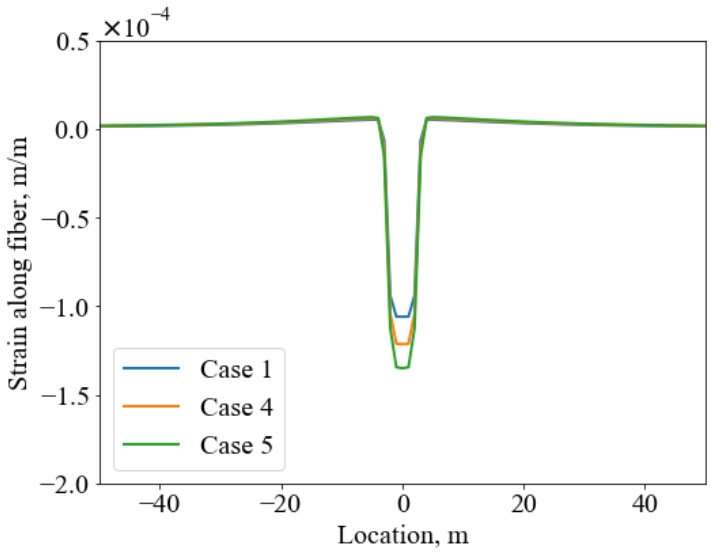

Figure 7.17 Comparison of strain profiles along the fiber after 1 day among Case 1, Case 4, and Case 5 with different thermal conductivities (reprinted from Liu et al. 2021d).

However, in geothermal reservoirs, the reservoir temperature can be as high as 300°C (Yu et al. 2019). Cold water injection may also last for a longer time to extract thermal energy from the subsurface. In Case 6, we set the initial reservoir temperature to 300 °C and the simulation times are elongated to 30 days and 100 days. The thermal conductivity is 3 W/(m•K) in Case 6. As shown in Figure 7.18, there are significant temperature changes and thermally induced rock deformation. The temperature diffuses further into the reservoir as simulation time increases. Figure 7.19 shows that the displacements are in the order of a few millimeters, which indicates pronounced deformations. The maximum induced displacement reaches about 7 mm in this case. Correspondingly, the strain data is also in the order of 10^{-3}, which is comparable to the mechanical induced strain. Therefore, in long-term LF-DAS monitoring of cold fluid

injection in hot geothermal reservoirs, it is necessary to consider thermal effects on LF-DAS measurements.

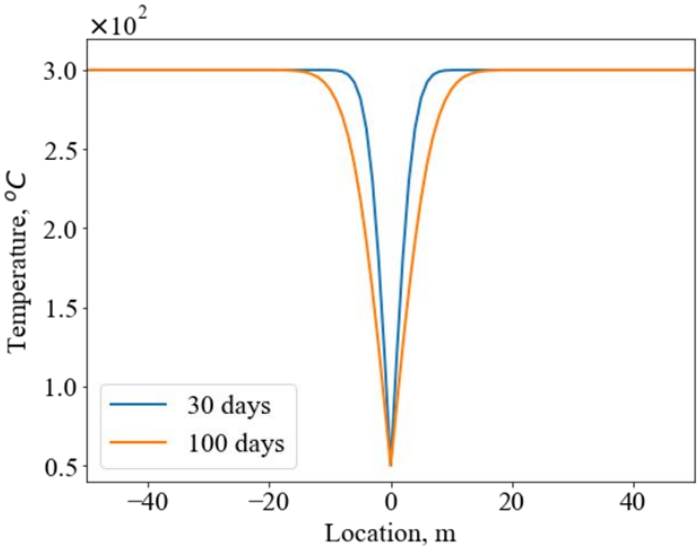

Figure 7.18 Temperature profiles along the fiber at two different times (i.e., 30 days and 100 days) of Case 6 (reprinted from Liu et al. 2021d).

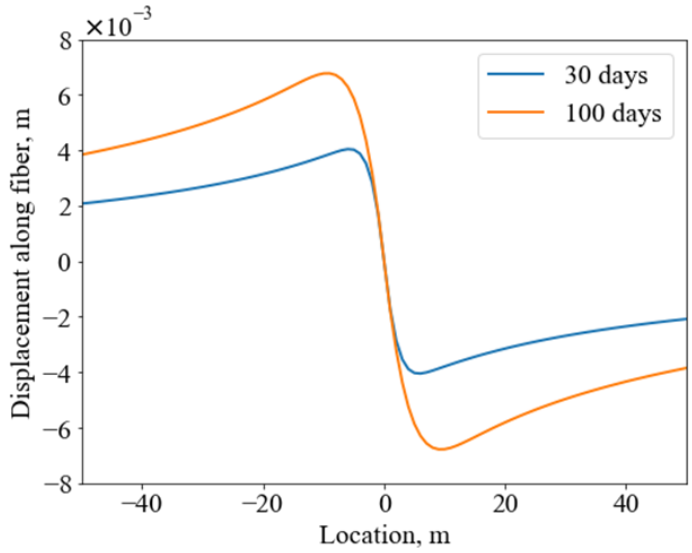

Figure 7.19 Displacement profiles along the fiber at two different times (i.e., 30 days and 100 days) of Case 6 (reprinted from Liu et al. 2021d).

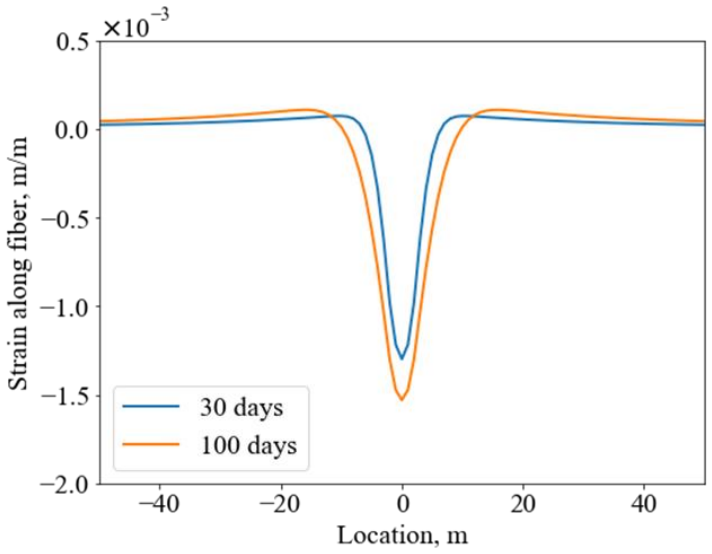

Figure 7.20 Strain profiles along the fiber at two different times (i.e., 30 days and 100 days) of Case 6 (reprinted from Liu et al. 2021d).

7.6 Summary

In this chapter, we presented a 2D thermoelastic model to quantify the contributions of thermal effects on LF-DAS strain measurements. The model was solved using a fictitious heat source method. In the current model, we assumed a constant temperature boundary condition. The objective was to have a quick assessment of the thermally induced strains that are measurable by LF-DAS.

In unconventional reservoirs, temperature perturbation does not play a significant role during stimulation processes, which usually lasts for 2-3 hours. After 1-day simulation with a temperature difference being 80 °C, the detectable strain is within one gauge length on each side of the fracture and the maximum strain is usually one order smaller than the mechanically induced strain. A larger temperature difference leads to a larger strain

around the fracture, but the affected dimension along the fiber does not show much variance, i.e., about one gauge length to the fracture surface. Similar to the effects of temperature difference, rock thermal conductivity does not have significant impacts on the LF-DAS measurement either.

In geothermal reservoirs, cold water injection may last for a longer time. Under such circumstances, temperature effects could play a dominant role, which must be considered when analyzing LF-DAS measurements for fracture characterization. The thermally induced strain measured by LF-DAS can be one order larger than the mechanical strain during long-term cold fluid injection operations in hot geothermal reservoirs.

CHAPTER 8

CONCLUSIONS AND FUTURE WORK

8.1 Key Conclusions

We summarize the key contributions and new insights obtained from this research into three sections, i.e., forward modeling, inverse modeling, and field applications, in accordance with the objectives stated in Chapter 1.

8.1.1 Forward Modeling and Analysis of LF-DAS Signals

An efficient geomechanical model on the basis of a three-dimensional displacement discontinuity method was developed, which calculated the dynamic fracture-induced rock deformations and characterized strain/strain-rate responses measured by LF-DAS during multifracture propagation. The primary capabilities of the developed model include:

1. The model can handle complex fracture geometries generated by any third-party fracturing simulator as long as the fracture information is stored in the required input format.

2. The model is very flexible in dealing with various well configurations. The horizontal treatment well and monitoring wells can be placed in different depths with any arbitrary directions.

3. The model honors the realistic spatial resolution of distributed acoustic sensing. The sensing locations along the fiber and gauge length can be the same as those in the real field monitoring operations.

The major objective of developing such a model is to simulate, characterize, and analyze the LF-DAS signals for a better understanding of the influencing mechanisms for the observed patterns of LF-DAS signals. The major outputs of the forward model are:

1. Spatial distributions of fracture-induced displacement and strain in the direction of the monitoring wells at specified time steps during fracture propagation.

2. Waterfall plots of displacements, strains, and strain rates along the monitoring wells.

One main application of the forward model in this study was to understand fracture-hit signatures and propose guidelines for accurate fracture-hit detection. Three 1D features were defined based on the outputs of the forward model, i.e., maximum strain rate, summation of strain rate, and summation of strain-rate magnitude along each sensing location (channel). Based on the distinct signatures of the three 1D features, a general guideline was proposed, which could significantly reduce the uncertainties in identifying fracture hits in multicluster stimulation jobs.

The key findings from the forward modeling are summarized as follows:

1. Fracture opening deforms the rock in the opposite directions, resulting in extension in front of the fracture tips and compression on both sides of the fracture. These physical characteristics of fracture-induced rock deformation can generate featuring signatures that are measurable by the time serial LF-DAS data, which, in turn, can be used for hydraulic fracture characterization.

2. Distinct responses can be observed related to the time when the fracture hits the offset monitoring well. In the waterfall plot of strain, there is a heart shape as the fracture

tip approaches the monitoring well, representing the narrowing extension detected by the fiber. After the fracture hit, the location where the fracture encounters the fiber is extended while the sections on both sides of the fracture are compressed, which is the effect of stress shadowing.

3. In the strain-rate waterfall plot, there is also a heart-shaped extending zone before fracture hit, indicating the magnitude of extension keeps increasing. After the fracture hit, a two-wing compressing zone divided by an extending zone is formed. When interpreting field LF-DAS data, the fracture hit should be picked where the transition from a heart shape to the pattern of a two-wing compressing zone occurs.

4. Under the same color bar range, the sizes of the observable signatures on the strain-rate waterfall plot increase with the fracture width, because a larger fracture opening induces more significant deformation over a longer length along the fiber. The dimension in the time axis of the compressing zone is related to the fracture propagation speed. Fractures with a slower propagation speed could generate strain perturbation detectable by the cable over a longer time sequence, which results in an elongated strain-rate pattern.

5. After the fracture hit, the strain variations measured by the fiber sections off the fracture path are influenced by both the compression induced by the fracture opening at the fracture-hit location and extension induced by the opening of the fracture sections near the monitoring well. Fractures with a large height would induce more pronounced extension on the fiber in the vicinity of the fracture, which results in less overall compression, indicated by a resumed extending signature in the waterfall plot of LF-DAS strain-rate data.

6. The size of the heart-shaped zone is dependent on the fracture height at the tip. A clear red extending zone with decreasing overall compression near the fracture-hit location can be observed after the fracture hit because of the gradual height growth. The decrease of the affected dimension along the location axis is smoother when fracture growth is considered, because fracture height keeps growing gradually in each timestep such that the strain perturbation can be detected by the fiber for a longer time.

7. During simultaneous multifracture propagation, only the fractures that propagate close to the monitoring well can be detected, and the different fracture hit times can be clearly identified. In addition, the strain-rate waterfall plots could reflect the interactions among fractures, such as relative fracture opening/closing, and fracture propagation characteristics, such as the stop and restart of fractures.

8. The widths of red extending bands after fracture hits are dependent on the predefined gauge length. When the gauge length is close to the cluster spacing, the red extending zones of individual fractures could overlap in multiple-cluster completion, which makes characteristic signatures of the three features (i.e., the maximum strain rate, the summation of strain rates, and summation of the amplitude of strain rates) corresponding to every single fracture less distinguishable.

9. At fracture-hit channels, the three features show significant peak values or local deflections, which help to accurately identify fracture hits when the LF-DAS data is complicated.

10. Fracture interference becomes more severe as the cluster spacing reduces in simultaneous multifracture propagation, which may result in dynamic intermittent fracture

closing/opening or fracture curving. These processes can be diagnosed by LF-DAS data, indicated by discontinuities of the red extending zones and off-azimuth fracture-hit locations.

In addition, a 2D thermoelastic model was developed based on a fictitious heat source method. The main purpose was to have an assessment of the thermal-induced rock deformation that can be detected by LF-DAS along horizontal offset wells. The main conclusions are:

1. Temperature perturbation does not play a significant role in unconventional reservoirs. After 1-day simulation with a temperature difference being 80 °C, the detectable strain is within one gauge length on each side of the fracture and the maximum strain is usually one order smaller than the mechanically induced strain.

2. During long-term cold-water injection into hot reservoirs such as geothermal reservoirs, temperature effects could play a dominant role, which must be considered when analyzing LF-DAS measurements for fracture characterization. The thermally induced strain measured by LF-DAS can be one order larger than the mechanical strain after tens of days of injection.

8.1.2 Quantitative Hydraulic Fracture Characterization

Our inversion process consists of two steps: fracture width inversion and fracture height estimation. For fracture width inversion, we proposed a Green-function-based inversion algorithm, in which the strains monitored by LF-DAS along an offset well were related to the fracture widths through a Green function, which was constructed based on a 3D displacement discontinuity method. The linear least-squares method with

regularization can be used to solve the problem efficiently. We used Markov chain Monto Carlo (MCMC) simulations to verify our hypothesis that LF-DAS strain data are only sensitive to the fracture segments near the monitoring well. After we obtained the fracture widths, we back calculated the strain profiles with a strong smoothness constraint under different fracture heights. The error between the back-calculated strain data using the inverted widths and the true strain data should be decreasing as the fracture height is getting close to the true value. The main functions of the inverse modeling workflow are:

1. Near real-time fracture width inversion for the whole stimulation process using LF-DAS strain data for both single- and multiple-cluster completion designs.

2. Equivalent created fracture height estimation at specific time steps based on the inverted widths.

From the inverse modeling studies, we obtained the following key insights pertinent to estimate hydraulic fracture geometry by direct inversion of LF-DAS strain data:

1. Without regularization, the least-squared-method inversion results might be unstable because the linear system is underdetermined. Constraints, such as a smooth fracture or symmetric fracture, could stabilize the inversion process. However, the inversion results are nonunique depending on the weights of the regularization terms.

2. Regardless of the different regularization terms used to stabilize the linear underdetermined system, the inverted fracture width at the fracture-hit location is always nearly identical to the true value. This is because of the data sensitivity, an inherent

property of the Green function matrix, which imposes a dominant constraint on the fracture width at the fracture-hit location.

3.MCMC simulations confirm that the LF-DAS strain data are only sensitive to the fracture segments near the monitoring well, and the geometries of fracture sections that are far away from the monitoring well cannot be directly obtained from the inversion of LF-DAS data. At the fracture-hit location, the mean of the inversion results matches the true value with negligible variance.

4. LF-DAS data near the fracture-hit location usually cannot accurately represent the fracture-induced strain perturbation in the formation because of the decoupling and thermal effects, which might make the inversion results unreliable. It is suggested to use the strain data in the "stress-shadow" regions, at least one-half gauge length away from the fracture-hit location.

5. In multifracture scenarios, when the strain data set is complete (i.e., all the measured data along the fiber can be used for inversion), the algorithm only needs to be stabilized by the smoothness regularization. Near the monitoring well, both the width summation of all fractures and the individual width of each fracture match well with the true values.

6. Exclusion of the strain data near the fracture-hit locations, because of the LF-DAS measurement bias, may result in deviations of fracture width from the true value for each individual fracture. Nevertheless, the width summation of all fractures shows a good estimation of the true value.

7. To get a better inverted-width profile for each separate fracture, a time-dependent constraint at the fracture-hit locations is added to the model, which means that the width at the current timestep is related to the width at the previous timestep and the width variation between the two timesteps. The width variation can be roughly estimated by the LF-DAS strain rate at each fracture-hit location.

8. The inversion algorithm is height-insensitive because of the extremely dominant sensitivity of the strain profile to the fracture segment near the monitoring well (i.e., fracture-hit location). Therefore, fracture height can be roughly estimated by matching the true strain profile, assuming that the inverted widths can be treated as the average fracture width near the monitoring well. The error between the calculated strain and true strain is minimum when the height is close to the true value.

8.1.3 Insights from Field Case Studies

In this dissertation, we presented LF-DAS data of 4 consecutive stages during a stimulation job along a horizontal well in an unconventional reservoir. Field LF-DAS data are much more complicated due to unavoidable complex subsurface conditions. In each field case study, we firstly identified fracture hits following the general guideline presented in Chapter 4. Then we applied the two-step inversion workflow developed in Chapter 5 to characterize hydraulic fracture geometry. The field examples demonstrated the efficiency and accuracy of the workflow for quantitative hydraulic fracture geometry characterization. New insights regarding the fracture propagation characteristics, fracture geometry, and completion issues for the presented field cases are summarized as:

1. The fractures propagate nearly perpendicular to the horizontal wellbore in the field examples in this unconventional shale formation.

2. Field studies indicate that four to five fractures in each stage with eight perforation clusters can propagate at least 1300 ft and hit the monitoring well. The fractures of the first two clusters close to the toe side usually do not hit the monitoring well, which could be due to the stress-shadow effects induced by the previous stage.

3. Fracturing fluid leaks off into the previous stage, possibly due to plug leakage, cement debonding, or fluid pumping before the ball seat, which could negatively affect the completion efficiency of the current stage.

4. Early first fracture-hit time may indicate there is one or two dominant fracture(s) taking a large portion of fracturing fluid.

5. The temporal evolutions of width summation of all fractures, width summations of fractures in separate stages, and width of each fracture all show consistent trends with the field LF-DAS data.

6. Dynamic fracture opening and closing processes can be retrieved from the width profiles, indicating fracture interactions in multifracture propagation.

7. At the end of fluid injection, the fracture width at the location that is 1300 ft away from the perforation point ranges approximately from near zero to 0.6 mm. The fracture reopen from the previous stage is about 0.1 mm, but certain fractures can reopen up to 0.6 mm.

8. The estimated equivalent created fracture height ranges from 55 to 80 m for the presented examples, which are consistent with the values reported in Raterman et al. (2018).

8.2 Recommendations for Future Work

Based on the results of this dissertation and the aforementioned conclusions, I make some recommendations for future work from three different perspectives as well: (1) more comprehensive characterization of LF-DAS signature patterns; (2) hydraulic fracture geometry inversion; (3) monitoring well deployment and monitoring duration. In specific, the recommendations are:

1. In the forward synthetic cases presented in this dissertation, we only characterized the LF-DAS signatures along monitoring wells that are in the same depth and parallel to the treatment well. It is recommended to investigate the LF-DAS responses under more complicated well configurations. For example, the LF-DAS signature patterns, corresponding to scenarios where fractures bypass the monitoring wells, can be modeled by putting the monitoring wells and treatment well into different depths. It is also recommended to simulate the LF-DAS responses along vertical monitoring well, which may help to characterize the fracture height evolution during a stimulation job. In addition, the monitoring wells and the treatment well could be not parallel to each other. Therefore, it is meaningful to characterize the LF-DAS signatures under such well configuration, which may be helpful to estimate the relative angles between fractures and horizontal wellbores.

2. After injection stops, fractures may close during the shut-in period. Fracture closure could generate LF-DAS signals with opposite polarities, compared to the injection phase. The shape and size of the LF-DAS signatures may be different, depending on the fracture closure behaviors that are related to the fracture conductivity and matrix permeability. It would be beneficial to develop a fracture closure model for reservoir property estimation, such as reservoir permeability.

3. Field LF-DAS data indicates that fracture width at the monitoring well keeps increasing shortly after injection stops at the treatment well. This phenomenon indicates that the pressure responses at the monitoring well are delayed. In other words, it takes time for the decreasing pressure to propagate to the monitoring well, resulting in a delayed fracture-closure signature. This inconsistency may be related to the fracture properties (e.g., fracture conductivity, fracture tortuosity, etc.) between the treatment well and monitoring well. One possible approach to investigate the mechanisms for this observation is to develop a coupled fracture flow and geomechanical model to simulate the pressure and strain responses during a short shut-in period after fluid injection.

4. In this dissertation, we quantified the thermal effects on LF-DAS measurements using a 2D thermoelastic model with fixed temperature boundary conditions. For future work, it is necessary to couple the thermal-induced rock deformation model with non-isothermal fluid flow, such that more realistic dynamic temperature distributions along the fracture during fluid injection processes can be obtained. The ultimate goal should be developing a coupled fluid flow-heat transport-geomechanics model to simulate cold water injection into hot reservoirs.

5. Because of the spatial sensitivity of LF-DAS, the information we obtained based on the analysis of LF-DAS data is limited to the fracture segments near the monitoring well. To better characterize the whole fracture, it is recommended to have multiple monitoring wells at different locations. Another choice is to combine with data from other monitoring techniques, such as microseismicity, distributed temperature sensing, and distributed strain sensing from both treatment wells and monitoring wells.

REFERENCES

Atkinson, J. and Davis, T. 2011. Multi-component time-lapse monitoring of two hydraulic fracture stimulations in the Pouce Coupe field unconventional reservoir. *First Break* **29** (10): 91-97. https://doi.org/10.1190/1.3628062.

Bernauer, M., Fichtner, A. and Igel, H., 2014. Reducing nonuniqueness in finite source inversion using rotational ground motions. *Journal of Geophysical Research: Solid Earth*, **119** (6): 4860-4875. https://doi.org/10.1002/2014JB011042.

Bakku, S. 2015. *Fracture Characterization from Seismic Measurements in a Borehole*. Ph.D. dissertation. Massachusetts Institute of Technology.

Balkan, E., Erkan, K. and Şalk, M., 2017. Thermal conductivity of major rock types in western and central Anatolia regions, Turkey. Journal of Geophysics and Engineering 14(4): 909-919.

Banerjee, P.K. 1994. Boundary Element Methods in Engineering. McGraw-Hill College.

Boone, K., Crickmore, R., Werdeg, Z. et al. 2015. Monitoring hydraulic fracturing operations using fiber-optic distributed acoustic sensing. Presented at Unconventional Resources Technology Conference, San Antonio, Texas, 20-22 July. https://doi.org/10.15530/URTEC-2158449.

Clarkson, C. R. and Williams-Kovacs, J. 2013. Modeling two-phase flowback of multifractured horizontal wells completed in shale. *SPE Journal* **18** (04): 795-812. https://doi.org/10.2118/162593-PA.

Crouch, S. L. 1976. Solution of plane elasticity problems by the displacement discontinuity method. I. Infinite body solution. *International Journal for Numerical Methods in Engineering* **10** (2): 301-343. https://doi.org/10.1002/nme.1620100206.

Crouch, S. L., Starfield, A. M., and Rizzo, F. 1983. Boundary element methods in solid mechanics. *Journal of Applied Mechanics* **50**: 704. https://doi.org/10.1115/1.3167129.

Dahi-Taleghani, A. and Olson, J. E. 2011. Numerical modeling of multistranded-hydraulic-fracture propagation: accounting for the interaction between induced and natural fractures. *SPE Journal* **16** (03): 575-581. https://doi.org/10.2118/124884-PA.

Daneshy, A. 2011. Multistage fracturing using plug-and-perf systems. *World oil* **232** (10).

Dawson, M. and Kampfer, G. 2016. Breakthrough in hydraulic fracture & proppant mapping: Achieving increased precision with lower cost. Paper Presented at Unconventional Resources Technology Conference, San Antonio, Texas, USA, 1-3 August. https://doi.org/10.15530/urtec-2016-2432330.

Dong, C. and De Pater, C. 2001. Numerical implementation of displacement discontinuity method and its application in hydraulic fracturing. *Computer methods in applied mechanics and engineering* **191** (8-10): 745-760. https://doi.org/10.1016/S0045-7825(01)00273-0.

Efendiev, Y., Datta-Gupta, A., Ginting, V. et al. 2005. An efficient two-stage Markov chain Monte Carlo method for dynamic data integration. *Water Resources Research* **41** (12). https://doi.org/10.1029/2004WR003764.

Fisher, M., Heinze, J., Harris, C. et al. 2004. Optimizing horizontal completion techniques in the Barnett shale using microseismic fracture mapping. Paper Presented at the SPE Annual Technical Conference and Exhibition, Houston, Texas, USA, 26-29 September. SPE-90051-MS. https://doi.org/10.2118/90051-MS.

Fu, P., Johnson, S. M., Carrigan, C. R. et al. 2013. An explicitly coupled hydro-geomechanical model for simulating hydraulic fracturing in arbitrary discrete fracture networks. *International Journal for Numerical Methods in Engineering* **37** (14): 2278-2300. https://doi.org/10.1002/nag.2135.

Ghassemi, A. and Zhang, Q., 2004. A transient fictitious stress boundary element method for porothermoelastic media. Engineering analysis with boundary elements, 28(11): 1363-1373.

Grubert, M. A., Li, X., and Chavarria, A.2020. Making Sense of Unconventionals with DAS. Oilfield Technology13 (Jan/Feb): 21–24.

Hartog, A. H. 2017. An introduction to distributed optical fibre sensors, CRC press.

Haustveit, K., Dahlgren, K., Greenwood, H. et al. 2017. New Age Fracture Mapping Diagnostic Tools-A STACK Case Study. Presented at SPE Hydraulic Fracturing Technology Conference and Exhibition. https://doi.org/10.2118/184862-MS.

Haustveit, K., Elliott, B, Haffener, J. et al. 2020. Monitoring the Pulse of a Well Through Sealed Wellbore Pressure Monitoring, a Breakthrough Diagnostic with a Multi-Basin Case Study. Paper Presented at the SPE Hydraulic Fracturing Technology Conference and Exhibition, The Woodlands, Texas, USA, 4-6 February. SPE-199731-MS. https://doi.org/10.2118/199731-MS.

Hill, D. 2015. Distributed Acoustic Sensing (DAS): Theory and Applications. *Frontiers in Optics*. Optical Society of America.

Holley, E.H. and Kalia, N. 2015. Fiber-optic monitoring: Stimulation results from unconventional reservoirs. Presented at Unconventional Resources Technology Conference, San Antonio, Texas, 20-22 July. https://doi.org/10.15530/URTEC-2015-2151906.

Hu, X., Wu, K., Song, X. 2018. Development of a New Mathematical Model To Quantitatively Evaluate Equilibrium Height of Proppant Bed in Hydraulic Fractures for Slickwater Treatment (includes associated supplemental discussion). *SPE Journal* **23**(06): 2158-2174. SPE-191360-PA. https://doi.org/10.2118/191360-PA.

Huckabee, P. T. 2009. Optic Fiber Distributed Temperature for Fracture Stimulation Diagnostics and Well Performance Evaluation. Paper Presented at the SPE Hydraulic Fracturing Technology Conference, The Woodlands, Texas, USA, 19-21 January. SPE-118831-MS. https://doi.org/10.2118/118831-MS.

Ichikawa, M., Kurosawa, I., Uchida, S. et al. 2019. Case Study of Hydraulic Fracture Monitoring Using Low-Frequency Components of DAS data. Proceeding in SEG Technical Program Expanded Abstracts, Society of Exploration Geophysicists**:** 948-952. https://doi.org/10.1190/segam2019-3214251.1.

In't Panhuis, P., den Boer, H., Van Der Horst, J. et al. 2014. Flow monitoring and production profiling using DAS. Presented at SPE Annual Technical Conference and Exhibition. https://doi.org/10.2118/170917-MS.

Jin, G, Mosher, C. C., Filice, F. P. et al. 2017a. *Hydraulic fracture monitoring by low-frequency das*, US Patents.

Jin, G. and Roy, B 2017b. Hydraulic-Fracture Geometry Characterization Using Low-Frequency DAS Signal. *The Leading Edge* **36**(12): 975-980. https://doi.org/10.1190/tle36120975.1.

Jin, G., Krueger, K. R., and Roy, B. 2019a. *Low frequency das well interference evaluation*. US Patent.

Jin, G., Mendoza, K., Roy, B. et al. 2019b. Machine Learning-Based Fracture-Hit Detection Algorithm Using LFDAS Signal. *The Leading Edge* **38**(7): 520-524. https://doi.org/10.1190/tle38070520.1.

Karmakar, S., Ghergut, J., and Sauter, M. 2016. Early-Flowback Tracer Signals for Fracture Characterization in an EGS Developed in Deep Crystalline and Sedimentary Formations: A Parametric Study. *Geothermics* 63: 242-252. https://doi.org/10.1016/j.geothermics.2015.08.007.

Karrenbach, M., Cole, S., Ridge, A. et al. 2019. Fiber-Optic Distributed Acoustic Sensing of Microseismicity, Strain and Temperature during Hydraulic Fracturing. *Geophysics* 84(1): D11-D23. https://doi.org/10.1190/geo2017-0396.1.

Labus, M. and Labus, K., 2018. Thermal conductivity and diffusivity of fine-grained sedimentary rocks. Journal of Thermal Analysis and Calorimetry 132(3): 1669-1676.

Lascelles, P., Wan, J., Robinson, L. et al. 2017. Applying Subsurface DNA Sequencing in Wolfcamp Shales, Midland Basin. Paper Presented at the SPE Hydraulic Fracturing Technology Conference and Exhibition, The Woodlands, Texas, USA, 24-26 January. https://doi.org/10.2118/184869-MS.

Li, X. and Zhu, D. (2018). Temperature Behavior during Multistage Fracture Treatments in Horizontal Wells. *SPE Production & Operations* **33** (03): 522-538. SPE-181876-PA. https://doi.org/10.2118/181876-PA.

Li, X., Zhang, J., Grubert, M. et al. 2020. Distributed Acoustic and Temperature Sensing Applications for Hydraulic Fracture Diagnostics. Presented at SPE Hydraulic Fracturing Technology Conference and Exhibition, The Woodlands, Texas, USA, 4-6 February. SPE-199759-MS. https://doi.org/10.2118/199759-MS.

Lindsey, N.J., Rademacher, H. and Ajo-Franklin, J.B., 2020. On the broadband instrument response of fiber-optic DAS arrays. *Journal of Geophysical Research: Solid Earth,* **125**(2): 1-16. https://doi.org/10.1029/2019JB018145.

Liu, F., Wu, J., Jin, M. et al. 2020a. From Reservoir Characterization to Reservoir Monitoring: An Integrated Workflow to Optimize Field Development Using Geochemical Fingerprinting Technology. Paper Presented at the SPE/SEG/AAPG Unconventional Resources Technology Conference, Austin, Texas, USA, 20-22, July. https://doi.org/10.15530/urtec-2020-2902.

Liu, Y., Jin, G., Wu, K. et al. 2021a. Quantitative Hydraulic-Fracture Geometry Characterization with LF-DAS Strain Data: Numerical Analysis and Field Applictations. SPE Hydraulic Fracturing Technology Conference and Exhibition, Virtual, 4-6 May. SPE-204158-MS.

Liu, Y., Jin, G., Wu, K., et al. 2021b. Hydraulic-Fracture-Width Inversion Using Low-Frequency Distributed-Acoustic-Sensing Strain Data. Part II: Extension for Multifracture and Field Application. *SPE Journal*. SPE-205379-PA. https://doi.org/10.2118/205379-PA.

Liu, Y., Jin, G., Wu, K., et al. 2021c. Hydraulic-Fracture-Width Inversion Using Low-Frequency Distributed-Acoustic-Sensing Strain Data. Part I: Algorithm and Sensitivity Analysis. *SPE Journal*. SPE-204225-PA. https://doi.org/10.2118/204225-PA.

Liu, Y., Leung, J. Y., Chalaturnyk, R. et al. 2019. New insights on mechanisms controlling fracturing-fluid distribution and their effects on well performance in shale-gas reservoirs. *SPE Prod & Oper*. SPE-185043-PA. https://doi.org/10.2118/185043-PA.

Liu, Y., Wu, K., Jin, G. et al. 2020b. Fracture-Hit Detection Using LF-DAS Signals Measured during Multifracture Propagation in Unconventional Reservoirs. *SPE Reservoir Evaluation & Engineering*. SPE-204457-PA. https://doi.org/10.2118/204457-PA.

Liu, Y., Wu, K., Jin, G. et al. 2020c. Hydraulic Fracture Modeling of Fracture-Induced Strain Variation Measured by Low-Frequency Distributed Acoustic Sensing (LF-DAS) along Offset Wells. Paper Presented at the 54th US Rock Mechanics/Geomechanics Symposium, Golden, Colorado, USA. ARMA-20-1426.

Liu, Y., Wu, K., Jin, G. et al. 2020d. Rock Deformation and Strain-Rate Characterization during Hydraulic Fracturing Treatments: Insights for Interpretation of Low-

Frequency Distributed-Acoustic Sensing Signals. *SPE Journal*. SPE-202482-PA. https://doi.org/10.2118/202482-PA.

Liu, Y., Wu, K., Jin, G. et al. 2021d. Quantification of Thermal Effects on Cross-Well Low-Frequency Distributed Acoustic Sensing Measurements. AAPG/SEG/SPE Unconventional Resources Technology Conference, 26-28 July, Houston, Texas, USA.

Mack, M. G., Elbel, J. L., and Piggott, A. R. 1992. Numerical representation of multilayer hydraulic fracturing. Presented at the 33th US Symposium on Rock Mechanics (USRMS).

Maxwell, S.C., Waltman, C., Warpinski, N.R. et al. 2009. Imaging seismic deformation induced by hydraulic fracture complexity. *SPE Reservoir Evaluation & Engineering*. **12**(01): 48-52.

Molenaar, M.M., Fidan, E. and Hill, D.J. 2012. Real-time downhole monitoring of hydraulic fracturing treatments using fiber optic distributed temperature and acoustic sensing. Presented at SPE/EAGE European Unconventional Resources Conference & Exhibition, Vienna, Austria, 20-22 March, 2012. https://doi.org/10.2118/152981-MS.

Ng, M., Umholtz, N., Hammerquist, C. et al. 2019. Quantifying Hydraulic Fracture Height Reduction in the Presence of Laminations and Weak Interfaces—Validation with Microseismic Moment Tensor Inversion in the Montney Shale. Paper Presented at

the SPE/AAPG/SEG Unconventional Resources Technology Conference, Denver, Colorado, USA, 22-24, July. https://doi.org/10.15530/urtec-2019-875.

Perkins, T.K. and Kern, L.R., 1961. Widths of hydraulic fractures. *Journal of Petroleum Technology*, **13**(09): 937-949. https://doi.org/10.2118/89-PA.

Pollard, D. D. and Segall, P. 1987. Theoretical displacements and stresses near fractures in rock: with applications to faults, joints, veins, dikes, and solution surfaces. *Fracture mechanics of rock* 277-349. Acad. Press, London, United Kingdom.

Raterman, K., Liu, Y., Warrrn, L. et al. 2019. Analysis of a Drained Rock Volume: An Eagle Ford Example. Paper Presented at the Unconventional Resources Technology Conference, Denver, Colorado, USA, 22-24, July. https://doi.org/10.15530/urtec-2019-263.

Raterman, K.T., Farrell, H.E., Mora, O.S., et al. 2018. Sampling a Stimulated Rock Volume: An Eagle Ford Example. *SPE Reservoir Evaluation & Engineering*. **21**(04): 927-941. https://doi.org/10.2118/191375-PA.

Richter, P., Parker, T., Woerpel, C. et al. 2019. High-resolution distributed acoustic sensor using engineered fiber for hydraulic fracture monitoring and optimization in unconventional completions. Proceeding in SEG Technical Program Expanded Abstracts, Society of Exploration Geophysicists**:** 4874-4878. https://doi.org/10.1190/segam2019-3215860.1.

Roussel, N. P. and Agrawal, S. 2017. Introduction to Poroelastic Response Analysis–Quantifying Hydraulic Fracture Geometry and SRV Permeability from Offset-Well Pressure Data. Paper Presented at the Unconventional Resources Technology Conference, Austin, Texas, USA, 24-26, July. https://doi.org/10.15530/urtec-2017-2645414.

Salamon, M.D.G., 1964. Elastic analysis of displacements and stresses induced by mining of seam or reef deposits: Part IV: Inclined reef. *Journal of the Southern African Institute of Mining and Metallurgy*. **65**(5): 319-338.

Sangnimnuan, A., Li, J., Wu, K. et al. 2019. Fracture Hits Analysis for Parent-Child Well Development. Presented at 53rd US Rock Mechanics/Geomechanics Symposium. ARMA-2019-1542.

Seth, P., Manchanda, R., Elliott, B. et al. 2019. Diagnosing Multi-Cluster Fracture Propagation Using Dynamic Poroelastic Pressure Transient Analysis. Paper Presented at the Unconventional Resources Technology Conference, Denver, Colorado, USA, 22-24, July. https://doi.org/10.15530/urtec-2019-1092.

Shapiro, S.A., Dinske, C. and Rothert, E., 2006. Hydraulic-Fracturing Controlled Dynamics of Microseismic Clouds. *Geophysical Research Letters*, **33**(14).

Shapiro, S.A., Huenges, E., and Borm, G. 1997. Estimating the Crust Permeability from Fluid-Injection-Induced Seismic Emission at the KTB Site. *Geophysical Journal International*. **131**(2): F15-F18.

Shapiro, S.A., Rothert, E., Rath, V., et al. 2002. Characterization of Fluid Transport Properties of Reservoirs Using Induced Microseismicity. *Geophysics.* **67**(01): 212-220.

Shen, B., Guo, H., Ko, T.Y. et al. 2013. Coupling rock-fracture propagation with thermal stress and fluid flow. International Journal of Geomechanics 13(6): 794-808.

Sherman, C., Mellors, R., Morris, J. et al. 2019. Geomechanical Modeling of Distributed Fiber-Optic Sensor Measurements. *Interpretation* **7** (1): SA21-SA27. https://doi.org/10.1190/INT-2018-0063.1.

Sherman, C., Morris, J., Mellors, R. et al. 2017. Simulating Fracture-Induced Strain Signals Measured by a Distributed Fiber-Optic Sensor. Proceeding in SEG Technical Program Expanded Abstracts, Society of Exploration Geophysicists**:** 4113-4117. https://doi.org/10.1190/segam2017-17678887.1.

Sherman, C., Mellors, R.J., Morris, J. et al. 2018. Modeling Distributed Fiber Optic Sensor Signals Using Computational Rock Mechanics. Paper Presented at the AAPG/SEG/SPE Unconventional Resources Technology Conference, Houston, Texas, 23-25 July.

Shou, K. J. 1993. *A High Order Three-Dimensional Displacement Discontinuity Method with Application to Bonded Half-Space Problems*. PhD dissertation, University of Minnesota, Minneapolis, Minnesota, USA.

Shou, K.-J., Siebrits, E. and Crouch, S. L. 1997. A higher order displacement discontinuity method for three-dimensional elastostatic problems. *International Journal of Rock Mechanics and Mining Sciences* **34** (02): 317-322. https://doi.org/10.1016/S0148-9062(96)00052-6.

Silkina, T. 2014. *Application of distributed acoustic sensing to flow regime classification.* Master's thesis, Norwegian University of Science and Technology.

Siriwardane, H. J. and Layne, A. W. 1991. Improved model for predicting multiple hydraulic fracture propagation from a horizontal well. Presented at the SPE Eastern Regional Meeting, Lexington, Kentucky, USA, 22-25 October. SPE-23448-MS. https://doi.org/10.2118/23448-MS.

Sun, H., Yu, W. and Sepehrnoori, K. 2017. A New Comprehensive Numerical Model for Fracture Diagnosis with Distributed Temperature Sensing DTS. Paper Presented at the SPE Annual Technical Conference and Exhibition, San Antonio, Texas, USA, 9-11 October. SPE-187097-MS. https://doi.org/10.2118/187097-PA.

Sun, Y., Xue, Z., Hashimoto, T. et al. 2020. Distributed Fiber Optic Sensing System for Well-Based Monitoring Water Injection Tests - A Geomechanical Responses Perspective. *Water Resources Research*. https://doi.org/10.1029/2019WR024794.

Tabatabaei, M. and Zhu, D. 2012. Fracture-Stimulation Diagnostics in Horizontal Wells Through Use of Distributed-Temperature-Sensing Technology. *SPE Production & Operations* **27** (04): 356-362. https://doi.org/10.2118/148835-PA.

Ugueto, G. A., Huckabee, P. T. et al. 2016. Perforation cluster efficiency of cemented plug and perf limited entry completions; Insights from fiber optics diagnostics. Presented at the SPE Hydraulic Fracturing Technology Conference, Woodlands, Texas, USA, 9-11 February. SPE-179124-MS. https://doi.org/10.2118/179124-MS.

Ugueto, G. A., Todea, F., Daredia, T. et al. 2019. Can You Feel the Strain? DAS Strain Fronts for Fracture Geometry in the BC Montney, Groundbirch. Paper Presented at the SPE Annual Technical Conference and Exhibition, Calgary, Alberta, Canada, 30 September - 2 October. SPE-195943-MS. https://doi.org/10.2118/195943-MS.

Van Der Baan, M., Eaton, D. and Dusseault, M. 2013. Microseismic monitoring developments in hydraulic fracture stimulation. Paper Presented at the ISRM international conference for effective and sustainable hydraulic fracturing. International Society for Rock Mechanics and Rock Engineering.

Wang, J., Elsworth, D. and Denison, M.K., 2018. Propagation, proppant transport and the evolution of transport properties of hydraulic fractures. *Journal of Fluid Mechanics*. **855**: 503-534. https://doi.org/10.1017/jfm.2018.670.

Wang, X., Jardani, A. and Jourde, H. 2017. A hybrid inverse method for hydraulic tomography in fractured and karstic media. *Journal of Hydrology* **551**: 29-46. https://doi.org/10.1016/j.jhydrol.2017.05.051.

Webster, P., Cox, B. and Molenaar, M., 2013. Developments in diagnostic tools for hydraulic fracture geometry analysis. Presented at Unconventional Resources Technology Conference, Denver, Colorado, USA, 12-14 August. https://doi.org/10.1190/urtec2013-025.

Wu, K. 2014. *Numerical Modeling of Complex Hydraulic Fracture Development in Unconventional Reservoirs*. PhD dissertation. The University of Texas at Austin, Austin, Texas, USA.

Wu, Y., Richter, P., Hull, R. and Farhadiroushan, M., 2020. Hydraulic Frac-Hit Corridor (FHC) Monitoring and Analysis with High-Resolution Distributed Acoustic Sensing (DAS) and Far-Field Strain (FFS) Measurements. *First Break*, **38(**6): 65-70.

Yu, X., Winterfeld, P., Wang, S. et al. 2019. A Geomechanics-Coupled Embedded Discrete Fracture Model and its Application in Geothermal Reservoir Simulation. Paper Presented at the SPE Reservoir Simulation Conference, Galveston, Texas, USA, 10-11 April 2019.

Zhang, Q. 2004. “A boundary element method for thermo-poroelasticity with applications in rock mechanics.” M.Sc. thesis, Univ. of North Dakota, Grand Forks, ND.

Zhang, S. and Zhu, D. 2020. Inversion of Downhole Temperature Measurements in Multistage-Fracturing Stimulation of Horizontal Wells in Unconventional

Reservoirs. *SPE Production & Operations* **35** (02): 231-244. https://doi.org/10.2118/187322-PA.

Zhang, Z., Fang, Z., Stefani, J. et al. 2020. Modeling of Fiber Optic Strain Responses to Hydraulic Fracturing. *Geophysics* **85**(6): 1-22. https://doi.org/10.1190/geo2020-0083.1.